MULTICARRIER TRANSMISSION TECHNIQUES

A Thesis Submitted
to the College of Graduate and Postdoctoral Studies
in Partial Fulfillment of the Requirements
for the Degree of Master of Science
in the Department of Electrical and Computer Engineering
University of Saskatchewan

by

QUANG DUONG

Saskatoon, Saskatchewan, Canada

Permission to Use

In presenting this thesis in partial fulfillment of the requirements for a Postgraduate degree from the University of Saskatchewan, it is agreed that the Libraries of this University may make it freely available for inspection. Permission for copying of this thesis in any manner, in whole or in part, for scholarly purposes may be granted by the professors who supervised this thesis work or, in their absence, by the Head of the Department of Electrical and Computer Engineering or the Dean of the College of Graduate and Postdoctoral Studies at the University of Saskatchewan. Any copying, publication, or use of this thesis, or parts thereof, for financial gain without the written permission of the author is strictly prohibited. Proper recognition shall be given to the author and to the University of Saskatchewan in any scholarly use which may be made of any material in this thesis.

Request for permission to copy or to make any other use of material in this thesis in whole or in part should be addressed to:

Head of the Department of Electrical and Computer Engineering
57 Campus Drive
University of Saskatchewan
Saskatoon, Saskatchewan S7N 5A9
Canada

OR

Dean
College of Graduate and Postdoctoral Studies
University of Saskatchewan
116 Thorvaldson Building, 110 Science Place
Saskatoon, Saskatchewan S7N 5C9
Canada

Abstract

In this thesis, multicarrier transmission techniques envisioned for the fifth-generation wireless networks are studied. First, three basic techniques, namely orthogonal frequency-division multiplexing (OFDM), filter-bank multicarrier offset quadrature amplitude modulation (FBMC-OQAM), and generalized frequency-division multiplexing (GFDM) are reviewed in detail. In particular, the block-based structure and cyclic prefixing of OFDM are discussed and its bit error rate (BER) performance is analyzed. Then it is demonstrated that with offset QAM the orthogonality between subcarriers in FBMC-OQAM is preserved. Next, the roles of tail biting technique and circular convolution in GFDM are explained. An efficient implementation of GFDM is also described.

Second, circular filterbank multicarrier offset QAM (CFBMC-OQAM), a technique which combines the block-based structure of GFDM and offset QAM of FBMC-OQAM, is presented. Then a precoded scheme is proposed, in which the Walsh-Hadamard (WH) transform is applied to CFBMC-OQAM system, resulting in a precoded scheme called WH-CFBMC-OQAM. The proposed system has a block-based structure and can be implemented efficiently using fast Fourier transform (FTT) and inverse FFT (IFFT). In addition, a cyclic prefix can be inserted to facilitate simple equalization at the receiver. WH-CFBMC-OQAM exploits the frequency diversity by averaging the signal-to-noise ratios (SNRs) over all subcarriers. A theoretical approximation for the bit error rate performance of WH-CFBMC-OQAM over a frequency-selective channel is derived. Under the same system configuration, simulation results demonstrate the excellent performance of the proposed scheme when compared to the performance of other techniques. Simulation also verifies that the theoretical results match perfectly with simulation results for any SNR value.

Acknowledgments

Firstly, I would like to express my sincere gratitude to my advisor, Prof. Ha Nguyen, for the continuous support of my M.Sc studies and research, for his patience, motivation, and immense knowledge. His guidance helped me in carrying out research and writing this thesis.

I thank my fellow labmates, Binh Vo, and Tung Nguyen, for stimulating discussions, for the help of creating illustrative figures, and for all the fun we have had in the last three years.

Last but not the least, I would like to thank my parents and my brother for supporting me spiritually throughout my M.Sc. program and my life in general.

Table of Contents

List of Abbreviations

AWGN	Additive White Gaussian Noise
BER	Bit Error Rate
CFBMC-OQAM	Circular Filterbank Multicarrier Offset QAM
CP	Cyclic Prefix
FBMC-OQAM	Filterbank Multicarrier Offset QAM
FEQ	Frequency Domain Equalizer
FFT/IFFT	Fast Fourier Transform/Inverse Fast Fourier Transform
FSC	Frequency Selective Channel
GFDM	Generalized Frequency Division Multiplexing
IBI	Interblock Interference
ICI	Intercarrier Interference
ISI	Intersymbol Interference
LPF	Low Pass Filter
MFR	Matched Filter Receiver
ML	Maximum Likelihood
MMSE	Minimum Mean Square Error
OFDM	Orthogonal Frequency Division Multiplexing
QAM	Quadrature Amplitude Modulation
QPSK	Quadrature Phase Shift Keying
QoS	Quality of Service
RC	Raised Cosine
SC-QAM	Single Carrier QAM
SNR	Signal to Noise Ratio
SRRC	Square Root Raised Cosine
WH	Walsh Hadamard

WH-CFBMC-OQAM	Walsh Hadamard Circular Filterbank Multicarrier Offset QAM
WH-GFDM	Walsh Hadamard Generalized Frequency Division Multiplexing
WSS	Wise Sense Stationary
ZFR	Zero Forcing Receiver
ZP	Zero Padding

List of Figures

List of Tables

1. Introduction

Driven by the fast-growing demand in data traffic, research on enabling technologies for the next (i.e., the fifth) generation of cellular networks, 5G networks, has been very active during the past few years [1], [2]. Today, the use of powerful smartphones and tablets imposes a high demand on advanced multimedia capabilities [3]. Since there are more users, devices, and content, new innovative technologies that are efficient and intelligent are desired to address many challenges, such as bandwidth shortage [4], high energy consumption [5], and diverse quality of service requirements (QoS). The current cellular networks, 4G networks, have reached the theoretical limit on the data rate with the current technologies and therefore are not sufficient to cope with the above challenges. In developing 5G networks, three main requirements have been identified [2], [3], [6]. First, a wide range of data rates has to be supported, up to multiple gigabits per second, and tens of megabits per second need to be guaranteed with very high availability and reliability. Second, a roundtrip latency of about 1 ms, an order of magnitude shorter than in 4G networks, is expected. Third, network scalability and flexibility are required to support a large number of devices with very low complexity and requirements for very long battery lifetime. Among ongoing research areas that support these requirements, the modulation formats play an important role. They are the key features for the past cellular generations, and yet again are expected to undergo another major change in the upcoming fifth generation.

The fundamental design issues of the modulation formats are rooted in the random quality of the wireless channels. Due to scattering, reflection and diffraction of the transmitted signal caused by the presence of objects in the signal path, multiple versions of a transmitted signal might reach the destination via multiple paths, called multipath propagation. An important

parameter of a wireless system is the multipath delay spread, defined as the difference in propagation time between the longest and shortest paths [7]. When the delay spread is much less than the symbol time, the channel is considered as flat, and a single tap is sufficient to represent the channel. When the delay spread is larger than the symbol time, the channel is said to be frequency-selective, and it has to be represented by multiple taps.

The frequency selectivity gives rise to intersymbol interference (ISI), where the received symbol over a given symbol period experiences interference from other symbols that have been delayed by multipath [8]. An approach to deal with the ISI problem is to design an equalizer at the receiver that could compensate or reduce ISI [9]. However, the complexity of the equalizer might increase dramatically when the channel is represented by so many taps. For that reason, other approaches which require simpler equalizers are preferred. Multicarrier modulation is a well-known solution to serve that need. In fact, it is the dominating modulation format for today's wireless systems.

Multicarrier modulation is a method that divides a bit stream into multiple substreams and sends them over many different subcarriers. By doing so, the data rate on each of the subcarriers is much less than the total data rate, and the corresponding subcarrier bandwidth is much smaller than the total system bandwidth. In particular, the number of subcarriers should be chosen such that the subcarrier bandwidth is much less than the coherence bandwidth of the channel, so that the individual subcarrier experiences a relatively constant gain (i.e., flat channel) [8]. In short, multicarrier modulation decouples an ISI (frequency-selective) channel into multiple parallel subchannels such that equalization and detection at the receiver side can be done per subchannel.

Among many multicarrier techniques, orthogonal frequency division multiplexing (OFDM) dominates the current broadband wireless communication systems [10]. OFDM can completely eliminate ISI through the use of a cyclic prefix, which consists of redundant symbols replicated from the end to the beginning of each transmitted block. Further, OFDM offers other advantages such as simple equalization by applying a scalar gain per subcarrier, and efficient discrete-time implementation through fast Fourier transform (FFT). On the other hand, OFDM also has its own drawbacks, such as high spectral leakage, high peak-to-average

power ratio (PARP), and strict orthogonality requirements.

Finding an appropriate multicarrier modulation technique for the next generation networks may be based on two approaches [10]. In the first approach, the existing OFDM structure is preserved, and its drawbacks are addressed through appropriate solutions [11]. The second approach is based on a generalized framework for multicarrier systems [12], which results in different techniques than OFDM.

Filter bank multicarrier communication offset QAM (FBMC-OQAM) is another candidate for 5G networks. Although, FBMC-OQAM has been invented even before OFDM, only recently has FBMC-OQAM been considered as a promising technique, and drawn interest from research community [12]. At the transmitter, FBMC-OQAM uses a set of filters, called synthesis filter bank, to shape and then combine a set of input signals. At the receiver, FBMC-OQAM uses another set of filters, called analysis filter bank, to split the received signal into individual components. The OQAM modulation splits the complex data into real and imaginary parts. By doing so, the orthogonality condition is relaxed and only applies to the real field. This enables the use of flexible waveforms which leads to improvement of signal's power spectrum properties. These characteristics are the desired features for 5G applications. However, FBMC-OQAM does not have a block-based structure as OFDM so that CP can be inserted. This means that the subcarrier orthogonality could be destroyed when the signal is transmitted through a frequency selective channel (FSC). In that case, an equalizer with high complexity is needed at the receiver to compensate ISI.

Beside OFDM and FBMC-OQAM, there is another multicarrier scheme, called generalized frequency division multiplexing (GFDM), that has been recently proposed for the air interface of the 5G networks [13]. GFDM has a block based structure and then CP can be easily inserted. Further, GFDM exploits the block based structure to perform circular convolution for pulse shaping rather than conventional linear convolution. By doing so, filters that are better than the rectangular filter can be utilized to improve the localization property of the power spectrum density (PSD) of the transmitted signal without increasing the CP length. However, the main issue of GFDM is that it is a nonorthogonal system, and thus requiring an advanced receiver to reduce ISI and intercarrier interference (ICI). In

an additive white Gaussian noise (AWGN) channel, a matched filter receiver with iterative interference cancellation can achieve almost the same symbol error rate performance as that of OFDM [14].

Recently, circular FBMC-OQAM (CFBMC-OQAM), a modified version of FBMC-OQAM, which makes use of circular convolution as in GFDM, has been proposed [15]. By using circular convolution, CFBMC-OQAM also has a block based structure, which enables the use of CP to achieve free interblock interference (IBI), and eases the task of equalization at the receiver. Furthermore, the circular convolution preserves the continuity of the transmitted waveform within one block. That continuity is necessary to guarantee a good localized power spectrum of the transmitted signal.

When operating over FSCs, the above multicarrier schemes do not offer any multipath diversity due to the fact that each symbol is transmitted over a single flat subchannel that may experience severe fading. Thus, the overall performance of the system is dominated by the performance of badly affected subchannels if no additional technique to counteract is applied. Precoding techniques are methods to solve such severe problem, and they have been substantially studied for OFDM systems. In [16], precoded vector OFDM systems are proposed for combating channel spectral nulls and reduce CP length. In [17], designs of linear precoding to maximize diversity gain and coding gain are considered. Reference [18] proposes the use of unitary precoders to minimize the bit error rate performance. In FBMC-OQAM systems, a few precoding proposals have been presented in the literature. An analytical approximation of the error performance of a precoded FBMC-OQAM system is establised in [19] with the assumption that the transmission channel is perfectly equalized. Later, [20] extends the previous study to the case where linear MMSE equalization is employed. For GFDM systems, [21] investigates the use of a unitary matrix, the Walsh-Hadamard matrix, as the precoder, and presents analytical approximation that can be used to estimate the bit error rate of GFDM over frequency-selective channels. To the best of our knowledge, precoding techniques and bit error rate performance of CFBMC-OQAM in frequency selective channels have never been reported in the literature. Studying a precoding scheme that can improve the overall bit error rate performance of CFBMC-OQAM system in FSCs is precisely the

main objective of this thesis.

The remainder of this chapter gives an overview of the thesis, its contributions and organization.

In Chapter 2, background of single carrier and multicarrier wireless communication systems considered in this thesis is provided. In the single carrier systems, quadrature amplitude modulation (QAM) and discrete time channel model are introduced. For multicarrier systems, the transceivers of OFDM and FBMC-OQAM are presented, in which the key features of each system and the important differences between the two are discussed.

Chapter 3 presents two kinds of circular pulse-shaped waveforms for 5G networks, which are GFDM and CFBMC-OQAM. For each system, the system model and its properties are discussed, followed by the implementation structures. This chapter also highlights the necessary of circular convolution and its usefulness in multicarrier systems. Further, the similarities and differences between GFDM and CFBMC-OQAM are examined.

Chapter 4 investigates the combination of CFBMC-OQAM with WH transform, called WH-CFBMC-OQAM, to improve the BER performance over FSCs. First, the system model of WH-CFBMC-QOAM is introduced. The transceiver of a WH-CFBMC-OQAM system is basically the same as that presented in Chapter 3 for CFBMC-OQAM except that a WH precoder is applied at the transmitter side to perform a linear combination of the inputs, and the Hermitian tranpose of the precoder is applied to the output at the receiver side to reverse the precoding process. This chapter also derives the theoretical approximation for the BER performance. The simulation results show that the WH-CFBMC-OQAM is superior than WH-GFDM, and the theoretical results match well with the simulation results.

Finally, Chapter 5 draws conclusion and offers suggestions for further studies.

2. Background

The objective of a communication system is to reliably transmit information from a source to a destination. In digital communications, information is represented by a sequence of bits (i.e., a bit stream) as illustrated in Figure 2.1. The function of the transmitter is to convert the bit stream into a continuous time signal $x(t)$, called a waveform, which has energy and can be propagated through a physical channel, represented by an impulse response $h(t)$ [22]. The channel, due to its adverse effect, causes the received signal $r(t)$ different from the transmitted signal $x(t)$. The main task of the receiver is to reconstruct the transmitted bit stream with as few errors as possible.

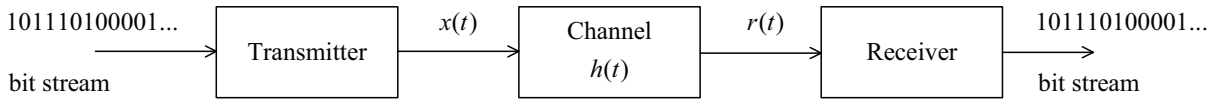

Figure 2.1: Main components of a communication system.

A more detailed block diagram of a digital communication system is illustrated in Figure 2.2 [9], [18], which consists of major signal processing tasks that are relevant to the topics discussed in this thesis. At the transmitter, the bits-to-symbol mapping block takes several bits of input and maps them to a real or complex modulation symbol $x[n]$ where n is the symbol index. Then the sequence of symbols is converted to a continuous-time signal $x_b(t)$. The signal $x_b(t)$ is a baseband signal since its spectrum is around 0 Hz. For radio transmission, the baseband signal is up-converted to a passband signal $x(t)$ whose spectrum is centered around some carrier frequency f_c. The transmitted signal $x(t)$ propagates through the channel $h(t)$, which is a continuous-time system. At the receiver, the received signal $r(t)$ is first down-converted to a baseband signal $r_b(t)$. Then $r_b(t)$ is converted to discrete-time signal $r[n]$ before the receiver makes a decision on the transmitted symbols and obtain $\hat{x}[n]$

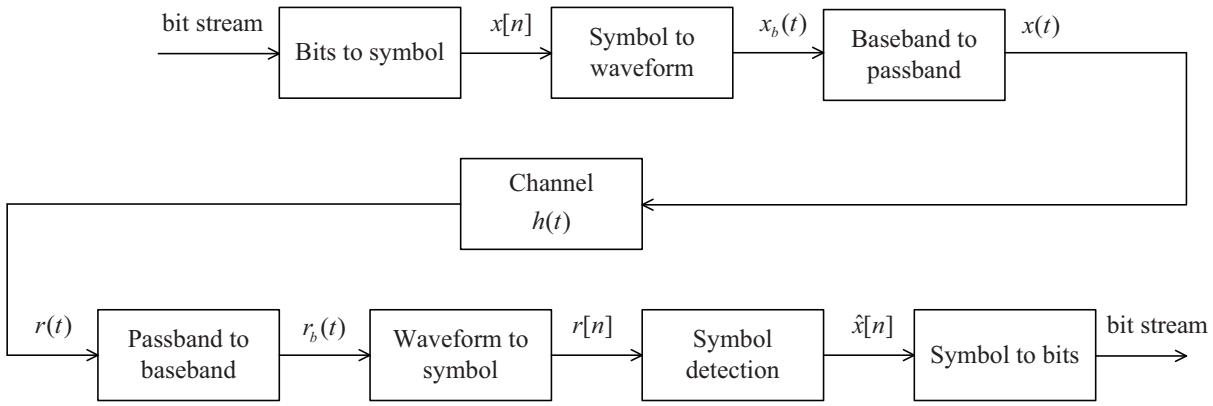

Figure 2.2: Block diagram of a digital communication system.

(symbol detection). Finally, the symbol-to-bits block maps the symbols $\hat{x}[n]$ back to the bit stream.

This chapter will provide more details of the signal processing tasks that are illustrated in Figure 2.2. First, a single-carrier QAM (SC-QAM) system is presented in Section 2.1. The limitation of a single carrier system is discussed, which then motivates the development of multicarrier systems. The well-known multicarrier system, orthogonal frequency division multiplexing (OFDM), is presented in Section 2.2. An alternative multicarrier scheme, which is based on the filter banks technique, called filter bank multicarrier offset QAM (FBMC-OQAM), is presented in Section 2.3. A comparision between FBMC-OQAM and OFDM is also provided in that section.

2.1 Single Carrier QAM System (SC-QAM)

Figure 2.3 illustrates a SC-QAM system. This system transmits two bit streams simultaneously by changing the amplitudes of two quadrature carriers, hence the name quadrature amplitude modulation. The transmitted QAM signal can be expressed as

$$x(t) = \sum_{n=-\infty}^{+\infty} x_I[n] p_T(t - nT) \cos(2\pi f_c t) - \sum_{n=-\infty}^{+\infty} x_Q[n] p_T(t - nT) \sin(2\pi f_c t) \tag{2.1}$$

where $x_I[n]$ and $x_Q[n]$ are the signal amplitudes (which are real values) of the quadrature carriers, $p_T(t)$ is the pulse shaping filter and T is the symbol period. Alternatively, the

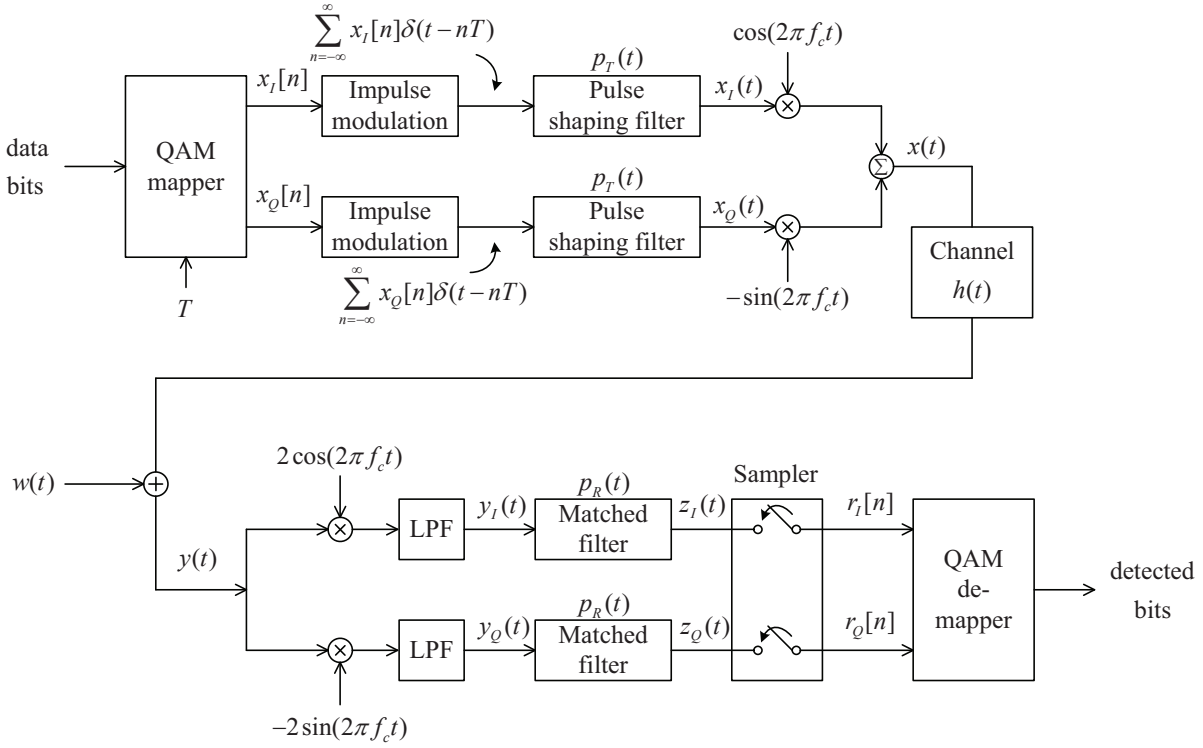

Figure 2.3: Block diagram of a single carrier QAM system.

transmitted QAM signal can be expressed as

$$x(t) = \mathcal{R}\Big\{ \sum_{n=-\infty}^{+\infty} x[n] p_T(t - nT) e^{j2\pi f_c t} \Big\} \tag{2.2}$$

where $x[n] = x_I[n] + j x_Q[n]$. From this representation, the two amplitudes ($x_I[n]$, $x_Q[n]$) transmitted on two quadrature carriers can be collectively expressed as a complex symbol $x[n]$. In a rectangular M-QAM system with $M = 2^k$, a group of $\Lambda = \Lambda_I + \Lambda_Q$ bits is mapped to a symbol of the form

$$x = \pm(2k+1)\Delta \pm j(2l+1)\Delta, \quad \text{where} \quad \begin{cases} k \in \{0, 1, \ldots, 2^{\Lambda_I} - 1\} \\ l \in \{0, 1, \ldots, 2^{\Lambda_Q} - 1\} \end{cases} . \tag{2.3}$$

The set of all possible complex symbols $x[n]$ can be described in a two dimensional diagram as depicted in Figure 2.4 for $M = 4$ and $M = 16$. Such a diagram is called a QAM constellation. The mapping from bits to symbols, called Gray coding, is done such that the adjacent symbols differ by only one bit. This mapping ensures that an error between adjacent constellation points, which is the most probable error, results in only one bit error.

The minimum distance between any two constellation points is 2Δ. The average symbol energy of the M-QAM constellation, denoted as E_s, is defined as the average of the distance squared over all the signal points in the constellation. When Λ is even, it can be shown that [9]:

$$E_s = \frac{2\Delta^2}{3}(2^\Lambda - 1) \tag{2.4}$$

The transmission channel is modelled as a continuous-time linear time invariant (LTI) system with an impulse response $h(t)$. Then the input-output relationship is expressed as

$$y(t) = x(t) * h(t) + w(t), \tag{2.5}$$

where $*$ denotes linear convolution, and $w(t)$ represents zero-mean additive white Gaussian noise (AWGN) with power spectral density $N_0/2$.

At the receiver, the RF input $y(t)$ is mixed with $2\cos(2\pi f_c t)$ and $-2\sin(2\pi f_c t)$ followed by low pass filters to obtain $y_I(t)$ and $y_Q(t)$. Then those signals are filtered by a matched filter with impulse response $p_R(t)$, which produces $z_I(t)$ and $z_Q(t)$. The resulted signals are uniformly sampled every T seconds to produce discrete time signals $r_I[n]$ and $r_Q[n]$. Finally, the QAM demapper makes a decision on which symbols are transmitted based on $r_I[n]$ and $r_Q[n]$, and then demaps the detected symbols back to bits.

Given that the QAM transmitted signal can be expressed as in (2.2), an equivalent representation of the transmitter is given as in Figure 2.5, where the complex baseband signal $x_b(t)$ is defined as

$$\begin{aligned} x_b(t) &= x_I(t) + jx_Q(t) \\ &= \sum_{n=-\infty}^{+\infty} x_I[n]p_T(t-nT) + j\sum_{n=-\infty}^{+\infty} x_Q[n]p_T(t-nT) \\ &= \sum_{n=-\infty}^{+\infty} x[n]p_T(t-nT). \end{aligned} \tag{2.6}$$

Likewise, the receiver in Figure 2.3 can be equivalently represented as shown in Figure 2.5, where $y_b(t) = y_I(t) + jy_Q(t)$, $z_b(t) = z_I(t) + jz_Q(t)$, and $r[n] = r_I[n] + jr_Q[n]$.

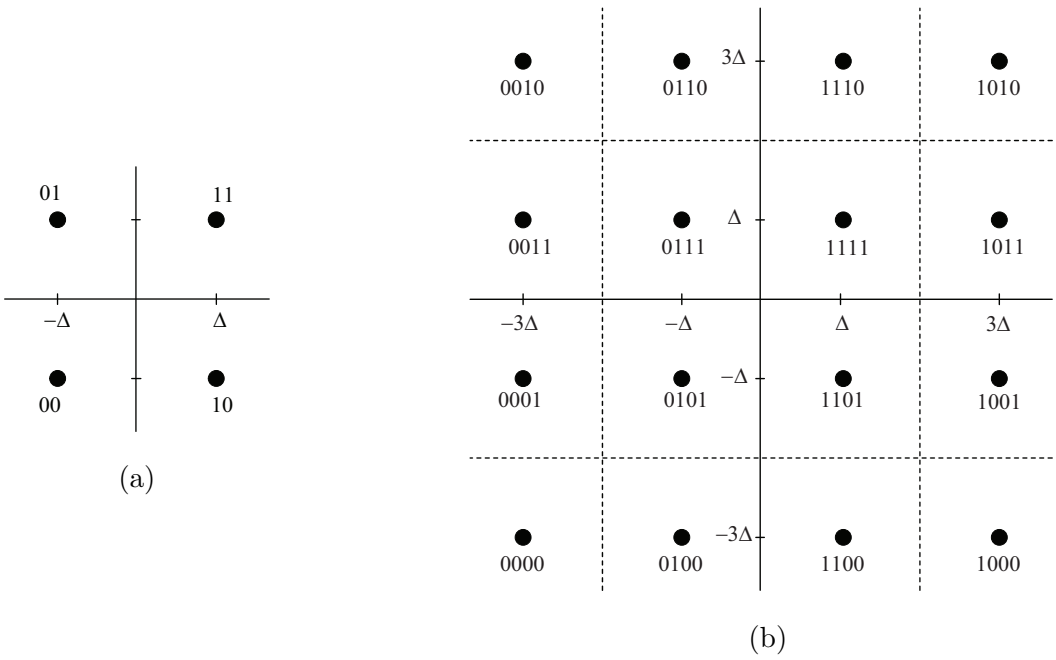

Figure 2.4: QAM constellations (a) QPSK (b) 16-QAM.

Equation (2.5) expresses the input/output relationship of a passband system. Since $x(t)$, $y(t)$, $h(t)$, and $w(t)$ are passband signals, they have baseband equivalent signals denoted by $x_b(t)$, $y_b(t)$, $h_b(t)$, and $w_b(t)$ where

$$\begin{aligned} x(t) &= \mathcal{R}\Big\{x_b(t)e^{j2\pi f_c t}\Big\} \\ y(t) &= \mathcal{R}\Big\{y_b(t)e^{j2\pi f_c t}\Big\} \\ h(t) &= \mathcal{R}\Big\{h_b(t)e^{j2\pi f_c t}\Big\} \\ w(t) &= \mathcal{R}\Big\{w_b(t)e^{j2\pi f_c t}\Big\} \end{aligned} \tag{2.7}$$

It has been shown in [9] that the input-output relationship between the baseband equivalent signals is similar to (2.5) and it is expressed as

$$y_b(t) = x_b(t) * h_b(t) + w_b(t). \tag{2.8}$$

The complex baseband equivalent channel model is illustrated in Figure 2.6.

To derive the equivalent discrete-time channel model that relates $x[n]$ to $r[n]$, consider

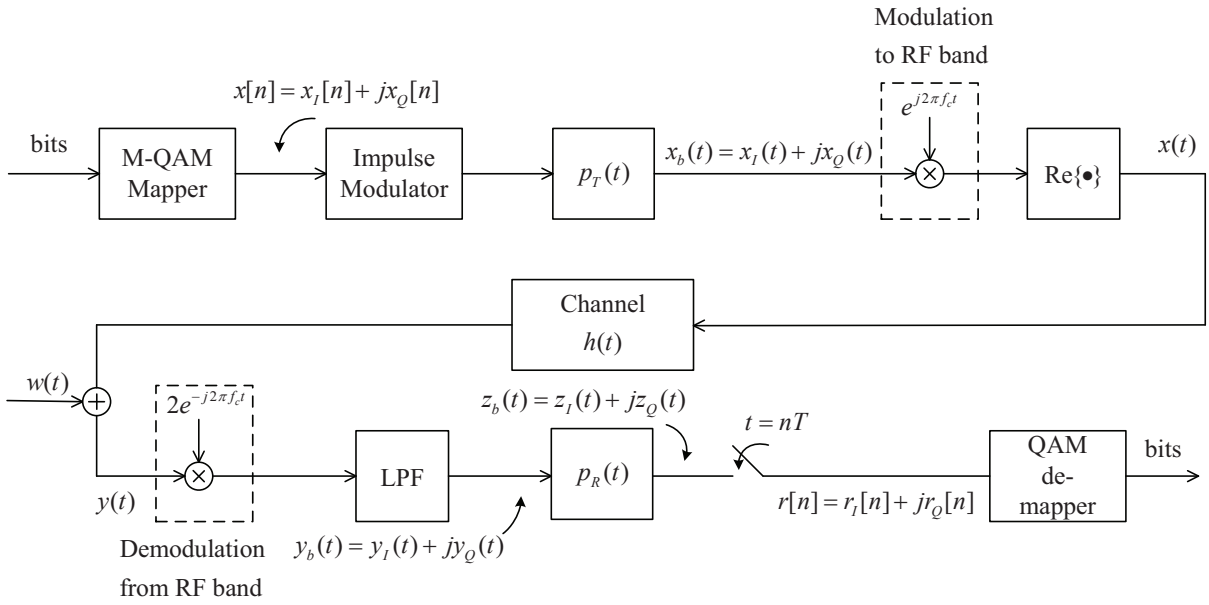

Figure 2.5: Representation of a SC-QAM system using complex baseband equivalent signals.

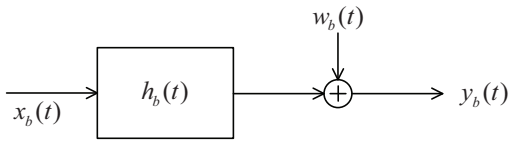

Figure 2.6: Complex baseband-equivalent channel model.

the signal $z_b(t)$ at the output of the receiver's matched filter, which is expressed as

$$\begin{aligned} z_b(t) = y_b(t) * p_R(t) &= x_b(t) * h_b(t) * p_R(t) + w_b(t) * p_R(t) \\ &= \sum_{k=-\infty}^{\infty} x[k] p_T(t - kT) * h_b(t) * p_R(t) + w_b(t) * p_R(t) \end{aligned} \tag{2.9}$$

Then $z_b(t)$ is uniformly sampled every T seconds to produce the discrete-time output $r[n] = z_b(nT)$. Define the effective continuous-time channel and effective noise, respectively, as follows:

$$h_e(t) = p_T(t) * h_b(T) * p_R(t) \quad \text{and} \quad w_e(t) = w_b(t) * p_R(t). \tag{2.10}$$

Then the received discrete-time signal is

$$r[n] = \sum_{k=-\infty}^{\infty} x[k] h_e(nT - kT) + w_e(nT). \tag{2.11}$$

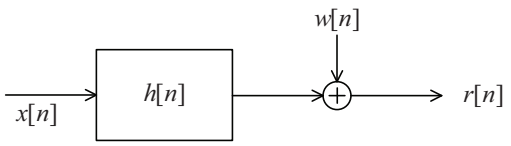

Figure 2.7: Equivalent discrete-time channel model.

The above expression can be rewritten as

$$r[n] = \sum_{k=-\infty}^{\infty} x[k]h[n-k] + w[n], \tag{2.12}$$

where $h[n]$ and $w[n]$ are, respectively, the discrete-time equivalent channel and noise given by

$$\begin{aligned} h[n] &= p_T(t) * h_b(t) * p_R(t)\Big|_{t=nT}, \\ w[n] &= w_b(t) * p_R(t)\Big|_{t=nT}. \end{aligned} \tag{2.13}$$

Thus, the system shown in Figure 2.6 can be represented as in Figure 2.7, which contains only discrete-time signals and system.

When an SC-QAM system operates in a channel with the input-output relationship expressed as in (2.12), the received signal $r[n]$ at time slot n not only depends on the transmitted signal $x[n]$, but also depends on the past symbols $x[n-1], x[n-2], \ldots$. This phenomenon is called intersymbol interference (ISI) and needs to be addressed. In the following, one approach to deal with ISI in an SC-QAM system is presented.

Equation (2.12) can be rewritten as

$$r[n] = x[n]h[0] + \sum_{k \neq n} x[k]h[n-k] + w[n], \tag{2.14}$$

where the term $x[n]h[0]$ is the desired information symbol at the time slot n, and the term $\sum_{k\neq n} x[k]h[n-k]$ represents ISI. It is noted that $h[n]$ is the sample of $h_e(t) = p_T(t) * h_b(t) * p_R(t)$ at time slot n. Thus, in order to have zero ISI, one should have

$$h_e(nT) = \begin{cases} 1, & n = 0 \\ 0, & \text{otherwise} \end{cases}. \tag{2.15}$$

Denote $H_e(f)$ as the frequency response of $h_e(t)$. Then the condition in (2.15) is satisfied if [22]

$$\sum_{n=-\infty}^{\infty} H_e\left(f + \frac{n}{T}\right) = T \quad \text{for } |f| \leq \frac{1}{2T}. \tag{2.16}$$

Equation (2.16) means that if one designs $h_e(t)$ such that $H_e(f)$ and its aliases (resulted from sampling $h_e(t)$) add up to a constant value in frequency band $|f| \leq 1/2T$, then zero ISI is achieved. This is known as Nyquist's first criterion.

One is faced with the problem of finding $h_e(t)$ such that its frequency response $H_e(f)$ satisfies the Nyquist's criterion. Figure 2.8 illustrates which shape and bandwidth $H_e(f)$ should have to satisfy (2.16).

- The upper part of Figure 2.8 illustrates a case where the bandwidth of $H_e(f)$ is less than $1/2T$. Due to sampling (every T seconds), $H_e(f)$ is shifted to $\pm\frac{n}{T}$. In this case, there is no overlap between $H_e(f)$ and its shifted version. Thus, one can see that there is no shape of $H_e(f)$ such that (2.16) is satisfied.

- The center part of Figure 2.8 illustrates a case where the bandwidth of $H_e(f)$ is exactly equal to $1/2T$. In this case, there is also no overlap between $H_e(f)$ and its aliases. However, due to the critical value of the bandwidth, there is one shape of $H_e(f)$ which is a rectangular such that (2.16) is satisfies. The corresponding impulse response $h_e(t)$ is a sinc function, which is

$$h_e(t) = \sin(\pi t/T)/(\pi t/T). \tag{2.17}$$

- The lower part of Figure 2.8 illustrates a case where the bandwidth of $H_e(f)$ is great than $1/2T$. In this case, it is obvious that aliasing occurs. However, there is an infinite number of $H_e(f)$ that satisfies (2.16) as long as its shape has a certain symmetry about the point $1/2T$ as shown in the figure. One popular set of $H_e(f)$ which satisfies (2.16) is the raise-cosine function shown in Figure 2.9 with the corresponding impulse response

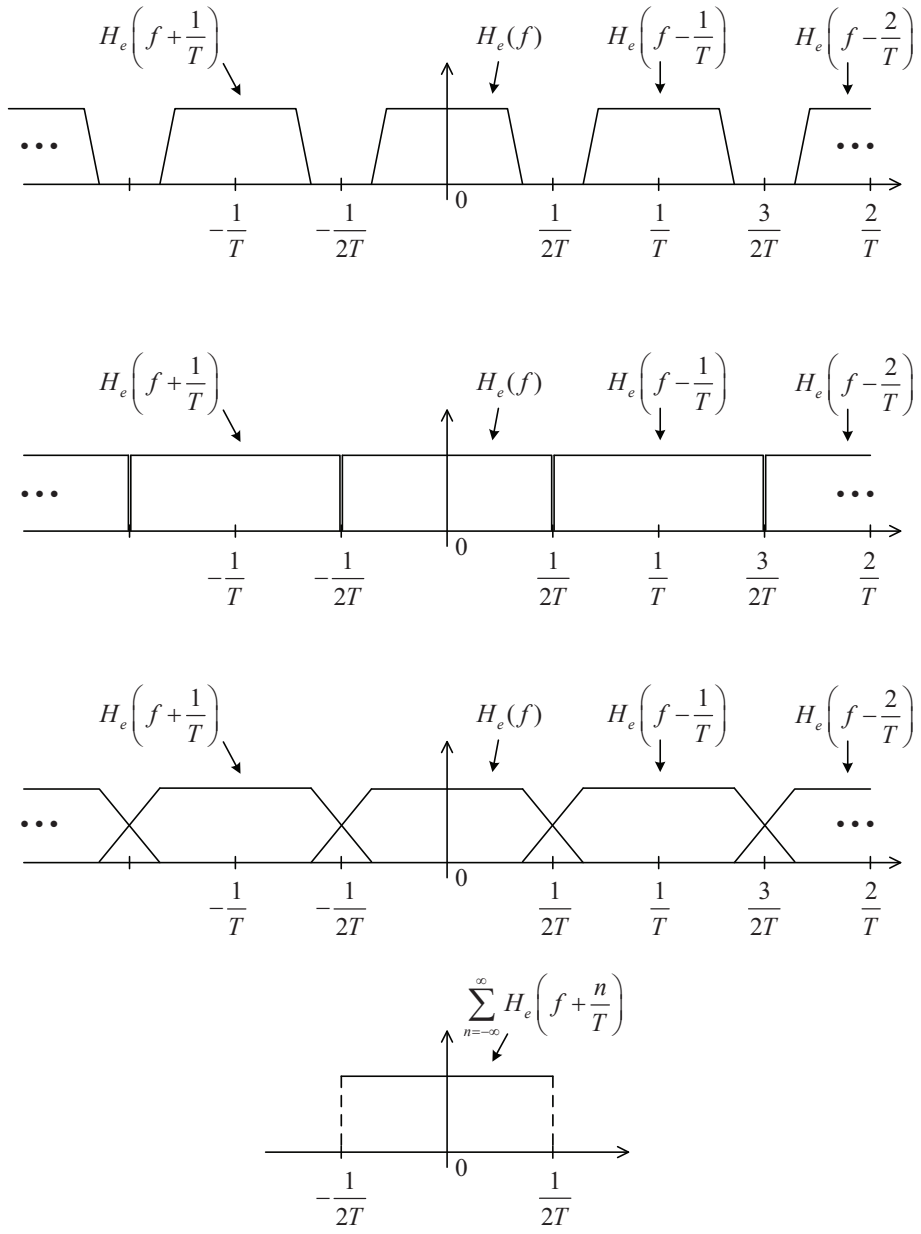

Figure 2.8: Condition on $H_e(f)$ to achieve zero ISI.

shown in Figure 2.10. It is given as [22]

$$H_e(f) = H_{\mathrm{RC}}(f) = \begin{cases} T, & |f| \le \frac{1-\beta}{2T} \\ T\cos^2\left[\frac{\pi T}{2\beta}\left(|f| - \frac{1-\beta}{2T}\right)\right], & \frac{1-\beta}{2T} \le |f| \le \frac{1+\beta}{2T} \\ 0, & |f| \ge \frac{1+\beta}{2T} \end{cases} . \tag{2.18}$$

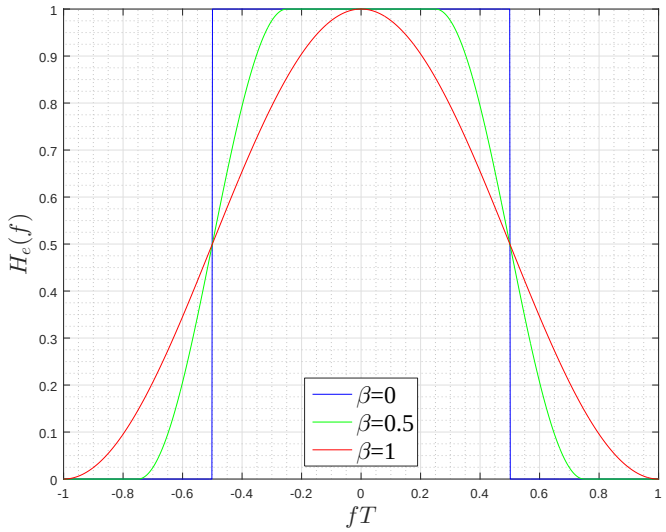

Figure 2.9: The raised-cosine spectrum

The impulse response is given by

$$h_e(t) = \text{sinc}(t/T)\frac{\cos(\pi\beta t/T)}{1-4\beta^2t^2/T^2}, \tag{2.19}$$

where β is the roll-off factor, which controls the excess bandwidth.

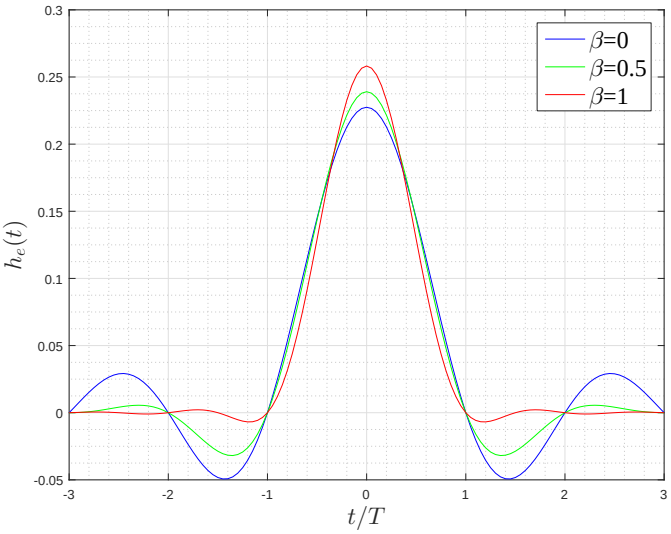

Figure 2.10: Time domain function of the raised-cosine spectrum

Recall that $H_e(f) = H_T(f)H_b(f)H_R(f)$ is the overall frequency response and one knows what $H_e(f)$ must be such that zero-ISI is achieved. For a given choice of a $H_b(f)$, such as a raised-cosine spectrum, one still needs to find out what are the optimal designs of $H_T(f)$

and $H_R(f)$. However, the optimal design in what sense should be stated first. It is noted that the design of $H_R(f)$ not only affects the ISI term but also the noise. It will be shown later that the probability of error is determined by the signal-to-noise ratio (SNR). Thus, the choice of $H_R(f)$ affects the probability of error. Therefore, the design problem is an optimization problem which is stated

$$\begin{array}{ll} \underset{H_T(f),H_R(f)}{\text{minimize}} & \text{probability of error} \\ \text{subject to} & \text{transmitted power } P_T \\ & H_T(f)H_b(f)H_R(f) \text{ satisfies zero-ISI criterion} \end{array} \tag{2.20}$$

If the noise has a flat PSD over the channel bandwidth, then the solution for the above problem is given as [22]

$$\begin{aligned} |H_R(f)|^2 &= K_1 \frac{|H_e(f)|}{|H_b(f)|}, \\ |H_T(f)|^2 &= K_2 \frac{|H_e(f)|}{|H_b(f)|} = \frac{K_2}{K_1}|H_R(f)|^2, \end{aligned} \tag{2.21}$$

where K_1, and K_2 are arbitrary constant which set the power levels at the transmitter and the receiver. In addition, the phases of $H_T(f)$ and $H_R(f)$ should cancel each other, which implies that the transmit and receive filters are a matched-filter pair.

In the special case where the channel is ideal, i.e., $H_b(f) = 1$ for $|f| \leq W$ where W is the channel bandwidth and $K_1 = K_2$, one obtains $|H_T(f)| = |H_R(f)| = \sqrt{|H_e(f)|}/\sqrt{K_1}$. If $H_e(f)$ is a raise-cosine spectrum and $K_1 = 1$, then $H_T(f)$ and $H_R(f)$ are square-root raised-cosine (SRRC) spectrum:

$$H_T(f) = H_R(f) = \begin{cases} \sqrt{T}, & |f| \leq \frac{1-\beta}{2T} \\ \sqrt{T}\cos\left[\frac{\pi T}{2\beta}\left(|f| - \frac{1-\beta}{2T}\right)\right], & \frac{1-\beta}{2T} \leq |f| \leq \frac{1+\beta}{2T} \\ 0, & |f| \geq \frac{1+\beta}{2T} \end{cases}. \tag{2.22}$$

The impulse response of SRRC is shown in Figure 2.11 and is given as [22]

$$h_T(t) = h_R(t) = \frac{4\beta t/T \cos[\pi(1+\beta)t/T] + \sin[\pi(1-\beta)t/T]}{(\pi t/T)[1-(4\beta t/T)^2]} \tag{2.23}$$

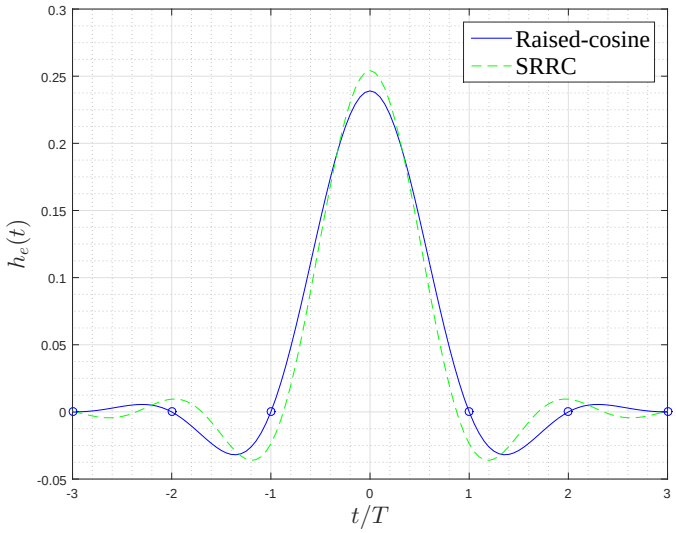

Figure 2.11: A Raised-cosine and SRRC impulse response with $\beta = 0.5$

The impulse response of an RC filter is also shown in Figure 2.11 to illustrate the difference between SRRC and RC filters. It is pointed out that the RC pulse satisfies the Nyquist criterion since its impulse response crosses zero at multiples of T, whereas the SRRC pulse does not.

When one designs the system to eliminate ISI, (2.12) is rewritten as:

$$r[n] = x[n] + w[n]. \tag{2.24}$$

Equation (2.24) is the input output relation of an AWGN channel, where there is no ISI and the transmission errors come from the channel noise only. In the following, statistical properties of the noise term $w[n]$ are discussed and then the performance of a SC-QAM system in an AWGN channel is derived.

The continuous time noise process $w(t)$ in (2.5) is modeled as a zero-mean wise sense stationary (WSS) white Gaussian random process. Since $w(t)$ is a WSS process, its power spectrum density $S_w(f)$ is the Fourier transform of its autocorrelation $R_w(\tau)$. In addition, $w(t)$ is white, then $S_w(f) = \frac{N_0}{2}$ for all f leading to $R_w(\tau) = \frac{N_0}{2}\delta(\tau)$. Thus, one has

$$E\{w(t_1)w^*(t_2)\} = \begin{cases} \dfrac{N_0}{2}, & \text{if } t_1 = t_2 \\ 0, & \text{otherwise.} \end{cases} \tag{2.25}$$

The white noise $w(t)$ is down-converted, filtered at baseband and sampled. Notice that the power spectrum density of $w_b(t) * p_R(t)$ is $S_{w,\text{filtered}}(f) = N_0/2|P_R(f)|^2$. Due to the sampling theorem, the power spectrum density of $w[n]$ is [9]

$$\sum_{n=-\infty}^{\infty} \frac{N_0}{2T}\left|P_R\left(\frac{f}{f_s}-n\right)\right|^2 = \sum_{n=-\infty}^{\infty} \frac{N_0}{2T}\left|P_R\left(\hat{f}-n\right)\right|^2 \tag{2.26}$$

where $f_s = 1/T$ and $\hat{f} = f/f_s$ is the normalized digital frequency with units cycles/sample. Thus, if $P_R(f)$ is a SRRC frequency response as given in (2.22), one has

$$\sum_{n=-\infty}^{\infty} \frac{1}{T}\left|P_R(f-nf_s)\right|^2 = 1. \tag{2.27}$$

Then the power spectral density of the discrete-time noise process $w[n]$ is a constant $\frac{N_0}{2}$, i.e., white. In addition, the real and imaginary components of $w[n]$ are i.i.d. Gaussian with variances $N_0/2$ [7]. Thus, $w[n]$ is a zero-mean complex Gaussian random variable with variance N_0, denoted as $w \sim \mathcal{CN}(0, N_0)$.

Suppose that an M-QAM symbol x is transmitted through an AWGN channel as modelled in (2.24). For notation simplicity, the time index n is dropped and the received signal at any specific time slot is written as $r = x + w$, where $w \sim \mathcal{CN}(0, N_0)$. Assume that x and w are independent. The conditional probability density function (pdf) of the received signal r given that x is transmitted is

$$f_{r|x}(r|x) = f_{r|x}(x + w|x) = f_w(r - x) \tag{2.28}$$

where $f_w(w)$ is the Gaussian pdf, given by

$$f_w(w) = \frac{1}{\pi N_0} e^{-|w|^2/N_0} \tag{2.29}$$

Based on the observation of received signal r, the optimal decision rule to decide which x is transmitted is the maximum a posterior probability (MAP) rule [9] and given as

$$\hat{x} = \arg\max_x f_{x|r}(x|r) \tag{2.30}$$

Since all the constellation points are equiprobable, and using Equations (2.28), (2.29), the

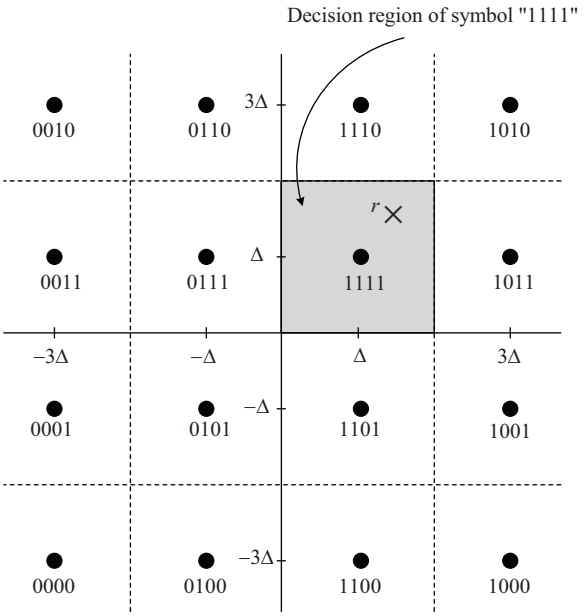

Figure 2.12: Minimum-distance decision regions of 16-QAM.

MAP rule can be expressed as

$$\begin{aligned}
\hat{x} &= \arg\max_x f_{x|r}(x|r) \\
&= \arg\max_x \frac{f_{r|x}(r|x)f_x(x)}{f_r(r)} \\
&= \arg\max_x f_{r|x}(r|x) \\
&= \arg\max_x f_w(r-x) \\
&= \arg\max_x \frac{1}{\pi N_0} e^{-|r-x|^2/N_0} \\
&= \arg\min_x |r-x|
\end{aligned} \tag{2.31}$$

The final expression in (2.31) implies that the receiver relies on the observation r and looks among all possible x to find the one that is closest to r. Such a rule is called a nearest-neighbor decision rule or the minimum-distance rule.

Figure 2.12 depicts a 16-QAM constellation together with the minimum-distance decision boundary. Using the minimum-distance receiver, the two dimensional plane containing the signal constellation is divided into regions, where each region is associated with one QAM symbol. For example, the shaded area in Figure 2.12 illustrates the decision region of symbol

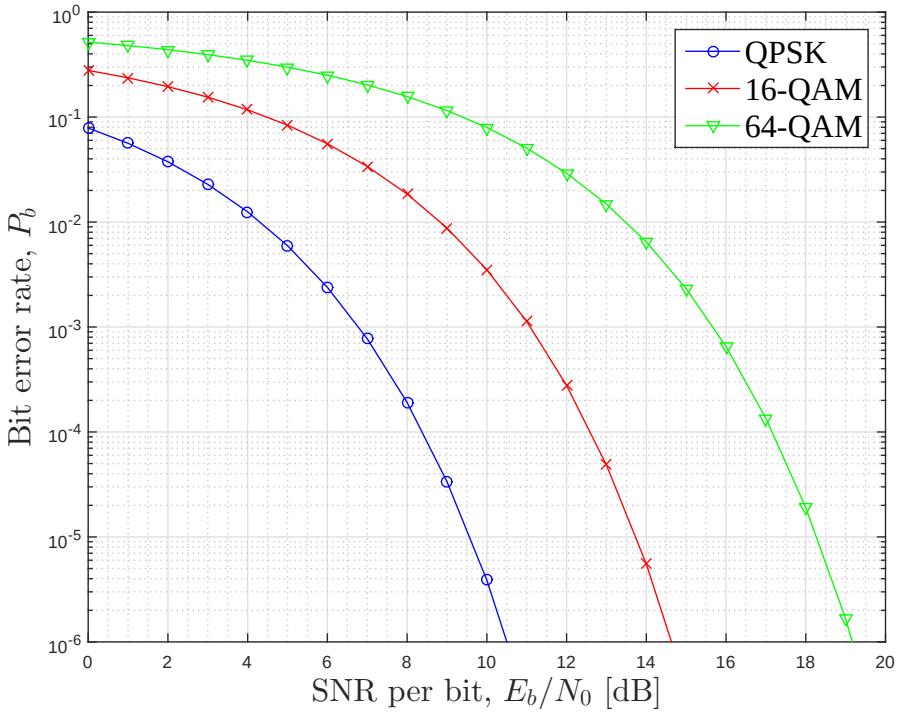

Figure 2.13: Bit error rates for different QAM systems.

(1111). The received signal r, due to noise, could be a random point in the two dimension plane. If r falls into the shaded area, then the QAM symbol (1111) is decided to be the transmitted symbol.

To derive the probability of error for a QAM system under an AWGN channel, one must specify the signal constellation. This thesis considers rectangular QAM constellations. Although they are not the best M-QAM signal constellations for $M \geq 16$, the average transmitted power required to achieve a given minimum distance is only slighly greater than the average power required for the best M-QAM signal constellation [9]. In addition, a rectangular QAM signal constellation has the distinct advantage of being easily generated as two ASK signals transmitted on the in-phase and quadrature carriers.

For a square QAM constellation where $M = 2^\lambda$ with λ even, the probability of symbol error can be derived exactly and given as [9]

$$P_{s,QAM} = 4\left(1 - \frac{1}{\sqrt{M}}\right) Q\left(\sqrt{\frac{3\gamma_s}{(M-1)}}\right), \tag{2.32}$$

where $\gamma_s = E_s/N_0$ is the signal to noise (SNR) ratio per symbol and E_s is defined as in

(2.4). If one uses Gray mapping to map the real and imaginary parts, respectively, any QAM symbol and its neighbors will differ only by one bit. In this case, the bit error rate (BER) of the M-QAM system can be approximated by

$$\begin{aligned} P_{b,QAM} &= \frac{1}{\log_2(M)} P_{s,QAM}. \\ &= \frac{4}{\log_2(M)} \left(1 - \frac{1}{\sqrt{M}}\right) Q\left(\sqrt{\frac{3\gamma_b \log_2(M)}{(M-1)}}\right), \end{aligned} \tag{2.33}$$

where $\gamma_b = \gamma_s / \log_2(M)$ is the SNR per bit.

Figure 2.13 shows the BER plots of QPSK, 16-QAM, and 64-QAM systems under the AWGN channel. Notice that to achieve the same level of error rate the QAM system with larger M requires more power. For example, at the level of $P_b = 10^{-6}$, the gap between 16-QAM and 64-QAM is around 5dB. This means that the transmit power needs to be increased by 5dB in order to send two additional bits per symbol while maintaining the same quality of service, at $P_b = 10^{-6}$.

Designing the transmit and receive filters as discussed is one approach to deal with ISI. Another approach is that one does not design the system to eliminate ISI but design the demodulator, with the ISI present, that best reconstructs the transmitted sequence [22]. Reference [9] demonstrates that an optimum demodulator can be realized as a filter matched to the overall impulse response of the chain: modulator/transmit filter/channel, followed by a sampler operating at the symbol rate and subsequent maximum-likelihood (ML) detection for estimating the transmitted sequence from the sample values. The optimal ML detection can be implemented using the Viterbi algorithm. However, the complexity of the Viterbi algorithm grows exponentially with the number of channel taps. Alternatively, sub-optimal demodulators which have lower complexity and yield comparable performance can be considered. Some candidates are linear equalizers such as the zero-forcing and minimum mean square error equalizers, which involve simple linear operations on the received symbols followed by simple hard detection.

Another popular alternate approach to deal with ISI is to use signal processing techniques at the transmitter and receiver to convert the ISI channel into non ISI parallel subchannels

such that each transmitted signal on a subchannel only experiences a constant gain channel, and thus a simple scalar equalizer for each subchannel is adequate. This method is commonly known as orthogonal frequency division multiplexing (OFDM), which is the topic of Section 2.2.

2.2 OFDM System

As discussed in the previous section, when transmitting a SC-QAM signal over a frequency selective channel which is modelled as a FIR filter with length V, ISI occurs. To deal with ISI, a popular approach is to transmit the information symbols in blocks and inserting guard symbols between blocks. As long as the length of the guard interval is larger than $V-1$, then ISI can be eliminated. The guard symbols could be zeroes, which results in a zero-padding (ZP) system, or it could be a repetition of the end of a block, which results in a cyclic-prefix (CP) system. The two systems have their own advantages and weaknesses, and have been compared extensively in [23].

This thesis only considers the CP system. In this section, first, it is shown that adding a CP at the transmitter and discarding it at the receiver can completely remove ISI. In addition, using CP turns linear convolution involving a frequency-selective multipath channel to circular convolution. The benefit of circular convolution is that its matrix representation is a circulant matrix, which can be diagonalized by Discrete Fourier Transform (DFT) and Inverse Discrete Fourier Transform (IDFT) matrices. Next, a CP-OFDM system is presented. Two main properties of this system are highlighted, which are efficient implementation using DFT and IDFT, and simple scalar equalization. At the end of this section, a drawback of OFDM concerning the power spectral density is discussed. That drawback motivates the development of FBMC-OQAM, which is discussed in Section 2.3.

Given a discrete time channel model represented with a V-taps FIR $h[n]$, the received signal is expressed as

$$r[n] = \sum_{k=0}^{V-1} h[k]x[n-k] + w[n]. \tag{2.34}$$

When transmitting over a frequency selective channel, it is useful to transmit the information

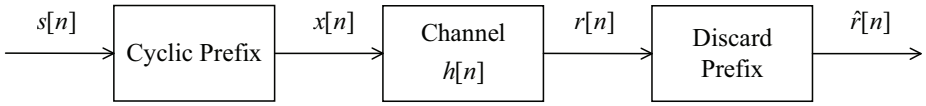

Figure 2.14: Transmission scheme using a CP.

symbols in blocks [11]. In particular, the transmitted sequence $x[n]$ is grouped into blocks of length P ($P \gg V$). The ith transmitted block and received block are denoted as $\mathbf{x}[i] = [x[iP], x[iP+1], \ldots, x[iP+P-1]]^{\mathrm{T}}, \mathbf{r}[i] = [r[iP], r[iP+1], \ldots, r[iP+P-1]]^{\mathrm{T}}$, respectively.

One can verify that (2.34) can be represented in a matrix form as

$$\mathbf{r}[i] = \mathbf{H}_0\mathbf{x}[i] + \mathbf{H}_1\mathbf{x}[i-1] + \mathbf{w}[i], \tag{2.35}$$

where

$$\mathbf{H}_0 = \begin{bmatrix} h[0] & 0 & 0 & \ldots & 0 \\ \vdots & h[0] & 0 & \ldots & 0 \\ h[V-1] & \ldots & \ddots & \ldots & \vdots \\ \vdots & \ddots & \ldots & \ddots & 0 \\ 0 & \ldots & h[V-1] & \ldots & h[0] \end{bmatrix} \tag{2.36}$$

$$\mathbf{H}_1 = \begin{bmatrix} 0 & \ldots & h[V-1] & \ldots & h[1] \\ \vdots & \ddots & 0 & \ddots & \vdots \\ 0 & \ldots & \ddots & \ldots & h[L] \\ \vdots & \vdots & \vdots & \ddots & \vdots \\ 0 & \ldots & 0 & \ldots & 0 \end{bmatrix}, \tag{2.37}$$

and $\mathbf{w}[i] = [w[iP], w[iP+1], \ldots, w[iP+P-1]]^{\mathrm{T}}$. Equations (2.35) implies that the current received block depends on both the current and previous transmitted blocks. This is commonly referred to as interblock interference (IBI) which is the same in nature as ISI. Further, only the first $V-1$ samples of each received block are corrupted by the previous transmitted block. Therefore, IBI can be removed by discarding the first $V-1$ samples of each received block.

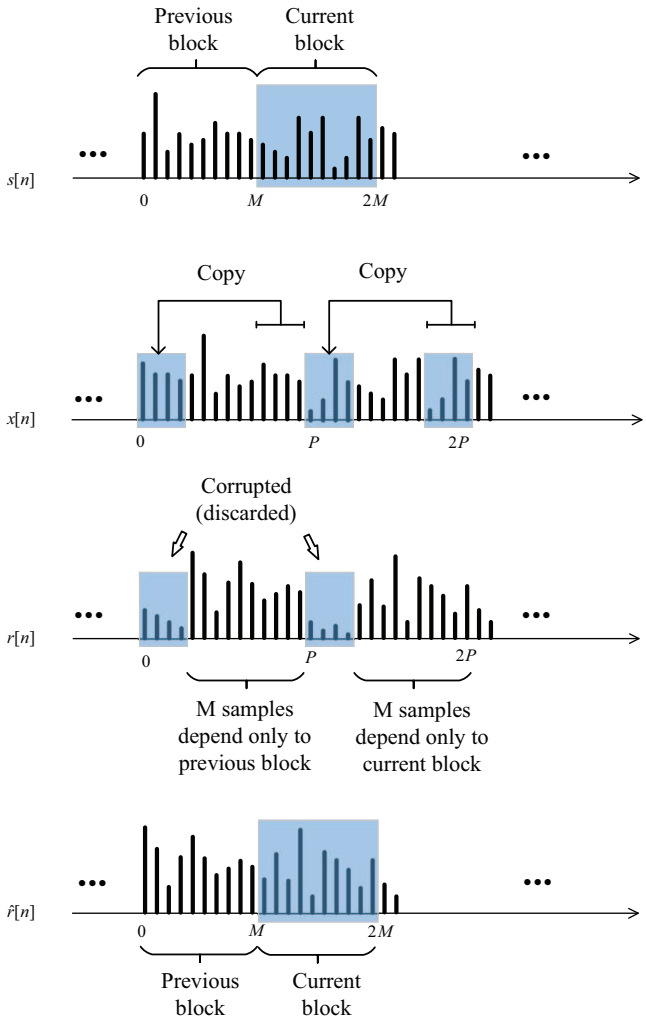

Figure 2.15: Illustration of how the CP is added and how IBI is eliminated in the CP system for the case of $M = 10$, $L = 4$, and $V = 5$.

Figure 2.14 shows a system that employs the cyclic-prefix scheme to transmit $\mathbf{s}[i]$, a block of length M. At the transmitter, the last L ($L \leq M$) samples at the end of $\mathbf{s}[i]$ are copied and placed at the beginning, where L is the CP length. The new block $\mathbf{x}[i]$ has length $P = M + L$. The cyclic-prefixed block $\mathbf{x}[i]$ is sent over the channel with the input output relation as in (2.35). As the channel has V taps, the first $V - 1$ samples of each received block are corrupted by the previous transmitted block. These contaminated samples are discarded, and this operation is denoted by a box labeled "Discard Prefix". After discarding the prefix, the obtained block $\hat{\mathbf{r}}[i]$ has length M, and only depends on the current transmitted block $\mathbf{s}[i]$. The process of adding CP at the transmitter and discarding it at the receiver is

illustrated in Figure 2.15. The length of the CP is chosen such that $L \geq V-1$ in order to completely eliminate IBI.

The process of adding CP at the transmitter and removing CP at the receiver can be expressed using matrices $\mathbf{T}_{\text{CP}}$, and $\mathbf{R}_{\text{CP}}$, respectively. The CP insertion can be described by choosing

$$\mathbf{T}_{\text{CP}} = \begin{bmatrix} \bar{\mathbf{I}}_L \\ \mathbf{I}_M \end{bmatrix}, \tag{2.38}$$

which is a concatenation of the last L rows of an $M \times M$ identity matrix $\bar{\mathbf{I}}_L$, and the identity matrix $\mathbf{I}_M$ itself. The CP discarding is carried out by the operation of matrix

$$\mathbf{R}_{\text{CP}} = \begin{bmatrix} \mathbf{0}_{M\times L} & \mathbf{I}_M \end{bmatrix}. \tag{2.39}$$

The received signal block after discarding CP can be expressed as

$$\hat{\mathbf{r}}[i] = \mathbf{R}_{\text{CP}}\mathbf{H}_0\mathbf{T}_{\text{CP}}\mathbf{s}[i] + \mathbf{R}_{\text{CP}}\mathbf{H}_1\mathbf{s}[i-1] + \hat{\mathbf{w}}[i], \tag{2.40}$$

where the noise vector $\hat{\mathbf{w}}[i] = \mathbf{R}_{\text{CP}}\mathbf{w}[i]$ contains the last M elements of $\mathbf{w}[i]$. One can verify that $\mathbf{R}_{\text{CP}}\mathbf{H}_1 = \mathbf{0}_{M\times P}$, which means that IBI is eliminated by discarding the CP. Furthermore, the join operation of $\mathbf{R}_{\text{CP}}$ and $\mathbf{T}_{\text{CP}}$ on $\mathbf{H}_0$ creates an $M \times M$ circulant matrix [24]:

$$\mathbf{H}_{\text{circ}} = \begin{bmatrix} h[0] & 0 & \dots & \dots & h[V-1] & \dots & h[1] \\ h[1] & h[0] & & & & \ddots & \vdots \\ \vdots & & \ddots & & & & h[V-1] \\ h[V-1] & & \ddots & \ddots & & & 0 \\ 0 & \ddots & & \ddots & h[0] & & \vdots \\ \vdots & \ddots & \ddots & & & \ddots & 0 \\ 0 & \dots & 0 & h[V-1] & \dots & h[1] & h[0] \end{bmatrix}, \tag{2.41}$$

where the mth column is obtained by shifting down the leftmost (0th) column by m. Using $\mathbf{H}_{\text{circ}}$ the input/output relationship in Figure 2.14 is given as

$$\mathbf{r}[i] = \mathbf{H}_{\text{circ}}\mathbf{s}[i] + \hat{\mathbf{w}}[i]. \tag{2.42}$$

It should be noted that the operation $\mathbf{H}_{\text{circ}}\mathbf{s}[i]$ is equivalent to circular convolution of $\mathbf{s}[i]$ and the leftmost column of $\mathbf{H}_{\text{circ}}$ [25]. Therefore, Equation (2.42) shows that by inserting the CP at the transmitter and discarding the CP at the receiver, the linear convolution with the channel (which results in IBI) in (2.35) is converted to a circular convolution and IBI is eliminated.

The matrix $\mathbf{H}_{\text{circ}}$ can be diagonalized by DFT and IDFT matrices as

$$\mathbf{H}_{\text{circ}} = \mathbf{F}^H \mathbf{\Gamma} \mathbf{F}, \tag{2.43}$$

where the $M \times M$ DFT matrix $\mathbf{F}$ is a matrix whose (k, m)th element is given as

$$[\mathbf{F}]_{k,m} = \frac{1}{\sqrt{M}} e^{-j2\pi km/M}, \tag{2.44}$$

and $\mathbf{\Gamma}$ is the diagonal matrix

$$\mathbf{\Gamma} = \begin{bmatrix} H_0 & 0 & \dots & 0 \\ 0 & H_1 & \dots & 0 \\ \vdots & \vdots & \ddots & \vdots \\ 0 & 0 & \dots & H_{M-1} \end{bmatrix}. \tag{2.45}$$

The quantity H_l is the lth DFT coefficient of $h[n]$:

$$H_l = \sum_{n=0}^{M-1} h[n] e^{-j2\pi nl/M}. \tag{2.46}$$

Figure 2.16 shows the block diagram of a system, known as OFDM, that takes advantage of the circular channel matrix as given in (2.43). In this system, the information sequence $\tilde{s}[n]$ is first demultiplexed into $M-1$ streams such that the lth stream is given as $\tilde{s}_l[n] = \tilde{s}[nM+l]$. A block of symbols at time n is given an $\tilde{\mathbf{s}}[n] = [\tilde{s}_0[n], \tilde{s}_1[n], \cdots, \tilde{s}_{M-1}[n]]$. The vector $\tilde{\mathbf{s}}_n$ is processed (precoded) by $\mathbf{F}^H$ to produce $\mathbf{s}[n] = \mathbf{F}^H \tilde{\mathbf{s}}[n]$. Then, the CP system is applied to $\mathbf{s}[n]$. Substituting $\mathbf{s}[n] = \mathbf{F}^H \tilde{\mathbf{s}}[n]$ and $\mathbf{H}_{\text{circ}} = \mathbf{F}^H \mathbf{\Gamma} \mathbf{F}$ into (2.42) the nth received signal vector is expressed as

$$\begin{aligned} \mathbf{r}[n] &= (\mathbf{F}^H \mathbf{\Gamma} \mathbf{F}) \mathbf{F}^H \tilde{\mathbf{s}}[n] + \hat{\mathbf{w}}[n] \\ &= \mathbf{F}^H \mathbf{\Gamma} \tilde{\mathbf{s}}[n] + \hat{\mathbf{w}}[n]. \end{aligned} \tag{2.47}$$

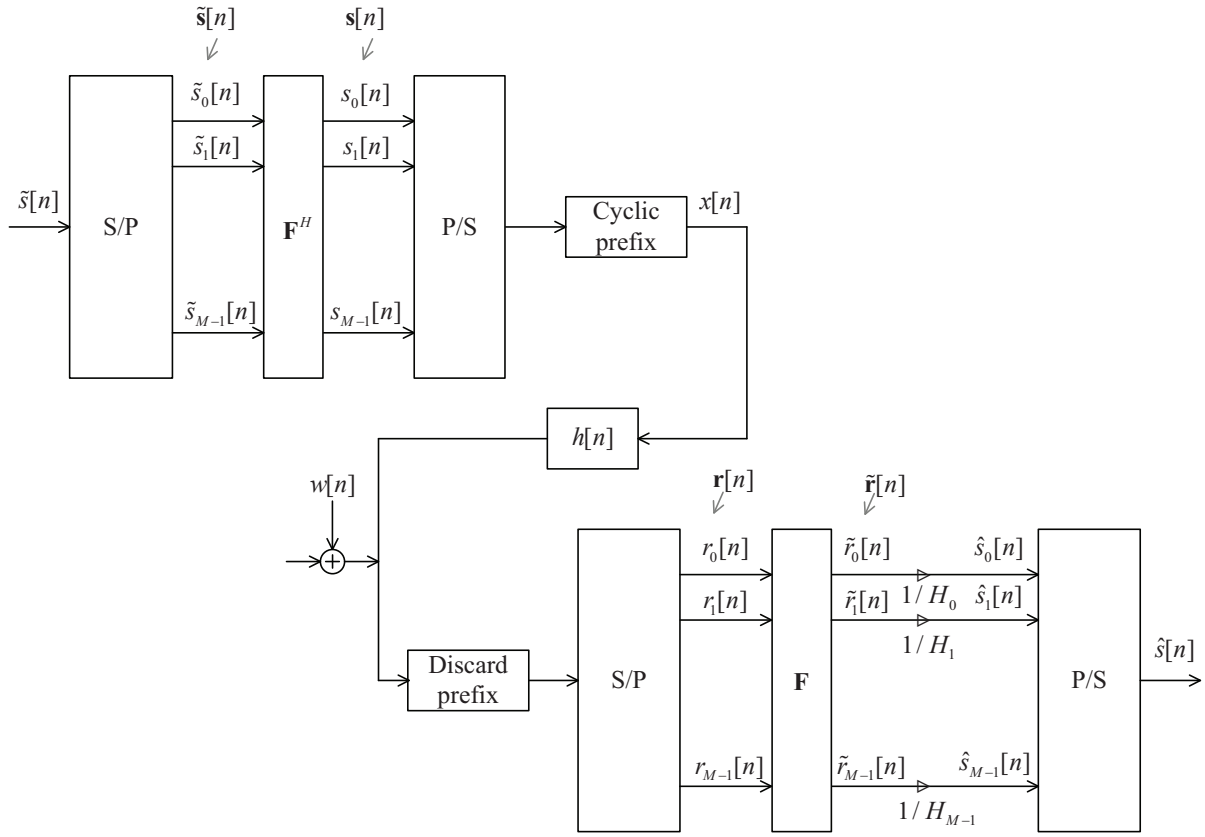

Figure 2.16: Discrete-time OFDM system.

At the receiver, be performing the DFT on $\mathbf{r}[n]$, one has

$$\begin{aligned}\tilde{\mathbf{r}}[n] &= \mathbf{F}\mathbf{r}[n] = \mathbf{F}(\mathbf{F}^H\mathbf{\Gamma}\tilde{\mathbf{s}}[n]) + \mathbf{F}\hat{\mathbf{w}}[n] \\ &= \mathbf{\Gamma}\tilde{\mathbf{s}}[n] + \tilde{\mathbf{w}}[n],\end{aligned} \tag{2.48}$$

where $\tilde{\mathbf{w}}[n] = \mathbf{\Gamma}\hat{\mathbf{w}}[n]$. Since $\mathbf{\Gamma}$ is a diagonalized matrix with elements H_l as expressed in (2.46), (2.48) can be rewritten as

$$\tilde{r}_l[n] = H_l\tilde{s}_l[n] + \tilde{w}_l[n], \quad l = 0, 1, \cdots, M-1. \tag{2.49}$$

Equation (2.49) demonstrates that an OFDM system effectively converts an ISI channel into M parallel subchannels as illustrated in Figure 2.17. The scalar H_l is the lth subchannel gain. Since there is no inter-subchannel interference, equalization can be easily done by multiplying $\tilde{r}_l[n]$ with $1/H_l$, an operation known as frequency domain equalization (FEQ).

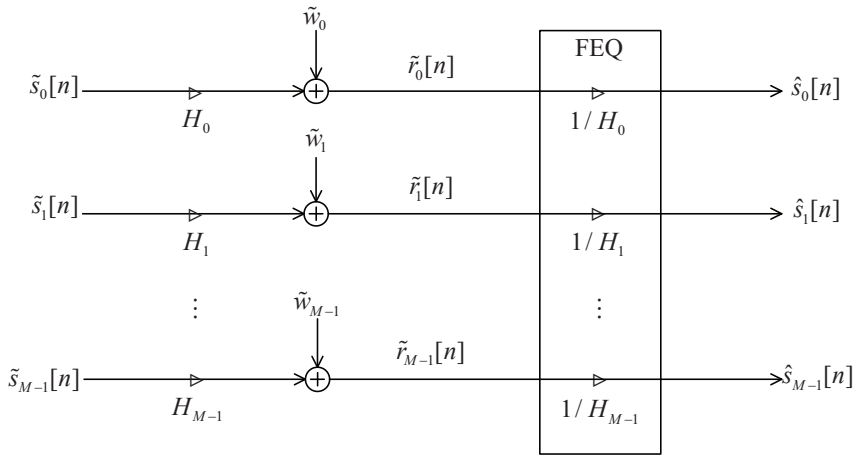

Figure 2.17: Equivalent parallel-subchannel model for the OFDM system.

Recall that $\hat{\mathbf{w}}[n]$ contains M i.i.d $\mathcal{CN}(0, N_0)$ random variables. Thus the autocorrelation matrix of $\hat{\mathbf{w}}[i]$ is $N_0\mathbf{I}_M$. The noise vector $\tilde{\mathbf{w}}_i = \mathbf{F}\hat{\mathbf{w}}[i]$ at the output of the DFT has autocorrelation $(N_0\mathbf{I}_M)\mathbf{F}\mathbf{F}^H = N_0\mathbf{I}_M$. That is, the DFT operation does not change the statistic of the noise. It follows that the SNR associated with the input/output model for the lth subchannel in (2.49) is

$$\beta_{\text{ofdm}}(l) = \frac{E_s|H_l|^2}{N_0} = \gamma_s|H_l|^2, \quad \text{where} \quad \gamma_s = E_s/N_0. \tag{2.50}$$

Since the subchannel SNR $\beta_{\text{ofdm}}(l)$ depends on the channel response, for frequency selective channels, $\beta_{\text{ofdm}}(l)$ can vary significantly with respect to l.

The average bit error rate of an OFDM system can be obtained by averaging the subchannel error rates. For M-QAM constellation with Gray mapping, the bit error rate of the lth channel follows directly from (2.33)

$$P_{b,\text{ofdm}}(l) = \frac{4}{\log_2(M)}\left(1 - \frac{1}{\sqrt{M}}\right) Q\left(\sqrt{\frac{3\gamma_b \log_2(M)|H_l|^2}{(M-1)}}\right), \tag{2.51}$$

The average BER of the OFDM system, averaged over all M subchannels is given as

$$P_{b,\text{ofdm}} = \frac{4}{M\log_2(M)}\left(1 - \frac{1}{\sqrt{M}}\right) \sum_{l=0}^{M-1} Q\left(\sqrt{\frac{3\gamma_b \log_2(M)|H_l|^2}{(M-1)}}\right). \tag{2.52}$$

As demonstrated, CP plays an important role in an OFDM system. However, CP leads to bandwidth inefficiency. Transmitting an information block of length M requires a block of length $M + L$, which results in a reduced bandwidth efficiency of $\eta = M/(M + L)$. In a frequency selective channel with a large number of taps, L should be long enough to combat IBI leading to small η. One could increase M such that $M \gg L$ to have an expected η. However, large M increases the delay of the system as well as the implementation complexity. Therefore, CP length needs to be carefully chosen when operating CP-OFDM in frequency selective channels, especially in cellular communication channels where bandwidth is a valuable resource.

Another drawback of OFDM system is inefficiency in using bandwidth since guard bands need to be allocated to prevent interference between communication system (which use OFDM transmission) operating in adjacent bands. This is due to the high side lobes of the spectrum of the transmitted signal. This is shown in the following.

From Figure (2.16), the transmitted signal on each subcarrier can be expressed as

$$s_k[n] = \frac{1}{\sqrt{M}} \sum_{l=0}^{M-1} \tilde{s}_l[n] e^{j2\pi kl/M} \tag{2.53}$$

The signal sequence $x[n]$ (assume no CP is added for simplicity) after the P/S converter is

$$x[n] = \sum_{k=0}^{M-1} \left[s_k[n-k] \right]_{\uparrow M}, \tag{2.54}$$

where $[\bullet]_{\uparrow M}$ denotes the upsampling by M samples of the sequence inside the bracket [26]. From (2.53), (2.54), the z transform of $x[n]$ is given as

$$\begin{aligned} X(z) &= \sum_{k=0}^{M-1} S_k(z^M) z^{-k} \\ &= \sum_{k=0}^{M-1} \frac{1}{\sqrt{M}} \sum_{m=0}^{M-1} S_l(z^M) e^{j2\pi kl/M} z^{-k} \\ &= \frac{1}{\sqrt{M}} \sum_{l=0}^{M-1} S_l(z^M) \sum_{k=0}^{M-1} \left(z e^{j2\pi l/M} \right)^{-k} \\ &= \frac{1}{\sqrt{M}} \sum_{l=0}^{M-1} S_l(z^M) F_l(z), \end{aligned} \tag{2.55}$$

where

$$\begin{aligned} F_l(z) &= F_0(ze^{j2\pi l/M}) \\ F_0(z) &= 1 + z^{-1} + \ldots + z^{-(M-1)} \end{aligned} \tag{2.56}$$

Equation (2.55) shows that the frequency spectrum of the lth subcarrier signal is compressed by M and then passes through the filter $F_l(z)$. In addition, (2.56) implies $f_0[n]$ is a rectangular window and $|F_0(e^{j\omega})| = |\sin(M\omega/2)/\sin(\omega/2)|$, which is plotted in Figure 2.18. The filter $F_l[z]$ has response

$$F_l(e^{j\omega}) = F_0(e^{j(\omega-(2\pi l/M))}) \tag{2.57}$$

which is a shifted version of $F_0(e^{j\omega})$. Thus, one can conclude that the transmitted OFDM signal can be synthesized from a bank of M filters as illustrated in Figure 2.19. The M filters are obtained from a single filter $F_0(z)$ by uniformly shifting the response. The stop-band attenuation of $F_0(z)$ is around 13 dB and its stop-band decays slowly with frequency.

To address the high stop-band attenuation, one could design $F_0(z)$ that has a sharper cutoff and higher stopband attenuation. However, in that case $f_0[n]$ is no longer an rectangular window and the CP length of the OFDM system should add to the length of $f_0[n]$ to guarantee no IBI [24]. Longer length of CP reduces the spectrum efficiency and should be avoided. Alternate multicarrier systems that do not require CP to achieve free IBI, and then can use well localized prototype filters have been studied. One of them is FBMC-OQAM, which is the topic of the next session.

Although, OFDM system is presented in this section in the discrete time domain, it is beneficial to represent it in the continuous time domain to compare with the SC-QAM system discussed in the previous section and the FBMC-OQAM system presented later. Figure 2.20 shows an OFDM system with M subcarriers in the continuous time domain where $p_R(t)$ is a rectangular window with duration T. In an ideal channel, $p_T(t)$ is also a rectangular window with duration T. Whereas, in a frequency selective channel, the duration of $p_T(t)$ is extended by a guard interval greater than the duration of the channel impulse response. This is illustrated in Figure 2.21. It is noticed that each subcarrier signal processing chain of an OFDM system is a SC-QAM system. Especially, each subcarrier signal is modulated in frequency by $e^{j2\pi(f_c+k/T)}$, where $k = 0, \cdots, M-1$ and the frequency spacing

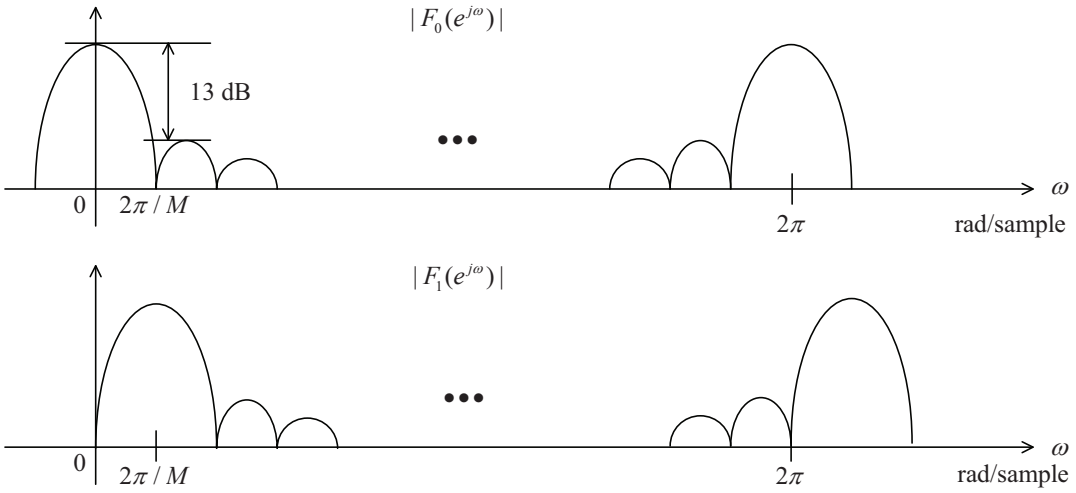

Figure 2.18: Frequency response of a rectangular pulse and its shifted version.

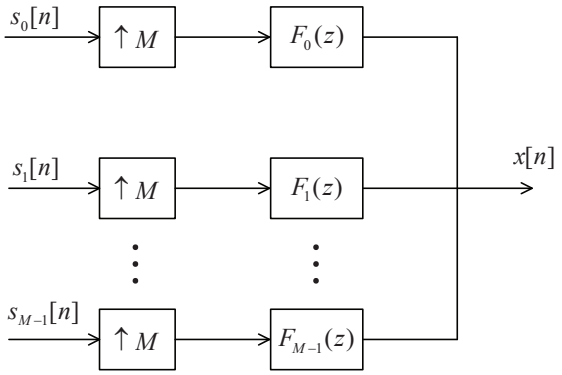

Figure 2.19: The OFDM transmitted signal synthesized from a bank of M filters.

is $F = 1/T$. Then, one can draw a time-frequency phase-space lattice representation of an OFDM system as in Figure 2.22. From the figure, there is one symbol in each rectangular of area $(T + T_{\text{cp}}) \times F = (T + T_{\text{cp}})/T$. Thus, the data symbol density is

$$\frac{1}{(T + T_{\text{cp}})F} = \frac{T}{T + T_{\text{cp}}} \leq 1. \tag{2.58}$$

The data symbol density also characterizes the bandwidth efficiency of OFDM. It is seen that OFDM achieves the upper limit 1 in (3.9) only in an ideal channel.

In summary, OFDM is an multicarrier system that uses CP and rectangular window to achieve orthogonality. It has an efficient implementation structure based on DFT and IDFT, and simple equalization. However, due to the use of rectangular window which has high side

lobes in the frequency domain, the power of the transmitted OFDM signal in the out-of-band frequency region could be high that causes interference to the transmitted signals of other communication system operating in adjacent bands. Furthermore, the use of CP leads to a loss of bandwidth efficiency.

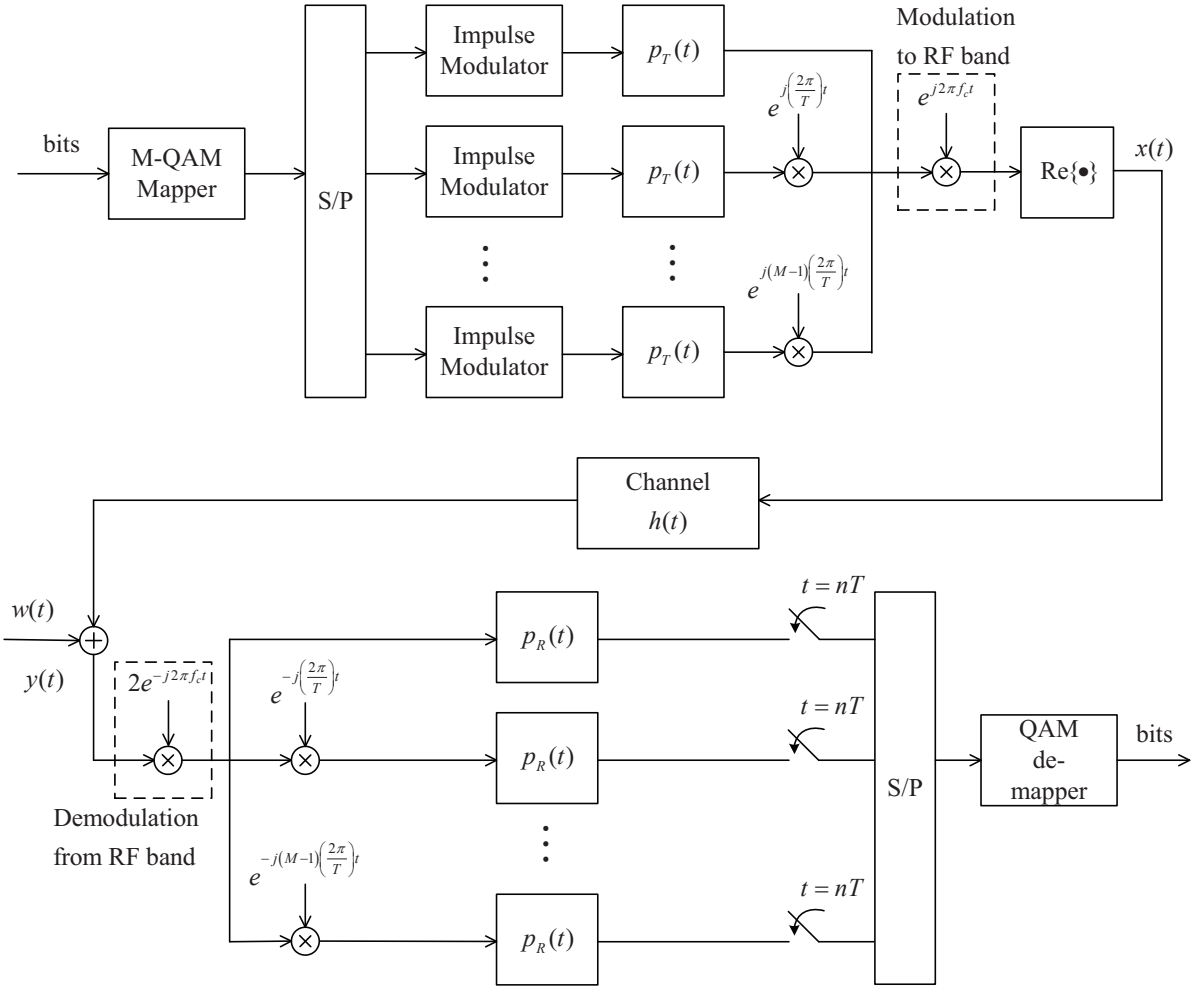

Figure 2.20: Representation of an OFDM system in the continuous time domain.

2.3 FBMC-OQAM System

In this section, an alternative multicarrier system, called Filter Bank Multicarrier Offset QAM (FBMC-OQAM), is presented. It will be shown that in an ideal channel, the transmitted symbols of FBMC system can be perfectly recovered without ISI or intercar-

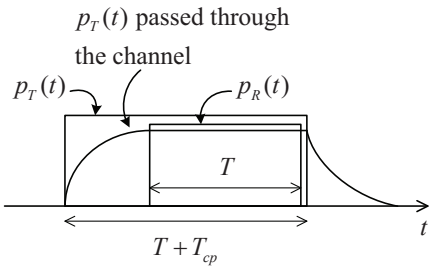

Figure 2.21: An illustration of how orthogonality is established in OFDM.

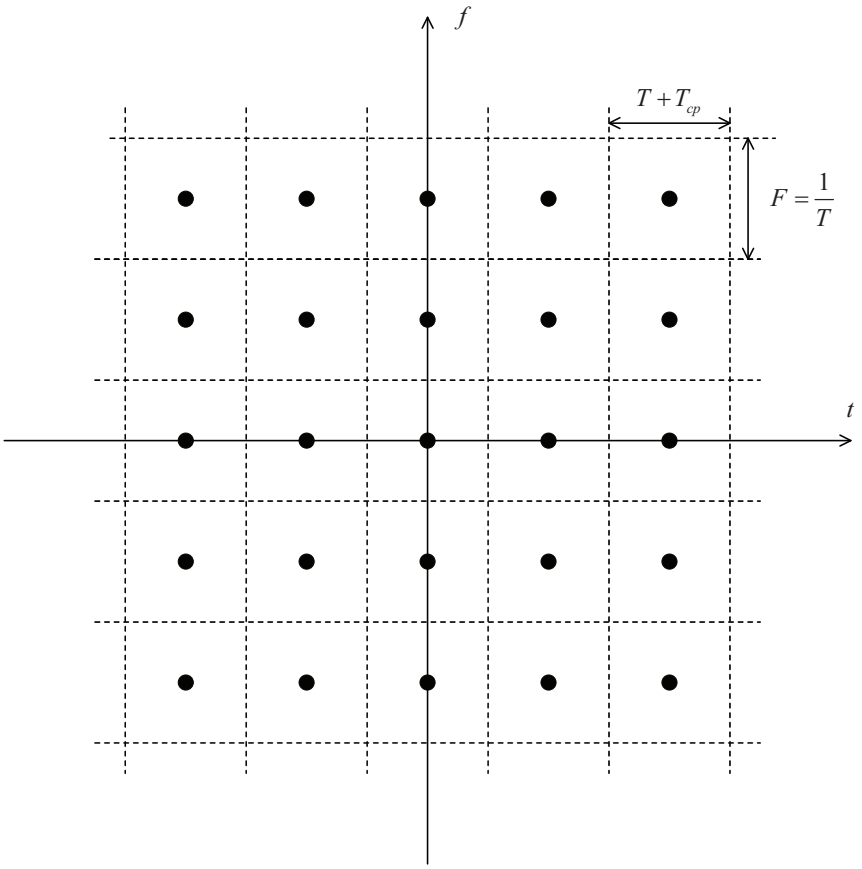

Figure 2.22: Time-frequency phase-space lattice representation of an OFDM system.

rier interference (ICI). In addition, the bandwidth efficiency of FBMC system is 1, which is the same as in OFDM for an ideal channel. The most important feature that distinguishes FBMC from OFDM is that, well-localized prototype filters can be used in an FBMC system without sacrificing the perfect reconstruction or bandwidth efficiency.

The presentation of FBMC-OQAM in this section follows closely the framework of [27],

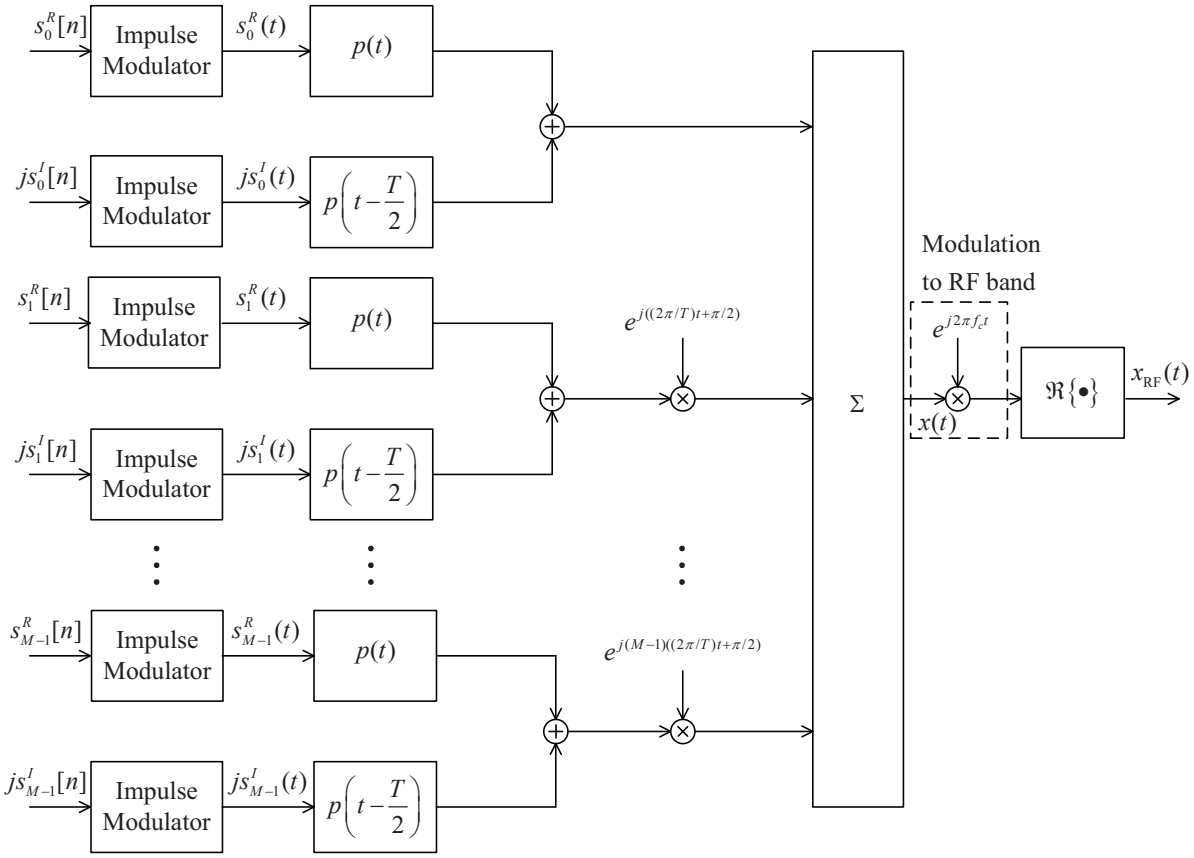

Figure 2.23: Block diagram of an FBMC-OQAM transmitter.

[12]. First, the transceiver structure is described. Then, how the system achieves the perfect reconstruction is explained. The bandwidth efficiency and the power spectrum density of FBMC-OQAM are also discussed.

An FBMC-OQAM system is illustrated in Figures 2.23 and 2.24 [12]. It should be noted that the same symmetric prototype filter $p(t)$ is used at the transmitter and the receiver. At the transmitter, each QAM symbol is divided into its real and imaginary part as

$$s_m(t) = s_m^R(t) + js_m^I(t) = \sum_{n=-\infty}^{+\infty} (s_m^R[n] + js_m^I[n])\delta(t - nT). \tag{2.59}$$

Then the real and imaginary parts on each subcarrier are staggered by $T/2$. This is done through the pulse shaped filter $p(t)$ which is shifted in time. In addition, a phase shift of $\pi/2$ is applied between any pair of adjacent symbols (along both the time and frequency axes).

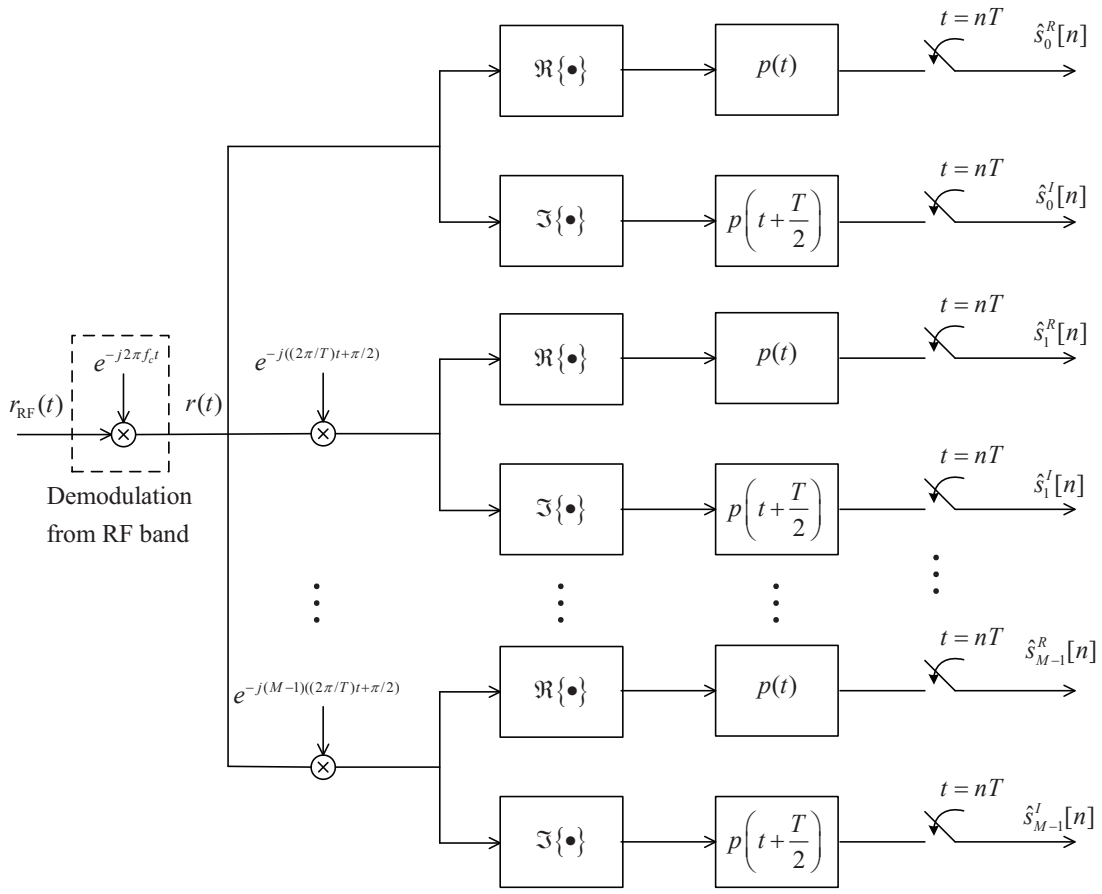

Figure 2.24: Block diagram of an FBMC-OQAM receiver.

The baseband transmitted signal in Figure 2.23 is given as

$$\begin{aligned} x(t) &= \sum_{m=0}^{M-1} \left[s_m^R(t) * p(t)\right] e^{jm\left(\frac{2\pi t}{T}+\frac{\pi}{2}\right)} + \sum_{m=0}^{M-1} \left[j s_m^I(t) * p\left(t-\frac{T}{2}\right)\right] e^{jm\left(\frac{2\pi t}{T}+\frac{\pi}{2}\right)} \\ &= \sum_{m=0}^{M-1} \sum_{n=-\infty}^{+\infty} \left[s_m^R[n] p\left(t-nT\right) e^{jm\frac{2\pi t}{T}} e^{jm\frac{\pi}{2}} + j s_m^I[n] p\left(t-\frac{T}{2}-nT\right) e^{jm\frac{2\pi t}{T}} e^{jm\frac{\pi}{2}}\right] \end{aligned} \tag{2.60}$$

Define

$$s_m[n] = \begin{cases} s_m^R[n'] & \text{for } n = 2n' \\ s_m^I[n'] & \text{for } n' = 2n'+1 \end{cases} \tag{2.61}$$

Then, Equation (2.60) can be rewritten as

$$x(t) = \sum_{m=0}^{M-1} \sum_{n=-\infty}^{+\infty} s_m[n] p\left(t-n\frac{T}{2}\right) e^{jm\frac{2\pi t}{T}} e^{j(m+n)\frac{\pi}{2}}. \tag{2.62}$$

Equation (2.62) implies that the real and imaginary parts of the original QAM symbols are transmitted with a time offset of $T/2$, and the data symbols are spaced at $F = 1/T$ along the

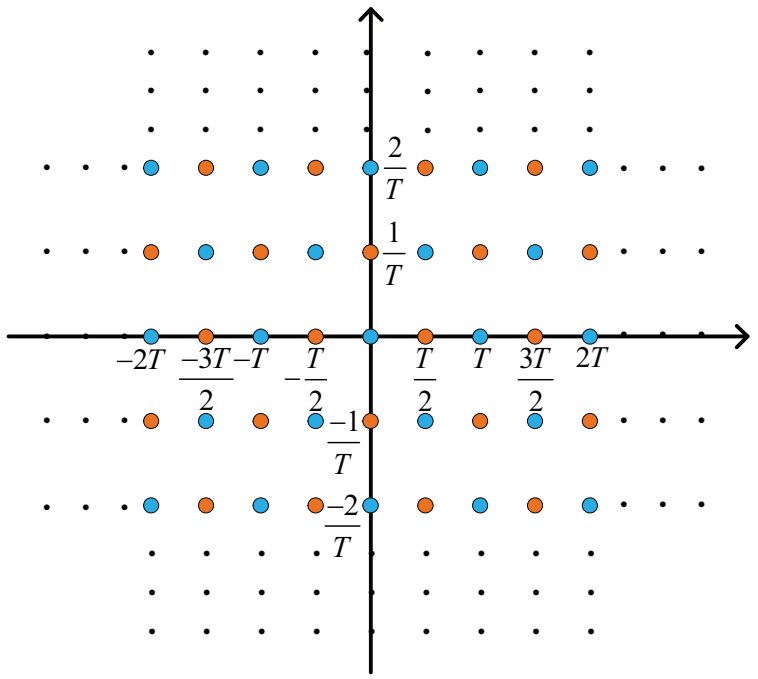

Figure 2.25: Time frequency phase space for transmission of FBMC-OQAM system.

frequency axis. In addition, the term $e^{j(m+n)\frac{\pi}{2}}$ indicates the phase offset of $\pi/2$ between any pair of adjacent symbols along the time and frequency axes as illustrated in time-frequency phase-space lattice representation in Figure 2.25, where the blue dots denote phase shift of integer factor of π and the orange dots denote phase shift of odd factor of $\pi/2$. It is obvious from the figure that there is one symbol over an area of $T/2 \times F = 1/2$, which results in the density symbol of two. However, notice that the symbol in Figure 2.25 is a real symbol ($s_m^R[n]$ or $s_m^I[n]$) and it carries one half of the information bits of the original complex QAM symbol ($s_m[n]$). Thus, one can conclude that FBMC-OQAM achieves the bandwidth efficiency of one, the same as OFDM system illustrated in Figure 2.22.

Figure 2.24 depicts the receiver of an FBMC-OQAM system. The detected data symbols at the receiver output are denoted as $\hat{s}_m^R[n]$ (or $\hat{s}_m^I[n]$). The filter $p(t)$ should be designed to have perfect reconstruction, i.e., $\hat{s}_m^R[n] = s_m^R[n]$ when the channel is ideal (there is no multipath fading and noise). The condition of $p(t)$ for such a perfect recovery is discussed next.

First, in an FBMC-OQAM system, the prototype filter is designed with an assumption

that $p(t)$ is band-limited such that only adjacent subcarrier channels overlap [28]. Thus, one can ignore possible interference from non-adjacent bands. In that case, there are only three interference scenarios that may happen:

1. The ISI on each subcarrier, that is, $s_m^R[n]$ interferences with $s_m^R[n']$ for $n \neq n'$, and similarly for $s_m^I[n]$.

2. The cross interference between $s_m^R[n]$ and $s_m^I[n]$.

3. ICI among the adjacent subcarrier signals.

To investigate the first and second scenarios, consider the relevant branches from Figure 2.23 and 2.24 that connect $s_m^R[n]$ and $js_m^I[n]$ to $\hat{s}_m^R[n]$ and $\hat{s}_m^I[n]$. In an ideal channel, these branches are illustrated in Figure 2.26. It is noted that the subcarrier modulator $e^{jm\left(\frac{2\pi t}{T}+\frac{\pi}{2}\right)}$ and the demodulator $e^{-jm\left(\frac{2\pi t}{T}+\frac{\pi}{2}\right)}$ cancel each other. Also noted that the output of $p(t)$ at the transmitter of Figure 2.26a is an real function of time since $s_m^R(t)$ is real symbol and $p(t)$ has real coefficients. In contrast, the output of $p(t-T/2)$ on the bottom-left of Figure 2.26a is an imaginary function of time. Thus, one can separate the blocks in Figure 2.26a in two separate channels as in Figure 2.26b.

From Figure 2.26b, it is obvious that there is no cross interference between the real and imaginary part of each subcarrier channel in FBMC-OQAM. To eliminate ISI , it is necessary and sufficient that $p(t)$ is chosen such that the combined response $p(t)*p(t)$ satisfies Nyquist criterion [27]. This requirement also guarantees ISI free transmission in the lower branch in Figure 2.26b, since $p(t-T/2)*p(t+T/2) = p(t)*p(t)$.

Figure 2.27 presents the branches that illustrate the interference from the $(m+1)$th subcarrier to the detection of symbols on the mth subcarrier. To show that there is no ICI between adjacent carriers, one need to show that $\tilde{s}_m^R[n] = 0$, and $\tilde{s}_m^I[n] = 0$ for all n. Consider the proof for $\tilde{s}_m^R[n] = 0$. Denote the output of the block labelled with $p(t)$ at the receiver in Figure 2.27 as $z(t)$. One has

$$\begin{aligned} z(t) &= \mathcal{R}\left\{ \left(s_{m+1}^R(t)p(t) + js_{m+1}^I(t)p\left(t-\frac{T}{2}\right)\right) e^{j(\frac{2\pi}{T}t+\frac{\pi}{2})} \right\} * p(t) \\ &= s_{m+1}^R(t)z_1(t) + s_{m+1}^I(t)z_2(t), \end{aligned} \tag{2.63}$$

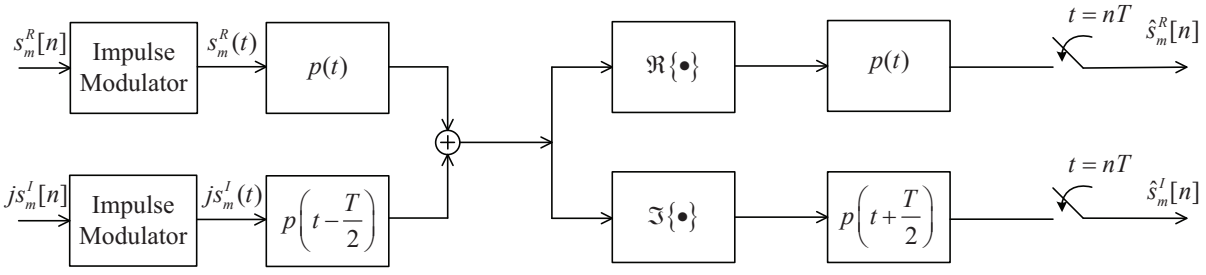

(a)

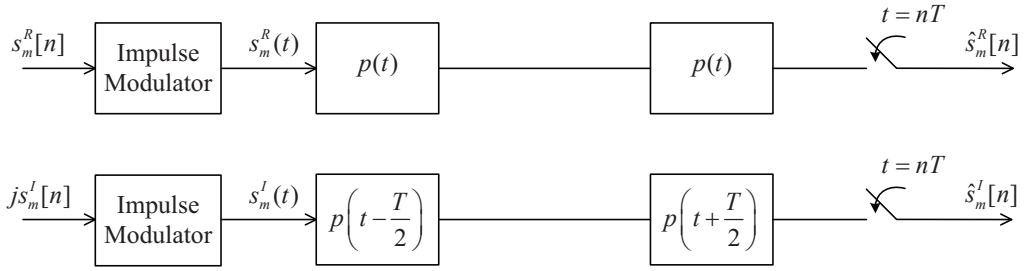

(b)

Figure 2.26: The mth subcarrier channel in an FBMC-OQAM system.

where

$$\begin{aligned} z_1(t) &= \mathcal{R}\left\{p(t)e^{j(\frac{2\pi}{T}t+\frac{\pi}{2})}\right\} * p(t) \\ z_2(t) &= \mathcal{R}\left\{p\left(t-\frac{T}{2}\right)e^{j(\frac{2\pi}{T}t+\pi)}\right\} * p(t). \end{aligned} \tag{2.64}$$

The interference term $\tilde{s}_m^R[n]$ is obtained by sampling $z(t)$ at $t = nT$ and given as

$$\tilde{s}_m^R[n] = s_{m+1}^R[n]z_1(nT) + s_{m+1}^I[n]z_2(nT) \tag{2.65}$$

The response $z_1(t)$ can be rewritten as

$$\begin{aligned} z_1(t) &= p(t)\cos\left(\frac{2\pi}{T}t+\frac{\pi}{2}\right) * p(t) \\ &= \int_{-\infty}^{\infty} p(\tau)\cos\left(\frac{2\pi}{T}\tau+\frac{\pi}{2}\right) * p(t-\tau)d\tau \\ &= -\int_{-\infty}^{\infty} p(\tau)\sin\left(\frac{2\pi}{T}\tau\right) * p(t-\tau)d\tau. \end{aligned} \tag{2.66}$$

Let $\tau = \tau + \frac{nT}{2}$, one obtain

$$\begin{aligned} z_1(nT) &= (-1)^{n+1}\int_{-\infty}^{\infty} p\left(\tau+\frac{nT}{2}\right)p\left(-\tau+\frac{nT}{2}\right)\sin\left(\frac{2\pi}{T}\tau\right)d\tau. \\ &= 0 \end{aligned} \tag{2.67}$$

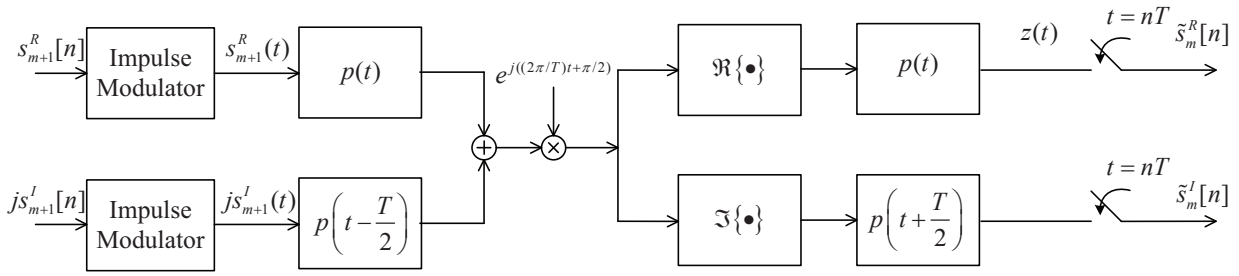

Figure 2.27: The interference branch from subcarrier $(m+1)$ to subcarrier m.

since $p\left(\tau+\frac{nT}{2}\right)p(-\tau+\frac{nT}{2})$ is an even function whereas $\sin\left(\frac{2\pi}{T}\tau\right)$ is an odd function, and then the expression under the integral of (2.67) is an odd function. Similarly, one can prove that $z_2(nT)=0$ for all n and then conclude that $\tilde{s}^R_m[n]=0$ for all n. The same is true for $\tilde{s}^I_m[n]$. Thus, there is no ICI between adjacent subcarriers in a FBMC-OQAM system.

In summary, the key designs that enable the FBMC-OQAM system to be an orthogonal system are:

(i) Using offset QAM modulation (OQAM) with a time shift of $T/2$ between the real part and imaginary part of a complex symbol and a subcarrier spacing of $F=1/T$.

(ii) Using the same prototype filter at the transmitter and the receiver, i.e., $p_T(t)=p_R(t)=p(t)$ such that $p(t)*p(t)$ satisfies the Nyquist criterion.

It has been discussed in the previous section that to satisfy (ii), $p(t)$ should be an SRRC filter which has the impulse response and frequency response as given in (2.23) and (2.22), respectively. One might ask how to choose the roll-off factor of the SRRC filter. It is pointed out that the larger the roll-off factor is, the more excess bandwidth is, but the faster the impulse response decays. The excess bandwidth causes ICI but in FBMC-OQAM the ICI between adjacent bands is eliminated by using OQAM. Thus, one can maximize the rate of decaying by choosing roll-off factor $\beta=1$ without worrying about ICI. This choice allows the ideal SRRC filter to be well approximated with a relatively short filter, and still can achieve a very high attenuation in the stopband. Figure 2.28 illustrates the magnitude responses of the prototype filters and the estimated PSDs of OFDM and FBMC-OQAM systems. The estimation is based on computing the FFT of 1000 blocks of the transmitted signal. We

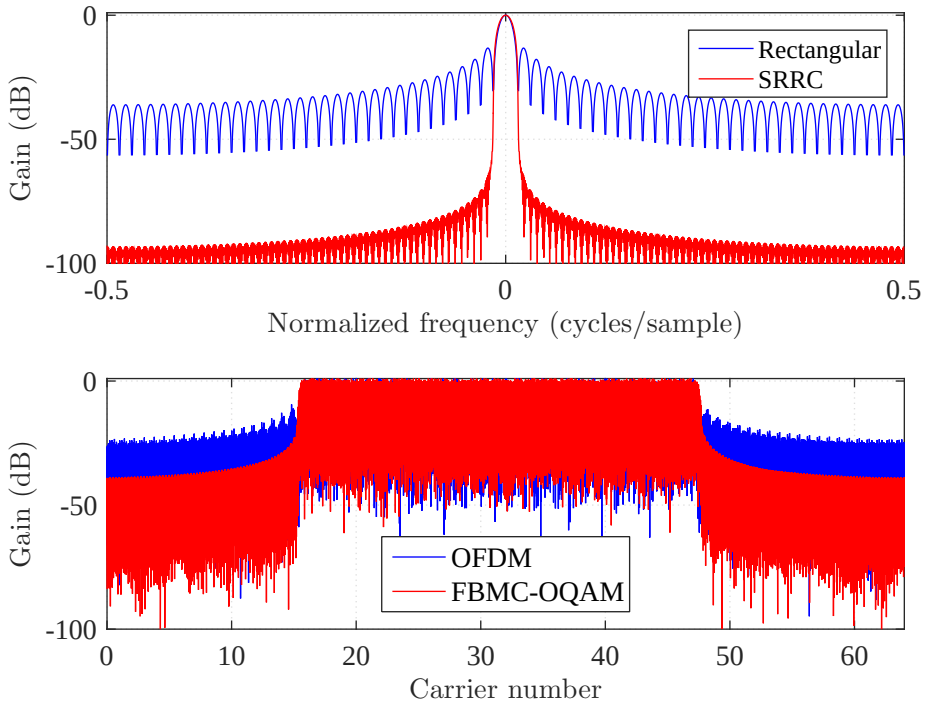

Figure 2.28: Mangitude responses of the prototype filters and the estimated PSDs of OFDM and FBMC-OQAM. $M = 64$ subcarriers, 32 active subcarriers which are $[17 : 48]$, SRRC filter with roll-off factor $\beta = 1$ for FBMC-OQAM.

observe that the magnitude response of the rectangular filter has higher side lobes than that of the SRRC filter. As a consequence, the power of FBMC-OQAM in the out-of-band (OOB) region (carriers $[0 : 16]$ and $[49 : 64]$) is lower than that of FBMC-OQAM.

The presentation and discussion of FBMC-OQAM in this section were based on the assumption that the channel is ideal. It is noted that the main reason for using any multicarrier system is to deal with ISI inherent in frequency-selective channels. An OFDM system utilizes CP to completely remove ISI. CP also enables simple equalization of OFDM signals, which requires only one-tap equalizer per subchannel. Unfortunately, due to the absence of CP, FBMC-OQAM requires complex equalization where one-tap per subchannel is not suffcicient to cope with frequency selective channels [12]. Knowing the benefit of CP while paying attention to its adverse effect (loss of bandwidth efficiency), one should find a way to exploit its advantages while limiting its disadvantages. Recently, a modified version of FBMC-OQAM, called circular FBMC-OQAM (CFBMC-OQAM) has been proposed. A

CFBMC-OQAM system not only benefits from all good properties of FBMC-OQAM system but also has the simple equalization like OFDM system due to the use of CP. Details of this scheme will be presented in the next chapter.

3. GFDM and CFBMC-OQAM

Although being widely adopted for current generation of wireless networks, OFDM has several drawbacks that make it less attractive for the next generation networks. First, OFDM requires one CP per symbol, which leads to low spectral efficiency. Second, the power spectrum of OFDM signals poses challenges for opportunistic and dynamic spectrum access. For those reasons, alternative multicarrier schemes are being investigated as candidates for the physical layer of next-generation mobile communication systems.

Generalized Frequency Division Multiplexing (GFDM) and Circular Filter Bank Multicarrier Offset OQAM (CFBMC-OQAM) are new multicarrier schemes that have recently been proposed for 5G networks [13]. The two techniques are based on the approach of replacing linear convolution for pulse shaping filtering with circular convolution. By using circular filtering, the overall system can maintain block transform processing so that a CP can be easily inserted. In fact, the use of circular convolution was originally proposed for GFDM systems to reduce the guard time interval between GFDM blocks. Details of the circular convolution technique will be presented later in this chapter. Due to its advantages, [15] adopts the circular filtering technique for the classical FBMC-OQAM system, which results in CFBMC-OQAM. CFBMC-OQAM is distinguishably different from GFDM by the fact that it is an orthogonal system, whereas GFDM is not. A non-orthogonal system is not preferred because it might require a complex and expensive receiver to cancel the interference caused by loosing the orthogonality. CFBMC-OQAM maintains its orthogonality by using offset QAM modulation (presented in the previous chapter), and requiring the combined response of transmit and receive filters be a Nyquist pulse. In contrast, GFDM has a flexibility in choosing the modulation symbols and the pulse shaping filter, but the system is

non-orthogonal and requires an advanced receiver to cancel ISI and intercarrier interference (ICI).

3.1 Generalized Frequency Division Multiplex (GFDM)

GFDM is a block-based structure multicarrier scheme that transmits MK data symbols per block using M time slots and K subcarriers. In addition, each data symbol is modulated by a pulse shaping filter that is obtained from a prototype filter appropriately shifted in time and frequency. In doing so, GFDM can control the power spectrum density (PSD) of the transmitted signal by choosing an appropriate pulse shaping filter. In a GFDM system, the pulse shaping filter should be chosen such that it has a sharp edge in the frequency domain in order to limit the interference between adjacent subcarriers. However, the good localization in frequency domain leads to a longer duration in the time domain. This is an issue since the length of the filters should be included in the CP, which results in inefficiently long CP. This issue can be addressed by using tail biting technique [13]. Details of this technique and the description of the GFDM transmitter are presented next.

3.1.1 GFDM Transmitter

The block diagram of a GFDM transmitter is illustrated in Figure 3.1 . The sequence of input bits is divided into K data streams. Each QAM modulation maps a group of q bits into a data symbol $s_{k,m}$, $k = 0, 1, 2, \ldots, K-1$, and $m = 0, 1, 2, \ldots, M-1$. Therefore, each of the K subcarriers transmits M data symbols per GFDM block. The data symbols transmitted in one block can be represented in a matrix form as:

$$\mathbf{S} = \begin{bmatrix} s_{0,0} & s_{0,1} & \cdots & s_{0,M-1} \\ s_{1,0} & s_{1,1} & \cdots & s_{1,M-1} \\ \vdots & \vdots & \ddots & \vdots \\ s_{K-1,0} & s_{K-1,1} & \cdots & s_{K-1,M-1} \end{bmatrix}, \tag{3.1}$$

where the kth row represents the symbols transmitted on the kth subcarrier and the mth column represents the symbols transmitted on the mth time slot.

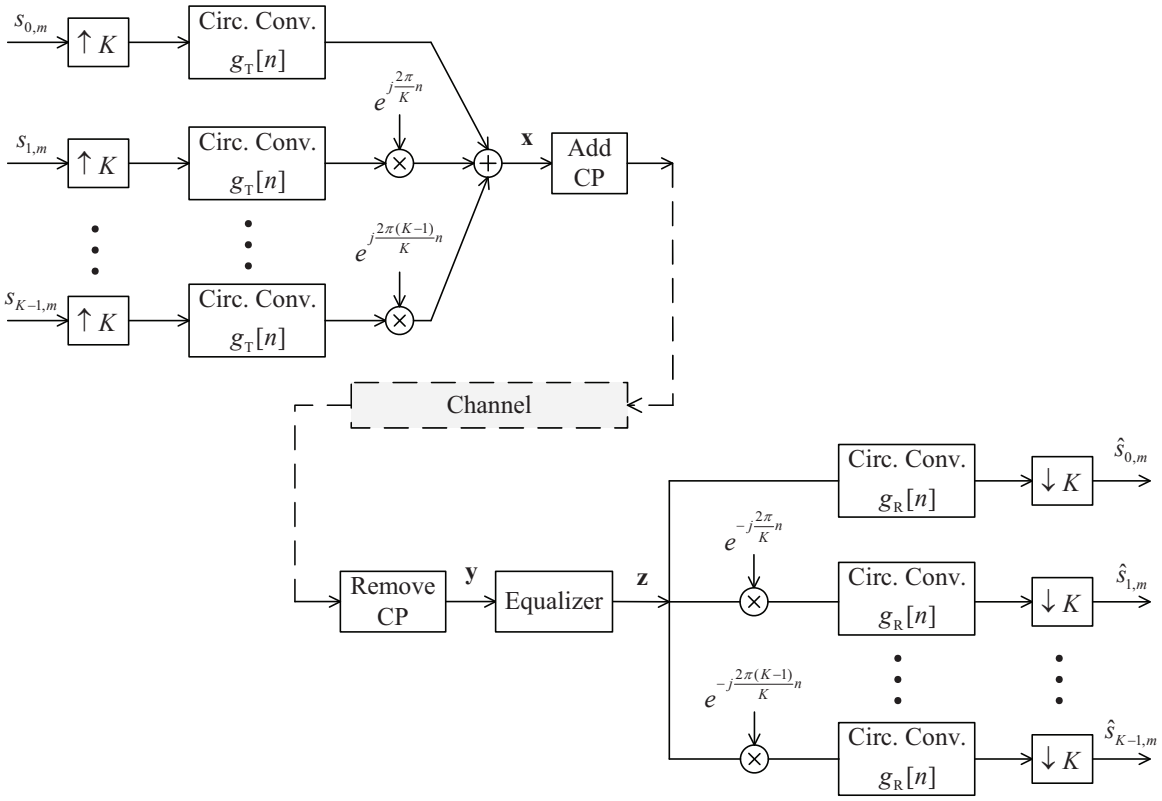

Figure 3.1: Block diagram of a GFDM transceiver.

The sequence of data symbols transmitted on the kth subcarrier can be expressed as

$$s_k[n] = \sum_{m=0}^{M-1} s_{k,m}\delta[n - mK], \tag{3.2}$$

Then, the sequence is shaped by a filter $g_{\mathrm{T}}[n]$ of length $N = MK$. If the filtering process is linear convolution as illustrated in Figure 3.2 for the case of $K = 8$, and $M = 3$, the guard time interval between GFDM blocks should be greater than the channel delay spread plus the filter length, which is equal to $(M - 1)K = 16$ samples in this example. A large guard time interval causes reduction in throughput and poor spectrum efficiency. To overcome such a drawback, a technique called tail biting is proposed in [13]. In this technique, the mK last samples at the output of the filter are shifted to the first mK position as illustrated in Figure 3.3 . This process is equivalent to a circular convolution between $s_{k,m}[n]$ and $g_{\mathrm{T}}[n]$. In order to use the tail biting technique, the filter impulse response is circularly shifted as shown in Figure 3.3 [13], [29]. Then each sub-stream is up-converted by multiplying with a complex subcarrier $e^{j2\pi\frac{k}{K}n}$.

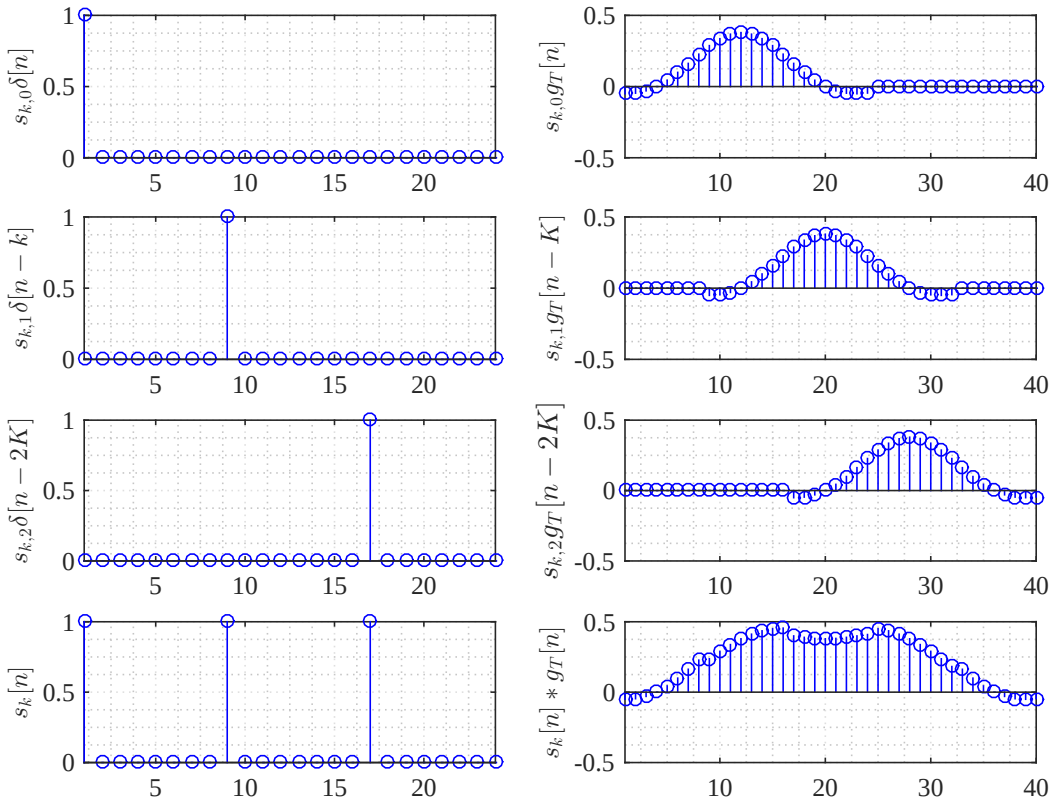

Figure 3.2: GFDM symbols obtained by linear convolution.

From Figure 3.1, the transmitted GFDM signal can be expressed as

$$\begin{aligned} x[n] &= \sum_{k=0}^{K-1} s_k[n] \circledast g_{\mathrm{T}}[n] e^{j2\pi \frac{k}{K} n} \\ &= \sum_{k=0}^{K-1} \sum_{m=0}^{M-1} s_{k,m}\delta[n-mK] \circledast g_{\mathrm{T}}[n] e^{j2\pi \frac{k}{K} n} \\ &= \sum_{k=0}^{K-1} \sum_{m=0}^{M-1} s_{k,m} g_{\mathrm{T}}[(n-mK)_N] e^{j2\pi \frac{k}{K} n} \\ &= \sum_{k=0}^{K-1} \sum_{m=0}^{M-1} s_{k,m} g_{k,m}[n], \quad n = 0, \ldots, N-1, \end{aligned} \tag{3.3}$$

where

$$g_{k,m}[n] = g_{\mathrm{T}}[(n-mK)_N] e^{j2\pi \frac{k}{K} n}. \tag{3.4}$$

Each $g_{k,m}[n]$ is a time and frequency shifted version of a prototype filter $g_{\mathrm{T}}[n]$, where the modulo operation makes $g_{k,m}[n]$ a circularly shifted version of $g_{\mathrm{T}}[n]$ with period N and the complex exponential performs the shifting operation in frequency. Equation (3.3) can be

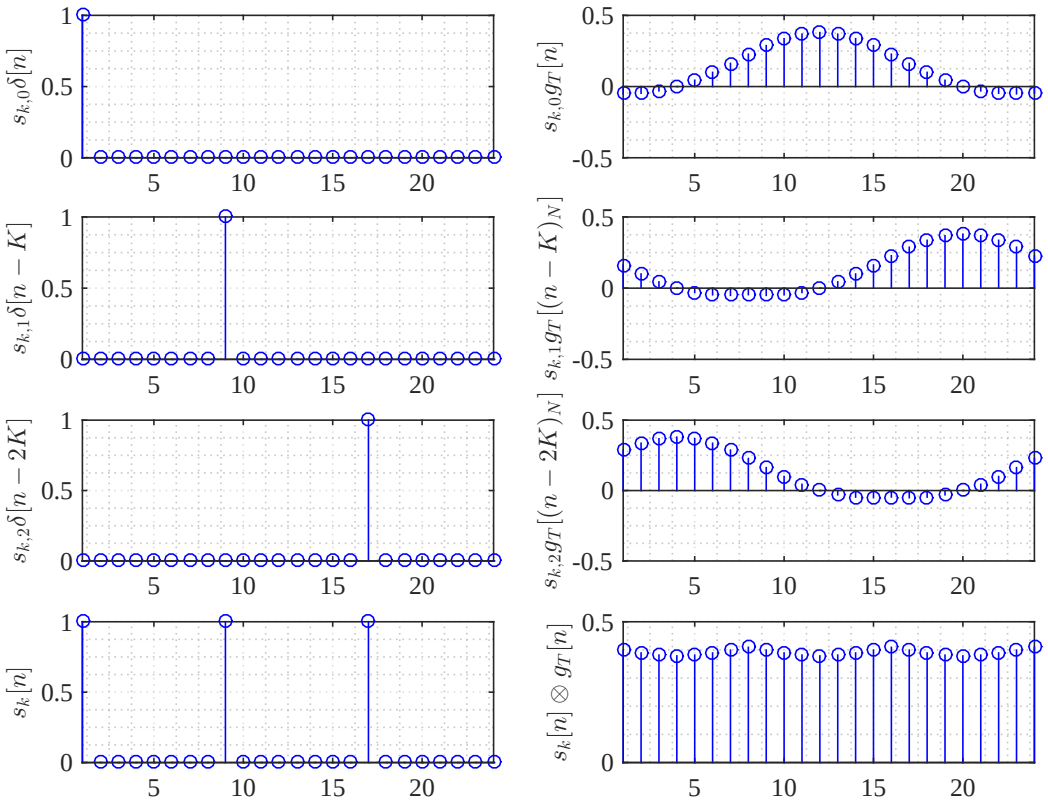

Figure 3.3: GFDM symbols obtained by circular convolution.

rewritten in a matrix form as:

$$\mathbf{x} = \mathbf{A}\mathbf{d}, \tag{3.5}$$

where $\mathbf{x} = [x[0], x[1], \ldots, x[N-1]]^{\mathrm{T}}$, $\mathbf{d} = [s_{0,0}, s_{1,0}, \ldots, s_{K-1,0}, s_{0,1}, s_{1,1}, \ldots, s_{K-1,M-1}]^{\mathrm{T}}$ and

$$\mathbf{A} = \begin{bmatrix} \mathbf{g}_{0,0} & \ldots & \mathbf{g}_{K-1,0} & \mathbf{g}_{0,1} & \ldots & \mathbf{g}_{K-1,M-1} \end{bmatrix} \tag{3.6}$$

with $\mathbf{g}_{k,m} = [g_{k,m}[0], g_{k,m}[1], \ldots, g_{k,m}[N-1]]^{\mathrm{T}}$.

From Equation (3.3) it is pointed out that each symbol $s_{k,m}$ of a GFDM block is transmitted by $g_{k,m}[n]$. The set of $g_{k,m}[n]$ for all k and m is not an orthogonal set leading to two kinds of interference. The intersymbol interference (ISI) between $s_{k,m}$ and $s_{k,m'}$ for $m \neq m'$, and the intercarrier interference (ICI) between $s_{k,m}$ and $s_{k',m}$ for $k \neq k'$. The impact of ISI and ICI on the performance of GFDM depends on which prototype filter is chosen to produce $g_{\mathrm{Tx}}[n]$. The Raised Cosine (RC) and Square Root Raised Cosine (SRRC) filters have been investigated as prototype filters for GFDM systems in [30]. The analysis show that if RC

filters are used on the transmitter and receiver sides, there will be larger ISI when compared with the use of SRRC filters because the Nyquist criterion is not satisfied. However the ICI will be smaller because of the shaper frequency response of the RC filters as compared to the SRRC filters. In addition, the smaller the roll-off factor of the prototype filter, the better the system performance (BER) because of the larger reduction of the ICI.

A block of GFDM symbols is represented by vector $\mathbf{x}$. Before transmission through a wireless channel that has an impulse response $h[v]$, $v = 0, 1, \ldots V-1$, $\mathbf{x}$ is appended with a CP of length L. After transmitting over the channel, the CP is removed at the receiver to eliminate the interblock interference (IBI). As discussed in the previous chapter, as long as $L \geq V - 1$ the relationship between the transmitted vector $\mathbf{x}$ and received vector $\mathbf{y}$ in Figure 3.1 is given as

$$\mathbf{y} = \mathbf{H}\mathbf{x} + \mathbf{w}, \tag{3.7}$$

where $\mathbf{H}$ is an $N \times N$ circulant matrix constructed from the channel vector

$$\mathbf{h} = [h[0], h[1], \ldots, h[V-1]]^{\mathrm{T}}, \tag{3.8}$$

and $\mathbf{w} \sim \mathcal{CN}(0, \mathcal{N}_0\mathbf{I}_N)$ denotes additive white Gaussian noise.

It should be noted that while OFDM requires a CP between two time slots, GFDM requires a CP only between GFDM blocks as illustrated in Figure 3.4. Since the CP is the same in both cases, GFDM achieves a higher spectrum efficiency compared to OFDM. Specifically, the spectrum efficiency of an OFDM system with K subcarriers and a CP of length N_{CP} is given as

$$\eta_{\mathrm{OFDM}} = \frac{K}{K + N_{CP}}. \tag{3.9}$$

On the other hand, the spectrum efficiency of an GFDM system with the same number of subcarriers and CP length is given as

$$\eta_{\mathrm{GFDM}} = \frac{KM}{KM + N_{CP}} \tag{3.10}$$

Thus, the spectral efficiency gain of GFDM over OFDM is

$$\rho = \frac{\eta_{\mathrm{GFDM}}}{\eta_{\mathrm{OFDM}}} = \frac{M(K + N_{CP})}{MK + N_{CP}}. \tag{3.11}$$

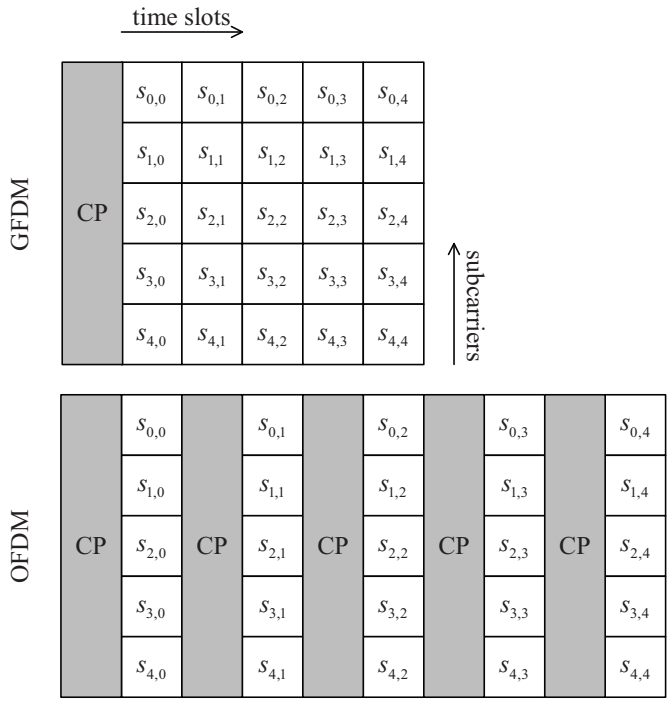

Figure 3.4: Block structures of OFDM and GFDM systems for $M = 5$ and $K = 4$.

For example, with $K = 64$, $M = 32$, and $N_{\mathrm{CP}} = 16$, the spectrum efficiency gain of GFDM over OFDM is $\rho = 1.25$, i.e., 25% increase.

3.1.2 GFDM Receiver

Since $\mathbf{H}$ in (3.7) is a circular convolution matrix, the received signal $\mathbf{y}$ can be equalized using the zero-forcing equalizer as efficiently used in OFDM. The equalized signal $\mathbf{z} = [z[0], z[1], \ldots, z[N-1]]^{\mathrm{T}}$ can be expressed as

$$\begin{aligned} \mathbf{z} &= \mathbf{H}^{-1}\mathbf{y} \\ &= \mathbf{H}^{-1}\mathbf{H}\mathbf{A}\mathbf{d} + \mathbf{H}^{-1}\mathbf{w} \\ &= \mathbf{A}\mathbf{d} + \bar{\mathbf{w}} \end{aligned} \tag{3.12}$$

where $\bar{\mathbf{w}} = \mathbf{H}^{-1}\mathbf{w}$. After equalization, a GFDM demodulator is applied to reconstruct the data. In particular, $\hat{s}_{k,m}$ is obtained by reversing the frequency shift, circular convolving

with receive filter $g_{\mathrm{R}}[n]$, and downsampling the resulting signal at $n = mK$ according to:

$$\begin{aligned}\hat{s}_{k,m} &= \left(z[n]e^{-j2\pi\frac{k}{K}n}\right) \circledast g_{\mathrm{R}}[n]\Big|_{n=mK} \\ &= \sum_{n=0}^{N-1} z[n]g_{\mathrm{R}}[(mK-n)_N]e^{-j2\pi\frac{k}{K}n} \\ &= \sum_{n=0}^{N-1} z[n]\gamma_{k,m},\end{aligned} \tag{3.13}$$

where

$$\gamma_{k,m} = g_{\mathrm{R}}[(mK-n)_N]e^{-j2\pi\frac{k}{K}n}. \tag{3.14}$$

Stacking all demodulated data symbol $\hat{s}_{k,m}$ into a vector

$$\hat{\mathbf{d}} = [\hat{s}_{0,0}, \hat{s}_{1,0}, \ldots, \hat{s}_{K-1,0}, \hat{s}_{0,1}, \hat{s}_{1,1}, \ldots, \hat{s}_{K-1,M-1}]^{\mathrm{T}},$$

it then follows from (3.13) and (3.14) that

$$\hat{\mathbf{d}} = \mathbf{B}\mathbf{z}, \tag{3.15}$$

where

$$\mathbf{B} = \begin{bmatrix}\boldsymbol{\gamma}_{0,0} & \cdots & \boldsymbol{\gamma}_{K-1,0} & \boldsymbol{\gamma}_{0,1} & \cdots & \boldsymbol{\gamma}_{K-1,M-1}\end{bmatrix}^{\mathrm{T}} \tag{3.16}$$

with $\boldsymbol{\gamma}_{k,m} = [\gamma_{k,m}[0], \gamma_{k,m}[1], \ldots, \gamma_{k,m}[N-1]]^{\mathrm{T}}$. The demodulated data $\hat{\mathbf{d}}$ depends on the choice of the receive filter $g_{\mathrm{R}}[n]$ through matrix $\mathbf{B}$. There are several demodulation approaches for GFDM that have been investigated in literature [31]. In the following, two popular approacheas are reviewed, which are matched filter receiver (MFR) and zero-forcing receiver (ZFR).

Matched Filter Receiver

To realize the matched filter receiver, $g_{\mathrm{R}}[n]$ is chosen to be $g_{\mathrm{R}}[n] = g_{\mathrm{T}}[n] = g[n]$. Figure 3.5 illustrates an example of $g[n]$ that has coefficients from a discrete SRRC designed with $M = 3$, $K = 4$, and a roll-off factor $\beta = 0.5$. It is noted that the SRRC filter has an odd number of taps (13 taps). However, to enable circular convolution in GFDM, the length of $g[n]$ should be $N = KM = 12$. Thus, $g[n]$ is obtained by removing the last sample in $g_{\mathrm{SRRC[n]}}$ as shown in the center part of Figure 3.5. The lower part of Figure 3.5

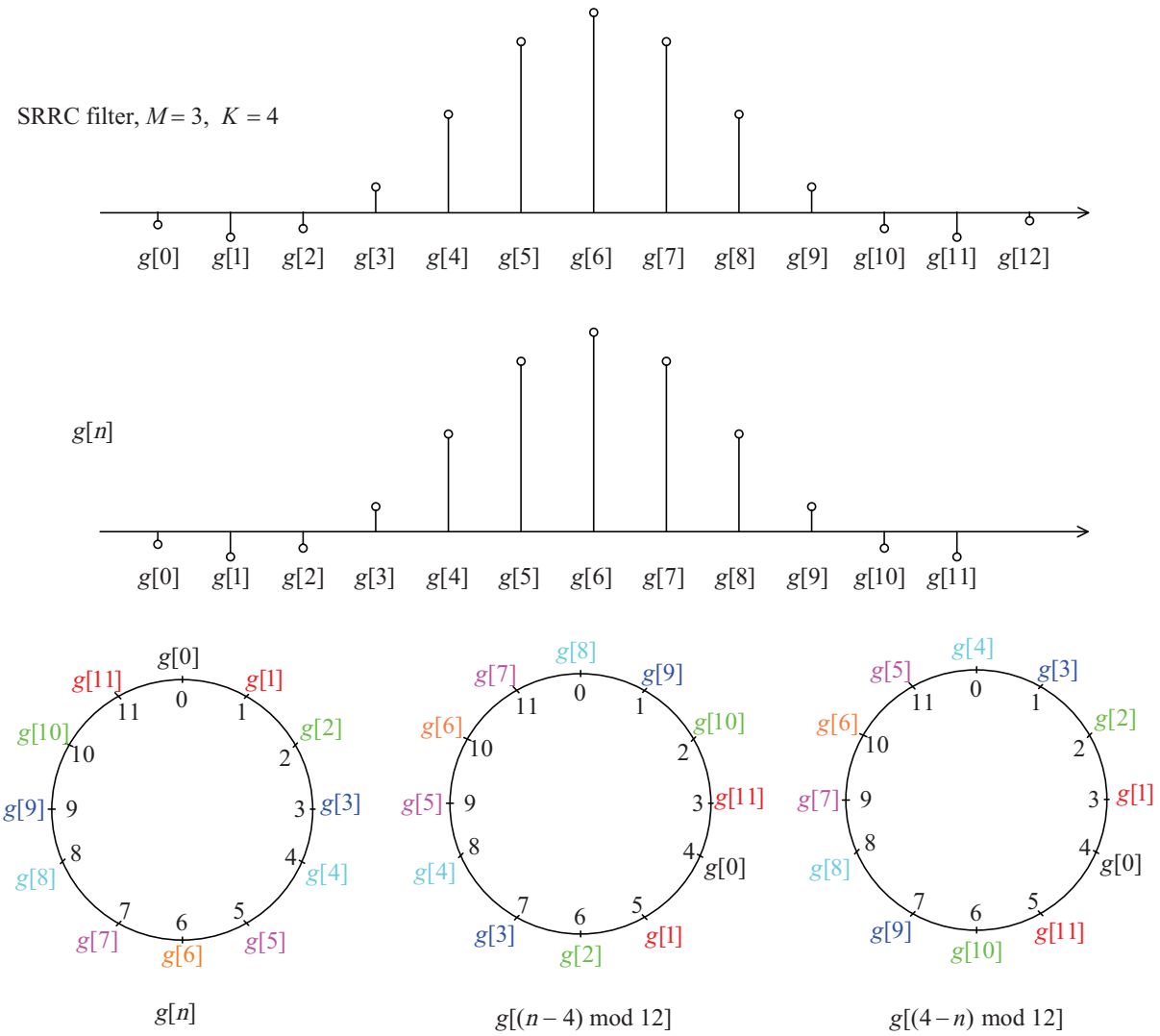

Figure 3.5: Illustration of the impulse response of the GFDM system with $K = 3$, and $K = 4$.

illustrates the coefficients of $g[n]$ in a circle and its circularly shifted versions. Two taps that have same color means that they have equal values. In this example, one can see that $g[(n-4)_{12}] = g[(4-n)_{12}]$. Generally, one can verifies that $g[(n-\alpha)_N] = g[(\alpha-n)_N]$. This property holds for any $g[n]$ that is even symmetric as the one shown in the upper part of Figure 3.5. However, the shape of $g[n]$ affects the ISI and ICI of a GFDM system, which can be analyzed as follow.

Using the above property and from (3.4), (3.14) one has $\gamma_{k,m} = g^*_{k,m}$. To investigate the

interference scenarios in a GFDM system, assume $z[n] = x[n]$ (i.e., disregard the effects of noise and channel). From (3.3) and (3.13) one has

$$\begin{aligned}
\hat{s}_{k',m'} &= \sum_{n=0}^{N-1}\sum_{k=0}^{K-1}\sum_{m=0}^{M-1} s_{k,m} g[(n-mK)_N] e^{j2\pi\frac{k}{K}n} g[(m'K-n)_N] e^{-j2\pi\frac{k'}{K}n} \\
&= s_{k',m'} \overbrace{g[(n-m'K)_N]g[(m'K-n)_N]}^{=1} + \overbrace{\sum_{\substack{m=0 \\ m\neq m'}} s_{k',m} \sum_{n=0}^{N-1} g[(n-mK)_N]g[(m'K-n)_N]}^{\text{ISI}} \\
&+ \overbrace{\sum_{\substack{k=0 \\ k\neq k'}}^{K-1} s_{k,m'} \sum_{n=0}^{N-1} |g[(n-m'K)_N]|^2 e^{j2\pi\frac{k-k'}{K}n}}^{\text{ICI caused by symbols from the same time slot}} \\
&+ \overbrace{\sum_{\substack{k=0 \\ k\neq k'}}^{K-1}\sum_{\substack{m=0 \\ m\neq m'}}^{M-1} s_{k,m} \sum_{n=0}^{N-1} g[(n-mK)_N]g[(m'K-n)_N] e^{j2\pi\frac{k-k'}{K}n}}^{\text{ICI caused by symbols from other time slots}}
\end{aligned} \tag{3.17}$$

As indicated in (3.17), there are three types of interference in GFDM system: ISI, ICI caused by symbols from the same time slot, and ICI caused by symbols from other time slots. Regarding ISI, it should be noted that in the continuous time domain $\int_{-\infty}^{\infty} g(t)g(mT-t)dt = g(t) * g(t)|_{t=mT} = 0$ if $g(t)$ is a SRRC filter. The term $\sum_{n=0}^{N-1} g[(n-mK)_N]g[(m'K-n)_N]$ in (3.17) is the approximate discrete version of $\int_{-\infty}^{\infty} g(t)g(mT-t)dt$ since $g[n]$ has a finite number of taps due to truncation and the shifting in discrete time is circular with period N. Figure 3.6 illustrates the power of $\sum_{n=0}^{N-1} g[(n-mK)_N]g[(m'K-n)_N]$ (ISI power) in dB versus the difference of $m-m'$ for RC and SRRC filters. One can see that the ISI power of the SRRC filter is lower than that of the RC filter since using a SRRC filter in the MF receiver satisfies the Nyquist condition. In addition, the larger roll-off factor the lowers the ISI power because a filter with a large roll-off factor decays faster and can be well approximated by a small number of taps.

The above discussion suggests that one should choose a SRRC filter with large β as the filter for a GFDM system because using such a filter lowers the ISI. However, ISI is not the only source of interference in a GFDM system. In fact, ICI is more problematic

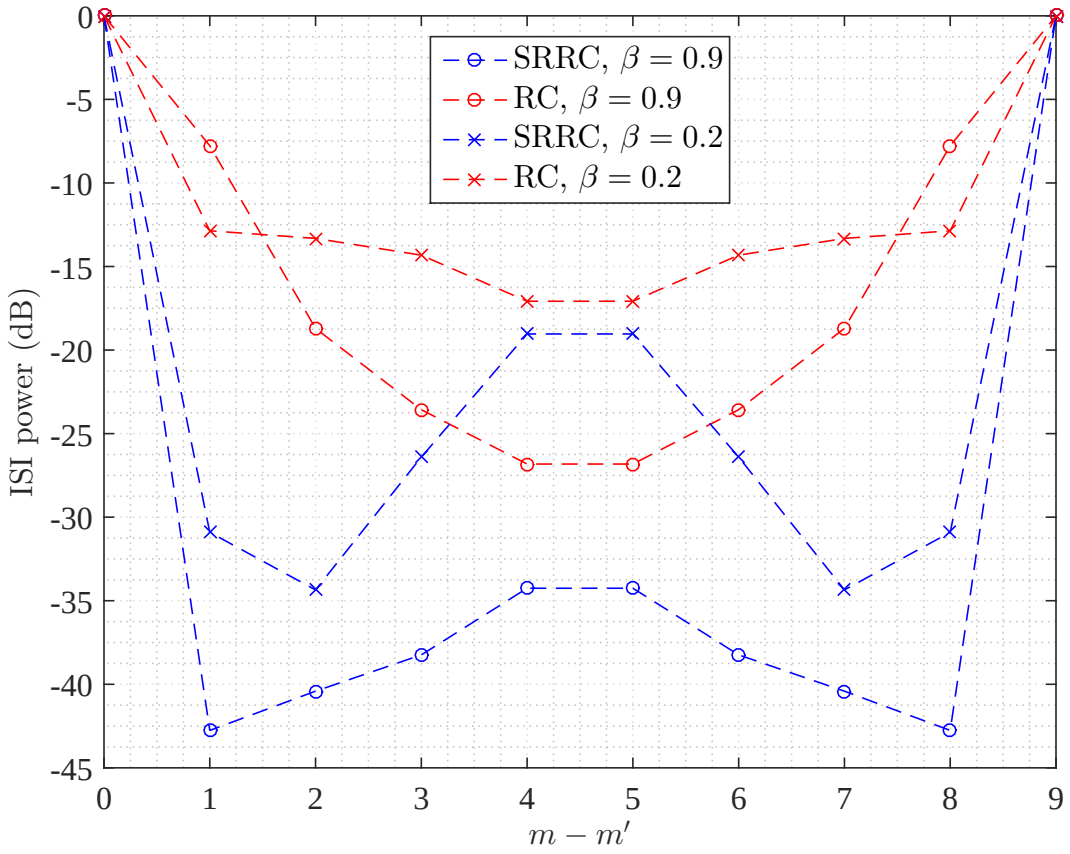

Figure 3.6: ISI power versus the difference of $m - m'$ for RC and SRRC filters. $g[n]$ is obtained from a RC or SRRC filter with $M = 9$ symbols and $K = 16$ samples per symbols.

than ISI in this system. To see the impact of ICI, recall that the GFDM modulation at the transmitter can be expressed as in (3.5) where matrix $\mathbf{A}$ characterizes the modulation process. In addition, for a MFR, $\mathbf{B} = \mathbf{A}^H$, which leads to

$$\begin{aligned} \hat{\mathbf{d}}_{\text{MF}} &= \mathbf{A}^H \mathbf{z} \\ &= \mathbf{A}^H \mathbf{A}\mathbf{d} + \mathbf{A}^H \bar{\mathbf{w}}, \end{aligned} \tag{3.18}$$

where $\hat{\mathbf{d}}_{\text{MF}}$ is the recovered vector using the MFR. It is noted that the term $\mathbf{A}^H\mathbf{A}$ characterizes the impacts of ISI and ICI in the recovered vector.

Figure 3.7 visualizes $\mathbf{A}^H\mathbf{A}$ in one GFDM block for $K = 16$, $M = 3$. Here, the filter is either SRRC or RC with $\beta = 0.2$ or $\beta = 0.9$. The main diagonal of the matrix represented in Figure 3.7 is associated with the desired information and all others values in the matrix represent the interferences at the output of the MFR.

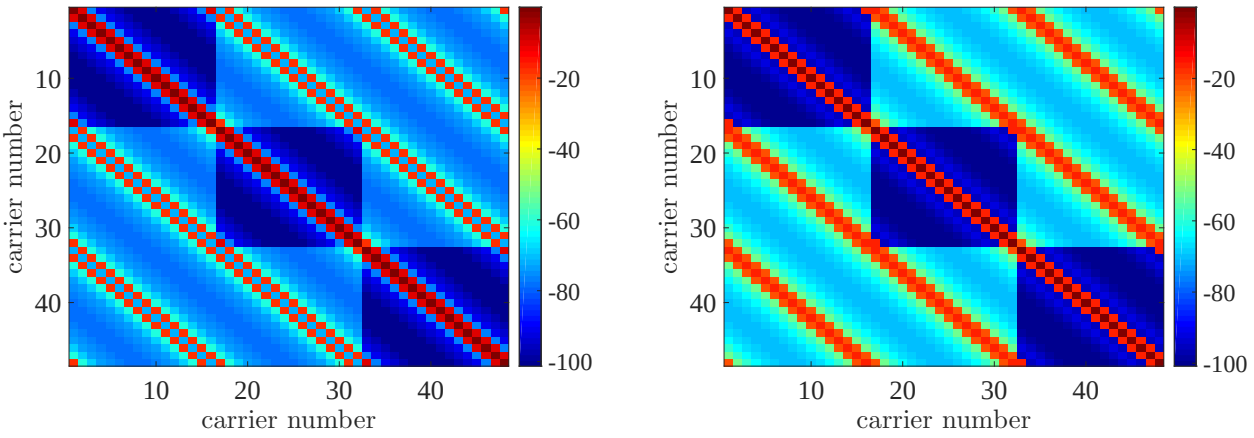

(a) SRRC, $\beta = 0.9$, SIR $= -0.256$ dB

(b) RC, $\beta = 0.9$, SIR $= 0.185$ dB

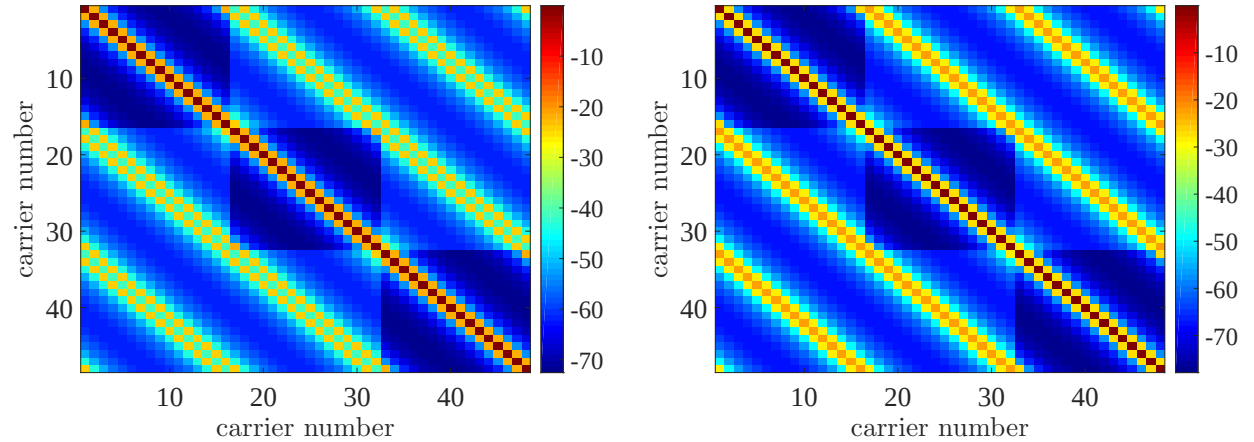

(c) SRRC, $\beta = 0.2$, SIR $= 3.099$ dB

(d) RC, $\beta = 0.2$, SIR $= 3.723$ dB

Figure 3.7: Interference patterns of a GFDM system with $M = 3$, and $K = 16$.

From Figure 3.7, one can see that the ICI caused by adjacent subcarriers is prominent and significantly larger than the one caused by non-adjacent subcarriers. In addition, filters with small β experience lower ICI than those with large β. This is due to the fact that the frequency responses of the SRRC and RC filters expand to the adjacent band, and the larger β, the more expansion. Figure 3.7 also shows that SRRC filters have lower ISI than RC filters, but RC filters have lower ICI than SRRC filters. The average signal-to-interference ratio (SIR) of the four cases are also shown in Figure 3.7. Observe that case (a), which uses a SRRC filter with large β, results in the smallest ISI. However, the large ICI outweights the benefit of low ISI. As such this case has the lowest SIR. Still using a SRRC filter but

with a smaller β, one can reduce the ICI and thus increase the SIR significantly as in case (c). Consider using a RC filter, one can make a tradeoff between ISI and ICI. For example, in case d), which uses a RC filter with small β, the system enjoys the largest SIR. Thus, this case might be a good choice for a GFDM system that is implemented with the matched filter receiver.

Zero-forcing Receiver

From (3.15), choosing $\mathbf{B} = \mathbf{A}^{-1}$ leads to a zero-forcing receiver. This gives

$$\begin{aligned} \hat{\mathbf{d}}_{\mathrm{ZF}} &= \mathbf{B}\mathbf{z} \\ &= \mathbf{A}^{-1}\mathbf{H}^{-1}\mathbf{y} \\ &= \mathbf{A}^{-1}\mathbf{H}^{-1}\left(\mathbf{H}\mathbf{A}\mathbf{d} + \mathbf{w}\right) \\ &= \mathbf{d} + \mathbf{A}^{-1}\mathbf{H}^{-1}\mathbf{w}, \end{aligned} \tag{3.19}$$

where $\hat{\mathbf{d}}_{\mathrm{ZF}}$ is the recovered vector using the zero-forcing approach. Consider the performance of the zero-forcing receiver over an AWGN channel, i.e., $\mathbf{H} = \mathbf{I}$. The nth element of $\hat{\mathbf{d}}_{\mathrm{ZF}}$ can be expressed as

$$\hat{d}_{\mathrm{ZF},n} = d_n + \sum_{n'=0}^{N-1} \left[\mathbf{A}^{-1}\right]_{n,n'} w_n \quad n = 0, 1, \ldots, N-1 \tag{3.20}$$

where $w_n \sim \mathcal{CN}(0, \mathcal{N}_0)$. Since $\mathbf{w} \sim \mathcal{CN}(0, \mathcal{N}_0\mathbf{I})$, the variables w_n, $n = 0, 1, \ldots, N-1$ are independent identically distributed (iid). Denote $\hat{w}_n = \sum_{n'=0}^{N-1} \left[\mathbf{A}^{-1}\right]_{n,n'} w_n$. The variance of $\hat{w}_n$ is given as

$$\mathrm{var}[\hat{w}_n] = \sum_{n'=0}^{N-1} \left| \left[\mathbf{A}^{-1}\right]_{n,n'} \right|^2 \mathcal{N}_0. \tag{3.21}$$

One can verify that $\mathrm{var}[\hat{w}_n]$ is equal for every n. Equation (3.20) can be rewritten as

$$\hat{d}_{\mathrm{ZF},n} = d_n + \hat{w}_n, \tag{3.22}$$

where $\hat{w}_n \sim \mathcal{CN}(0, \xi\mathcal{N}_0)$, and $\xi = \sum_{n'=0}^{N-1} \left|[\mathbf{A}^{-1}]_{n,n'}\right|^2$. Equation (3.22) shows that the zero-forcing receiver is able to completely remove the ICI resulted from the non-orthogonality between the subcarriers. However, this method enhances the noise power in the demodulated symbols because $\xi > 1$. Compare Equation (3.22) with the demodulated symbols of an OFDM system in Equation (2.49), it is expected that the BER curve of a GFDM system has

the same slope as the one of an OFDM system. However, the former experiences a power loss due to the noise enhancement factor ξ.

3.1.3 Efficient Implementation of GFDM

In this part, an efficient implementation for a GFDM system is presented. Then implementation complexity of different transmitter approaches is compared in term of complex valued multiplications.

The transmitted GFDM signal in (3.3) can be reformulated as:

$$x[n] = \sum_{m=0}^{M-1} g[(n-mK)_N] \sum_{k=0}^{K-1} s_{k,m} e^{j2\pi \frac{k}{K} n}. \tag{3.23}$$

Notice that the term $\sum_{k=0}^{K-1} s_{k,m} e^{j2\pi \frac{k}{K} n}$ for $n = 0, 1, \ldots, K-1$ is the K-point Inverse Discrete Fourier Transform (IDFT) of $\mathbf{s}_m = [s_{0,m}, \ldots, s_{K-1,m}]^{\mathrm{T}}$, which is expressed as $\mathbf{F}_K^H \mathbf{s}_m$, where $\mathbf{F}$ is the K-point Fourier Transform matrix. In addition, the sequence obtained from the IDFT is periodic with period K. Thus, for $n = 0, \ldots, N-1$ ($N = MK$), $\sum_{k=0}^{K-1} s_{k,m} e^{j2\pi \frac{k}{K} n}$ can be obtained by concatenating $\mathbf{F}_K^H \mathbf{s}_m$ M times, which is represented as $\mathbf{R}\mathbf{F}_K^H \mathbf{s}_m$ where $\mathbf{R} = [\mathbf{I}_K, \ldots, \mathbf{I}_K]^{\mathrm{T}}$ is the repetition matrix.

Multiplication with $g[(n-mK)_N]$ can be expressed by the matrix $\mathbf{G}_m = \mathrm{diag}(\mathbf{\Phi}_m \mathbf{g})$ where $\mathbf{g} = [g[0], \ldots, g[N-1]]^{\mathrm{T}}$, and $\mathbf{\Phi}_m$ is an $N \times N$ circulant matrix whose first column has only one non zero value, which is the mKth element. The matrix $\mathbf{G}_m$ circular shifting $g[n]$ according to time slot m.

Using the above matrix notation, one can rewrite (3.23) as

$$\mathbf{x} = \sum_{m=0}^{M-1} \mathbf{G}_m \mathbf{R} \mathbf{F}_K^H \mathbf{s}_m. \tag{3.24}$$

An example of (3.24) for $K = 3$, and $M = 2$ is illustrated in Figure 3.8. Note that in Figure 3.9, the coefficients $g_{n,m}$, $c_{n,m}$ is the nth element of $\mathbf{\Phi}_m \mathbf{g}$, $\mathbf{G}_m \mathbf{R} \mathbf{F}_K^H \mathbf{s}_m$, respectively.

The signal $\mathbf{x}$ is added a cyclic prefix and then transmitted through a channel with the input/output relationship expressed in (3.7). Then, the received signal is demodulated as

$$\hat{\mathbf{s}}_m = \mathbf{F}\mathbf{R}^{\mathrm{T}} \mathbf{G}_m \mathbf{S} \mathbf{y}, \tag{3.25}$$

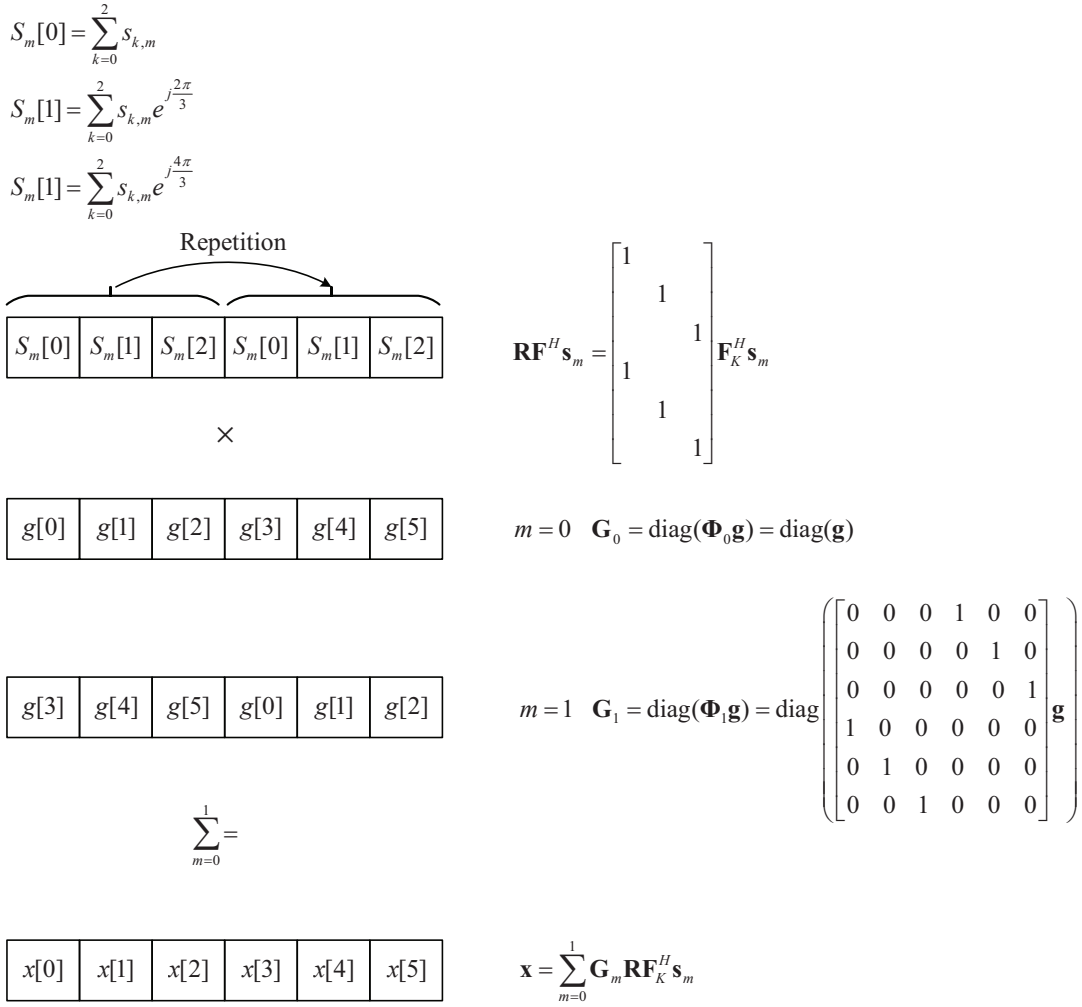

Figure 3.8: Illustration of (3.24) for $K = 3$, and $M = 2$.

where $\mathbf{S}$ represents the equalization. The transmitter and receiver approaches as in (3.24) and (3.25) can be implemented using the structure shown in Figure 3.9.

The GFDM transmitted signal so far has been expressed in the forms of (3.3), (3.5), and (3.24). It is not efficient to implement (3.3), and (3.5) directly. The number of complex valued multiplications that are required to produce $x[n]$ as in (3.5), and (3.24) are $C_{\mathrm{GFDM},\sum} = C_{\mathrm{GFDM},\mathbf{A}} = K^2M^2$. However, one can reduce the the complexity significantly by reformulating the GFDM transmitted signal as in (3.24) due to the benefit of the well known IFFT/FFT approach.

Assume that a K-point DFT can be implemented with the FFT algorithm at the ex-

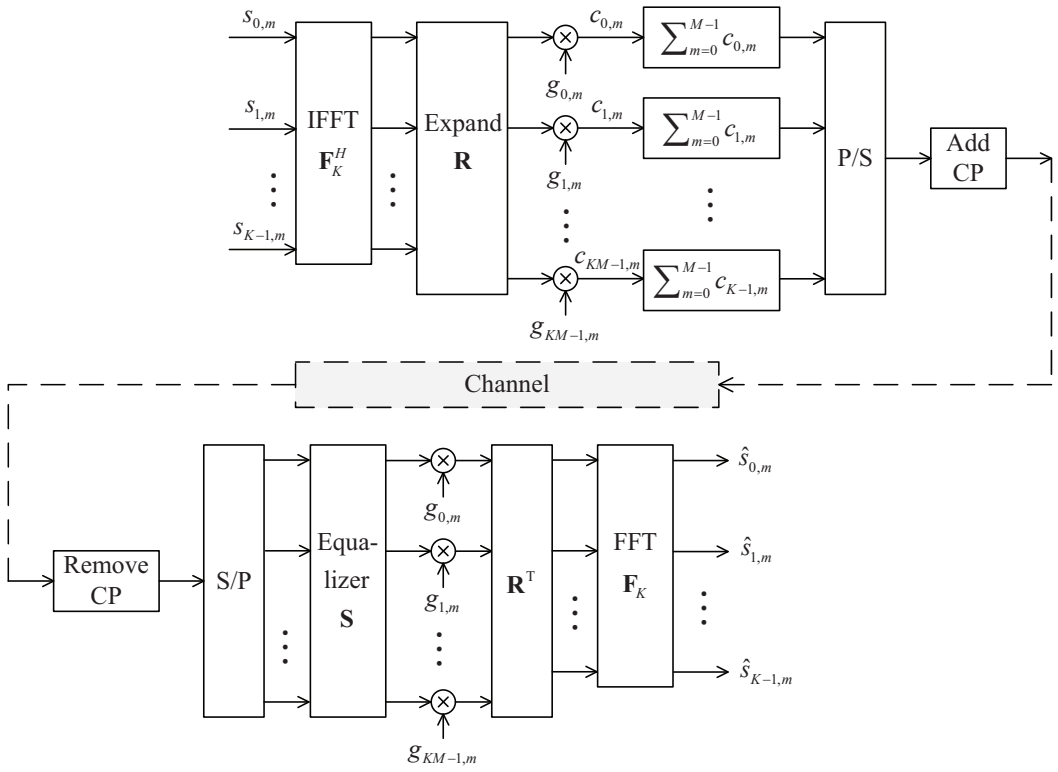

Figure 3.9: Efficient implementation of a GFDM system.

pense of $K \log_2 K$ complex valued multiplications. The complexity of performing (3.24) is as follows:

(i) Operation of $\mathbf{F}^H$ can be realized by a K-point FFT, which requires $K \log_2 K$ multiplications.

(ii) $\mathbf{G}_m$ is a diagonal matrix of size $MK \times MK$, thus it requires KM multiplications

(iii) The total number of multiplications to implement (3.24) is $C_{\text{GFDM,effcient}} = MK \log_2 M + M^2 K$

It should be noted that the operations related to $\mathbf{R}$ can be realized by means of pointer/memory operations and are thus not counted. In addition, only the complexity of the transmitter is addressed. A comparison of the implementation complexity of (3.3), (3.5), and (3.24) is provided in Figure 3.10 for a GFDM system with $K = 64$. Observe that the number

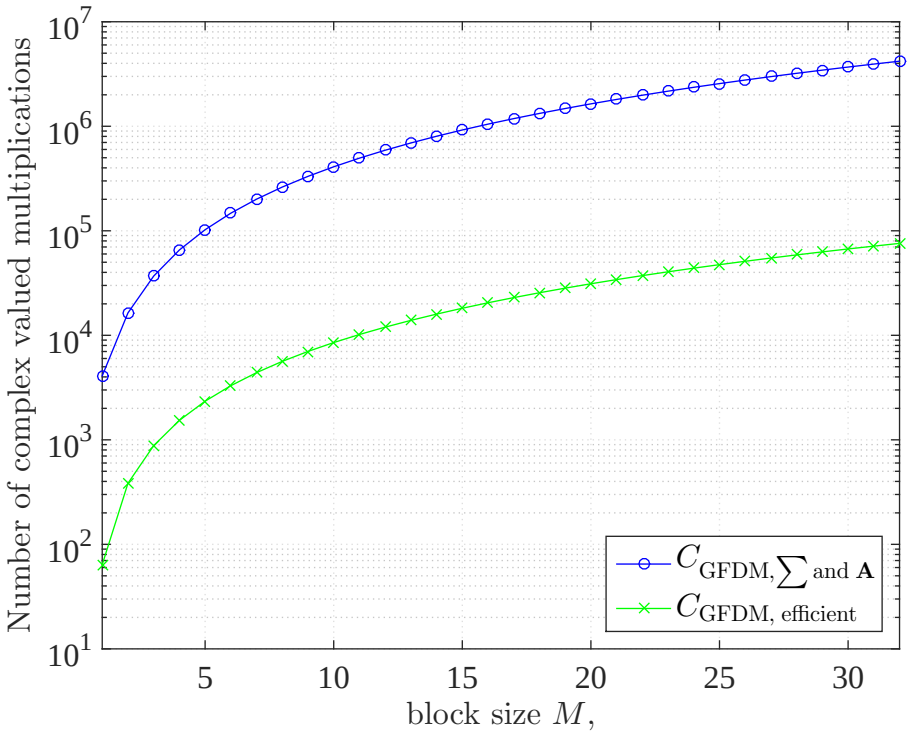

Figure 3.10: Comparison of implementation complexity of a GFDM system with $K = 64$.

of multiplications required by the efficient implementation method of (3.24) reduces by an order of 1.5 in magnitudes at $M = 32$ compared to the one of (3.3) and (3.5).

3.2 Circular Filterbank Multicarrier Communications Offset QAM (CFBMC-OQAM)

The FBMC-OQAM system has been presented in Section 2.3. It was shown that the FBMC-OQAM system is not only an orthogonal system but also able to use the well-localized prototype filter with desirable power spectrum density. However, an efficient implementation structure of FBMC-OQAM is not trivial. In addition, when transmitting the FBMC-OQAM signal through a frequency selective channel, the equalization at the receiver is not simple as compared to equalizatoin in an OFDM system. Using CP with the FBMC-OQAM system to ease the equalization is not feasible, because the length of the prototype filter in the time domain need to be taken into account, severely reducing the bandwidth efficiency.

Recently, a new multicarrier technique called Circular Filter Bank Multicarrier Offset

QAM (CFBMC-OQAM) was proposed [15], [32]. This system is an improvement of the FBMC-OQAM system since it preserves the orthogonality property and provides an efficient implementation structure as well as simple equalization. Those advantages of CFBMC-OQAM over FBMC-OQAM comes from the use of circular filtering, which is inspired by GFDM. In this section, first, the CFBMC-OQAM system is presented. Then the advantages of CFBMC-OQAM are demonstrated by comparison of its BER with that of GFDM.

3.2.1 CFBMC-OQAM Transmitter

The CFBMC-OQAM transceiver is illustrated in Figure 3.12. Similar to the GFDM system, a CFBMC-OQAM system also has a block-based structure that arranges the transmitted QAM symbols in a block of K subcarriers and M time slots as in (3.1). However, to enable OQAM, first, the real and imaginary parts of a complex QAM symbol, $s_{k,m} = s^R_{k,m} + js^I_{k,m}$, are separated and arranged in a $K \times 2M$ matrix as follows:

$$\begin{aligned}\mathbf{A} &= \begin{bmatrix} a_{0,0} & a_{0,1} & \cdots & a_{0,2M-1} \\ a_{1,0} & a_{1,1} & \cdots & a_{1,2M-1} \\ \vdots & \vdots & \ddots & \vdots \\ a_{K-1,0} & a_{K-1,1} & \cdots & a_{K-1,2M-1} \end{bmatrix} \\ &= \begin{bmatrix} s^R_{0,0} & s^I_{0,0} & \cdots & s^R_{0,M-1} & s^I_{0,M-1} \\ s^R_{0,0} & s^I_{0,0} & \cdots & s^R_{0,M-1} & s^I_{0,M-1} \\ \vdots & \vdots & \ddots & \vdots & \\ s^R_{0,0} & s^I_{0,0} & \cdots & s^R_{0,M-1} & s^I_{0,M-1} \end{bmatrix}.\end{aligned} \tag{3.26}$$

Then a phase offset of j^{k+m} is introduced to the real symbol $a_{k,m}$. Figure 3.11 shows the transmitted symbols after applying a phase offsets. The blue dots denote the real transmitted symbols and the red dots denote the imaginary transmitted symbols. One notices that the transmitted symbols are alternates of real and imaginary components between adjacent subcarriers and time slots.

Unlike GFDM, the transmitted sequence on each subcarrier of CFBMC-OQAM is upsampled by $K/2$. Note that the transmitted sequence on each subcarrier has length $2M$ and the

sequence after upsampling has length $N = MK$. The upsampled sequence is pulse shaped by circular convolving with filter $g[n]$ of length $N = MK$ and then shifted in frequency by the term $e^{j\frac{2\pi}{K}k}$. Following Figure 3.12, one finds that the elements of the transmitted vector $\mathbf{x} = [x[0], \ldots, x[N-1]]^{\mathrm{T}}$ are given as

$$x[n] = \sum_{k=0}^{K-1} \sum_{m=0}^{2M-1} j^{k+m} a_{k,m} g[(n - mK/2) \mod N] \mathrm{e}^{j2\pi kn/K}. \tag{3.27}$$

3.2.2 CFBMC-OQAM Receiver

Similar to the GFDM system, CP can be used in the CFBMC-OQAM system such that the relationship between vector $\mathbf{y}$ and vector $\mathbf{x}$ in Figure 3.12 is given as in (3.7). After equalizing to remove the effect of the channel, the vector $\mathbf{z}$ is processed similarly to the matched filter receiver of the GFDM system shown in Figure 3.1, except that the downsampling factor is $K/2$ and on each subcarrier the term $j^{-(k+m)}$ is added to remove the phase offset. Finally, the block $\mathbf{R}\{\bullet\}$ takes the real part of the complex values.

The demodulated symbol $\hat{a}_{k,m}$ in Figure 3.12 is given as

$$\hat{a}_{k,m} = \mathbf{R}\left\{ j^{-(k+m)} \sum_{n=0}^{N-1} g[(mK/2 - n)_N] e^{-j\frac{2\pi k}{K}n} z[n] \right\} \tag{3.28}$$

To investigate how a CFBMC-OQAM system handles ISI and ICI, assume $z[n] = x[n]$. Then

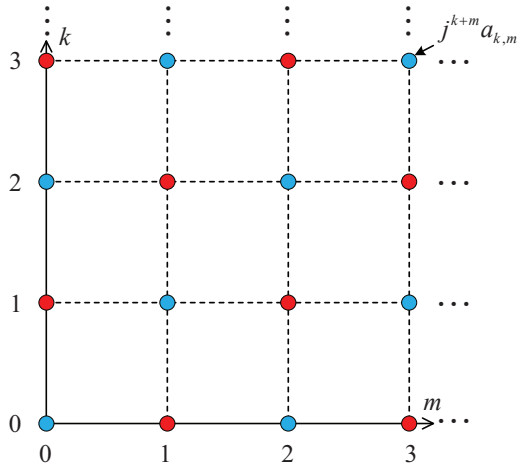

Figure 3.11: CFBMC-OQAM transmitted symbols after phase offset.

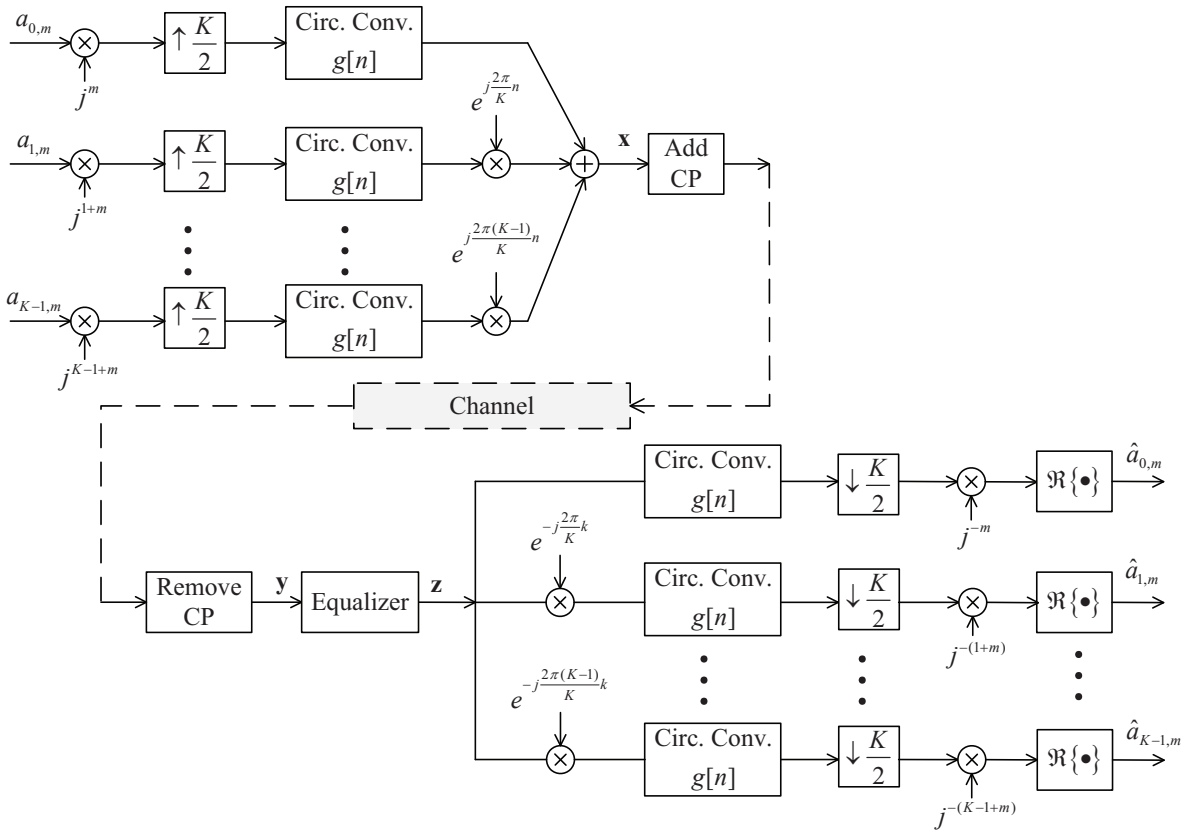

Figure 3.12: Block diagram of the CFBMC-OQAM transceiver.

from (3.27) and (3.28) the demodulated symbol $\hat{a}_{k,m}$ can be expressed as

$$
\begin{aligned}
&\hat{a}_{k',m'} \\
&= \mathbf{R}\left\{ j^{-(k'+m')} \sum_{n=0}^{N-1} g[(m'K/2-n)_N] e^{-j\frac{2\pi k'}{K}n} x[n] \right\} \\
&= \mathbf{R}\left\{ j^{-(k'+m')} \sum_{n=0}^{N-1} g[(m'K/2-n)_N] e^{-j\frac{2\pi k'}{K}n} \sum_{k=0}^{K-1} \sum_{m=0}^{2M-1} j^{k+m} a_{k,m} g[(n-mK/2)_N] e^{j2\pi kn/K} \right\} \\
&= a_{k',m'} \overbrace{\mathbf{R}\left\{ g[(m'K/2-n)_N] g[(n-m'K/2)_N] \right\}}^{=1} \\
&+ \overbrace{\sum_{\substack{m=0 \\ m\neq m'}}^{2M-1} a_{k',m} \mathbf{R}\left\{ j^{(m-m')} \sum_{n=0}^{N-1} g[(m'K/2-n)_N] g[(n-mK/2)_N] \right\}}^{\text{ISI}} \\
&+ \overbrace{\sum_{\substack{k=0 \\ k\neq k'}}^{K-1} a_{k,m'} \mathbf{R}\left\{ j^{(k-k')} \sum_{n=0}^{N-1} g[(m'K/2-n)_N] g[(n-m'K/2)_N] e^{j2\pi(k-k')n/K} \right\}}^{\text{ICI caused by symbols from the same time slot}}
\end{aligned}
$$

$$+\overbrace{\sum_{\substack{k=0\\k\neq k'}}^{K-1}\sum_{\substack{m=0\\m\neq m'}}^{2M-1} a_{k,m}\mathbf{R}\left\{j^{(k+m-k'-m')}\sum_{n=0}^{N-1} g[(m'K/2-n)_N]g[(n-mK/2)_N]e^{j2\pi(k-k')n/K}\right\}}^{\text{ICI caused by symbols from other time slots}} \tag{3.29}$$

Regarding the ISI term in (3.2.2), denote by I_{ISI} the result of taking the real part of the quantity inside the curly brackets. Then one can see that when $m-m'$ is an odd number, $I_{\text{ISI}} = \mathbf{R}\{\pm j \times \text{real number}\} = 0$. When $m-m'$ is an even number, one can verify that

$$\begin{aligned} I_{\text{ISI}} &= \mathbf{R}\left\{\sum_{n=0}^{N-1} g[(m'K/2-n)_N]g[(n-mK/2)_N]\right\} \\ &= \mathbf{R}\left\{\sum_{n=0}^{N-1} g[(u'K-n)_N]g[(n-uK)_N]\right\} \end{aligned} \tag{3.30}$$

The above equation shows that the I_{ISI} in CFBMC-OQAM for the case of even value of $m-m'$ is the same as the one in a GFDM system expressed in (3.17). Figure 3.13 plots the power of I_{ISI} versus $m-m'$. Only I_{ISI} values at even $(m-m')$ are displayed since when $m-m'$ is odd I_{ISI} is exactly equal to zero and then on the dB scale those values are infinity. The values of I_{ISI} at even $(m-m')$ have the same pattern as in the case of GFDM system shown in Figure 3.6.

For the ICI term caused by symbols from the same time slots in (3.2.2), denote by $I_{\text{ICI,s}}$ the result of taking the real part of the quantity inside the curly brackets. One has

$$\begin{aligned} I_{\text{ICI,s}} &= \mathbf{R}\left\{\sum_{n=0}^{N-1} |g[n-m'K/2]|^2 e^{j2\pi(k-k')n/K} e^{j\frac{\pi}{2}(k-k')}\right\} \\ &= \sum_{n=0}^{N-1} |g[n-m'K/2]|^2 \cos\left(\frac{2\pi(k-k')n}{K} + \frac{\pi}{2}(k-k')\right) \end{aligned} \tag{3.31}$$

When $k-k'$ is an odd number, $I_{\text{ICI,s}}$ is

$$I_{\text{ICI,s}} = (-1)^{\frac{k-k'+1}{2}} \sum_{n=0}^{N-1} |g[n-m'K/2]|^2 \sin\left(\frac{2\pi(k-k')n}{K}\right) \tag{3.32}$$

Figure 3.14 explains (3.32) by showing the terms $|g[n-m'K/2]|^2$, $\sin\left(\frac{2\pi(k-k')n}{K}\right)$, and their multiplication for the case of $m'=0$, $K=8$, $M=5$, and $k-k'=1$. One can see that $|g[n]|^2$ has length 40, and is even symmetric at $n=20$. Furthermore, $\sin\left(\frac{2\pi n}{K}\right)$ is odd

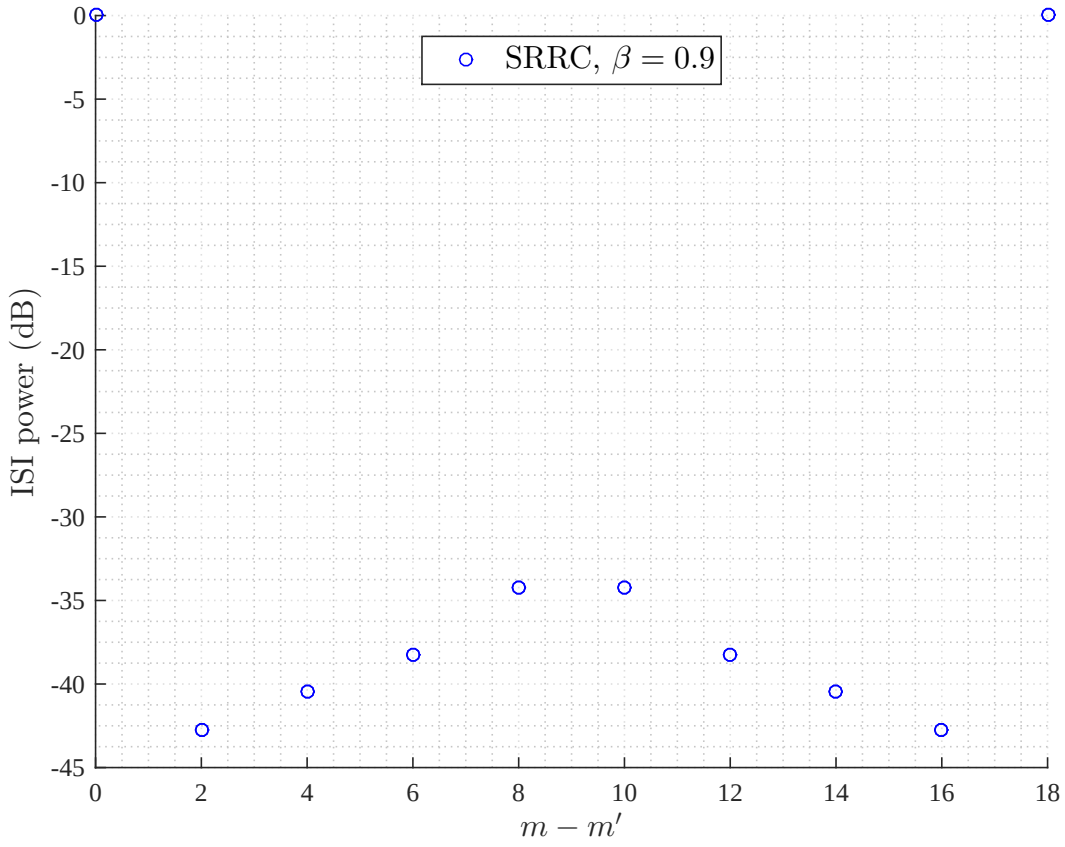

Figure 3.13: ISI power versus the difference of $m-m'$, CFBMC-OQAM with SRRC, $\beta = 0.9$, $K = 16$, and $M = 9$.

symmetric at $n = 20$. Thus, their multiplication is odd symmetric at $n = 20$ and then $-\sum_{n=0}^{N-1} |g[n]|^2 \sin\left(\frac{2\pi n}{K}\right) = 0$. For other values of m', $|g[n - m'K/2]|^2$ is a circular shift of $|g[n]|^2$ then it is circular even symmetric at $n = (20 + m'K/2)_N$. Meanwhile, for any odd value of $k - k'$, $\sin\left(\frac{2\pi(k-k')n}{K}\right)$ is circular odd symmetric at any n which is a multiple of $K/2$. Therefore (3.32) holds true for any m' and odd value of $k - k'$. Figure 3.15 illustrates another example where $m' = 3$ and $k - k' = 3$.

The above discussion proves that ICI from adjacent subcarriers ($k - k' = 1$) in CFBMC-OQAM system can be eliminated successfully. Furthermore, it can be shown that the ICI from non-adjacent subcarriers that satisfies $k - k' = 2u + 1$ can also be eliminated. Next, evaluate (3.31) for the case when $k - k' = 2u$. One can verify that

$$I_{\text{ICI,s}} = (-1)^{\frac{k-k'}{2}} \sum_{n=0}^{N-1} |g[n - m'K/2]|^2 \cos\left(\frac{2\pi(k-k')n}{K}\right) \tag{3.33}$$

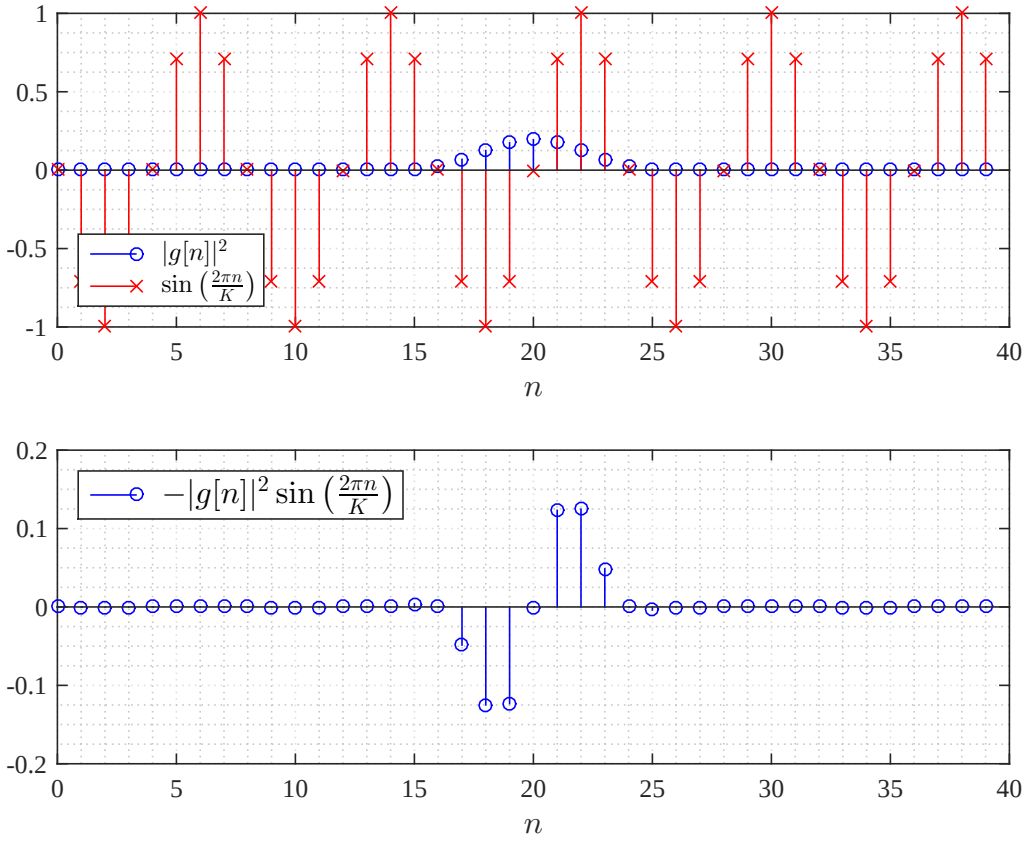

Figure 3.14: Illustration of the terms in (3.32) when $M = 5$, $K = 8$, SRRC filter with $\beta = 0.9$, $m' = 0$, and $k - k' = 1$.

Figure 3.16 illustrates the terms in (3.33) for the case when $m' = 0$ and $k - k' = 2$. One can see that $|g[n]|^2 \cos\left(\frac{2\pi 2n}{K}\right)$ does not have the circular odd symmetric property as in the case $k - k' = 1$. Then, $I_{\text{ICI,s}}$ is not exactly equal to 0. Therefore, the ICI from non-adjacent subcarriers such that $k - k' = 2u$ still remains. However, it can be substantially reduced by choosing the appropriate filters that fully extend up to the center of the adjacent subcarrier [32]. This choice minimizes stop band response of the filter which is the key factor in decreasing interference from far subcarriers. For example, if one chooses to use a SRRC filter for CFBMC-OQAM then a large roll-off factor β is a better choice than the small roll-off in terms of reducing ICI due to far subcarriers. Figure 3.17 illustrates the power of $I_{\text{ICI,s}}$ versus even $(k - k')$ for different values of β and M. It is clear that increasing β or M reduces the power of $I_{\text{ICI,s}}$ significantly. Note that M is the number of truncated symbols of the SRRC filter and thus large M (and β) indicates that $g[n]$ is well truncated in the time

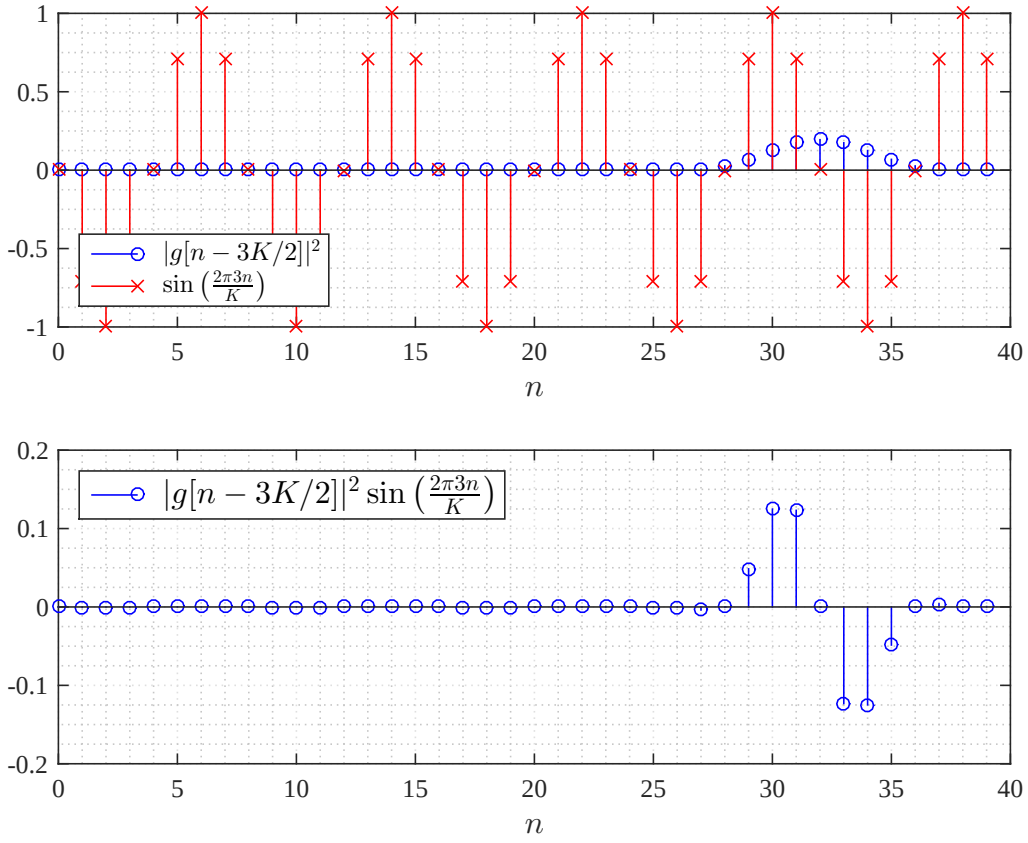

Figure 3.15: Illustration of the terms in (3.32) when $M = 5$, $K = 8$, SRRC filter with $\beta = 0.9$, $m' = 3$, and $k - k' = 3$.

domain which results in good stop-band attenuation.

Finally, for the ICI term caused by symbols from other time slots in (3.2.2), the result of taking the real part of the quantity inside the curly brackets can be expressed as

$$I_{\text{ICI,o}} = \sum_{n=0}^{N-1} g[(m'K/2 - n)_N] g[(n - mK/2)_N] \cos\left(\frac{2\pi(k-k')n}{K} + \frac{\pi}{2}(k + m - k' - m')\right) \tag{3.34}$$

If $g[n]$ is circular even symmetric then one can verify that $g[(m'K/2 - n)_N] g[(n - mK/2)_N]$ is also circular even symmetric at

$$n_{\text{sym}} = \frac{MK}{2} + \bar{m}\frac{K}{2} - (m - m')\frac{K}{4},$$

where $\bar{m} = \max(m, m')$ as shown in Figure 3.18. Evaluate the term $\cos\left(\frac{2\pi(k-k')n}{K} + \frac{\pi}{2}(k +\right.$

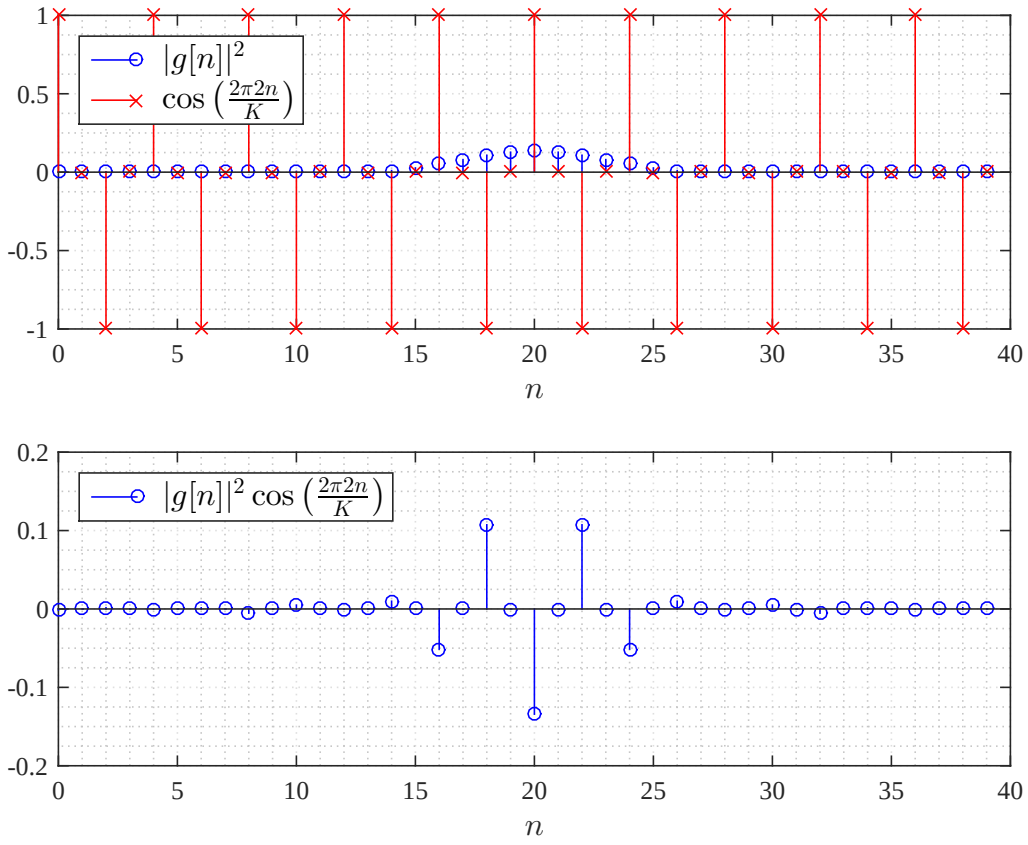

Figure 3.16: Illustration of the terms in (3.33) when $M = 5$, $K = 8$, SRRC filter with $\beta = 0.9$, $m' = 0$, and $k - k' = 2$.

$m - k' - m')\Big)$ at n_{sym}, one has

$$\begin{aligned}
&\cos\left(\frac{2\pi(k-k')n_{\text{sym}}}{K} + \frac{\pi}{2}(k+m-k'-m')\right) \\
&= \cos\left(\frac{2\pi}{K}(k-k')\left(\frac{MK}{2} + \bar{m}\frac{K}{2} - (m-m')\frac{K}{4}\right) + \frac{\pi}{2}(k+m-k'-m')\right) \\
&= \cos\left(\pi(\bar{m}+M)(k-k') - \frac{\pi}{2}(k-k')(m-m') + \frac{\pi}{2}(k+m-k'-m')\right)
\end{aligned} \tag{3.35}$$

For $k - k' = 2u + 1$,

$$\begin{aligned}
&\cos\left(\frac{2\pi(k-k')n_{\text{sym}}}{K} + \frac{\pi}{2}(k+m-k'-m')\right) \\
&= \cos\left(\pi(\bar{m}+M)(2u+1) - \frac{\pi}{2}(2u+1)(m-m') + \frac{\pi}{2}(2u+1+m-m')\right) \\
&= \cos\left(\pi(\bar{m}+M)(2u+1) - \pi u(m-m') + \frac{\pi}{2}(2u+1)\right) \\
&= 0
\end{aligned} \tag{3.36}$$

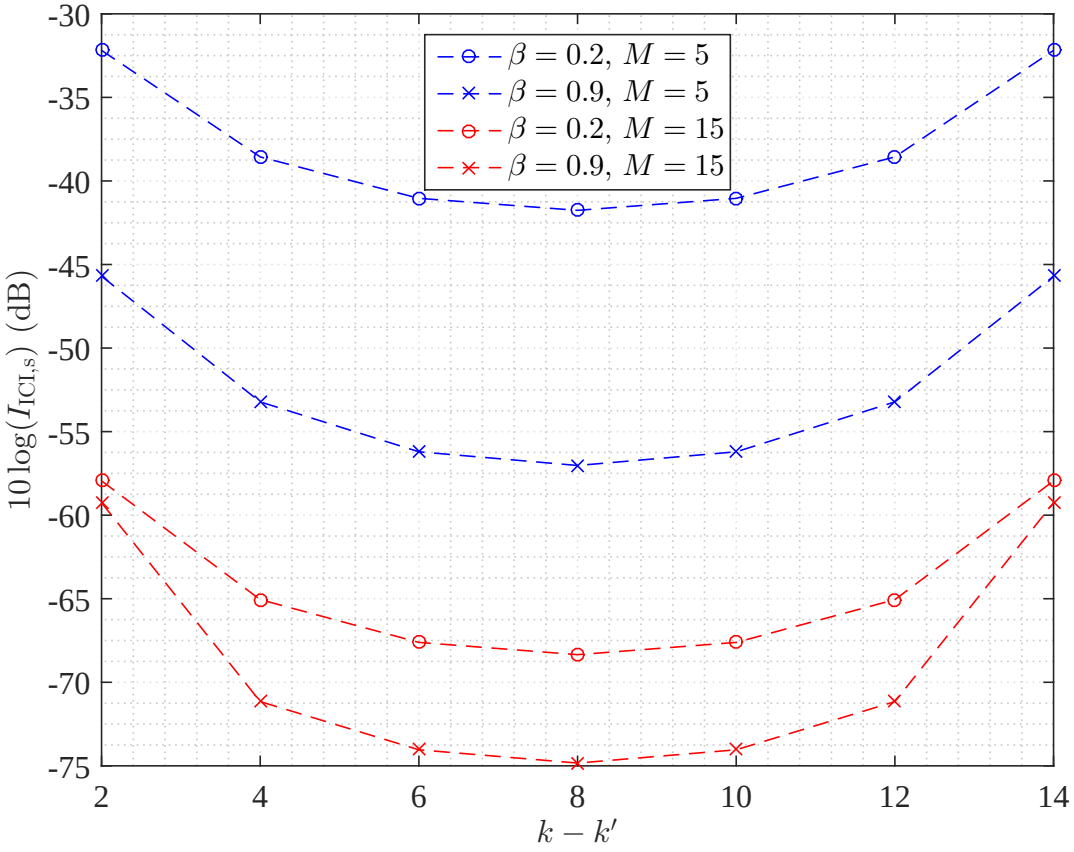

Figure 3.17: The power of $I_{\mathrm{ICI,s}}$ versus $k-k'$ for various values of β, and M. $K=16$, and the filter is SRRC.

Equation (3.36) implies that $\cos\left(\frac{2\pi(k-k')n}{K}+\frac{\pi}{2}(k+m-k'-m')\right)$ is circular odd symmetric at n_{sym} for $k-k'=2u+1$. Thus, $g[(m'K/2-n)_N]g[(n-mK/2)_N]\cos\left(\frac{2\pi(k-k')n}{K}+\frac{\pi}{2}(k+m-k'-m')\right)$ is circular odd symmetric at n_{sym} as shown in Figure 3.18 and then $I_{\mathrm{ICI,o}}=0$ for $k-k'=2u+1$. Therefore the ICI caused by symbols from other time slots where those symbols are in subcarriers separated by $k-k'=2u+1$ can be completely eliminated in a CFBMC-OQAM system.

For the case when $k-k'=2u$ and $m-m'=2u'+1$, Equation (3.35) can be rewritten as

$$\begin{aligned}&\cos\left(\frac{2\pi(k-k')n_{\mathrm{sym}}}{K}+\frac{\pi}{2}(k+m-k'-m')\right)\\&=\cos\left(\pi(\bar{m}+M)2u-\pi u(2u+1)+\pi u+\frac{\pi}{2}(2u'+1)\right)\\&=0.\end{aligned}\tag{3.37}$$

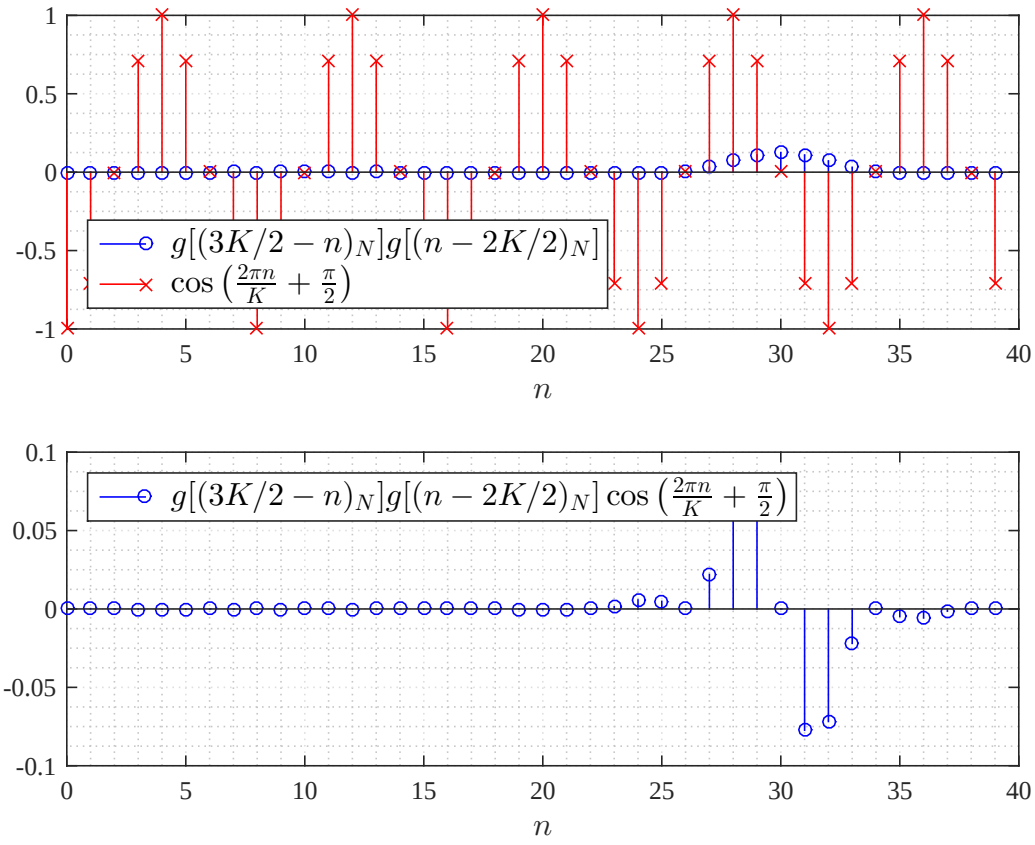

Figure 3.18: Illustration of the terms in (3.34) when $M = 5$, $K = 8$, SRRC filter with $\beta = 0.9$, $m = 2$, $m' = 3$, $k = 1$, $k' = 2$. One can see that $n_{\text{sym}} = 20 + 3\frac{8}{2} - (3-2)\frac{8}{4} = 30$.

For the case when $k - k' = 2u$ and $m - m' = 2u'$, Equation (3.35) can be rewritten as

$$\begin{aligned} &\cos\left(\frac{2\pi(k-k')n_{\text{sym}}}{K} + \frac{\pi}{2}(k+m-k'-m')\right) \\ &= \cos\left(\pi(\bar{m}+M)2u - \pi u(2u+1) + \pi u + \pi u'\right) \\ &= \pm 1. \end{aligned} \tag{3.38}$$

Similar to the case when $k - k' = 2u + 1$, from (3.38) one concludes that the ICI caused by symbols from other time slots where those symbols are in subcarriers separated by $k - k' = 2u$ and in subsymbols separated by $m - m' = 2u' + 1$ can be successfully eliminated. Equation (3.37) and (3.34) imply that the ICI caused by symbols from other time slots where those symbols are in subcarriers separated by $k - k' = 2u$ and in subsymbols separated by $m - m' = 2u'$ can not be completely eliminated. The power of $I_{\text{ICI,o}}$ in this case depends on $\sum_{n=0}^{N-1} g[(m'K/2 - n)_N]g[(n - mK/2)_N]$, which is the ISI power depicted in Figure 3.13.

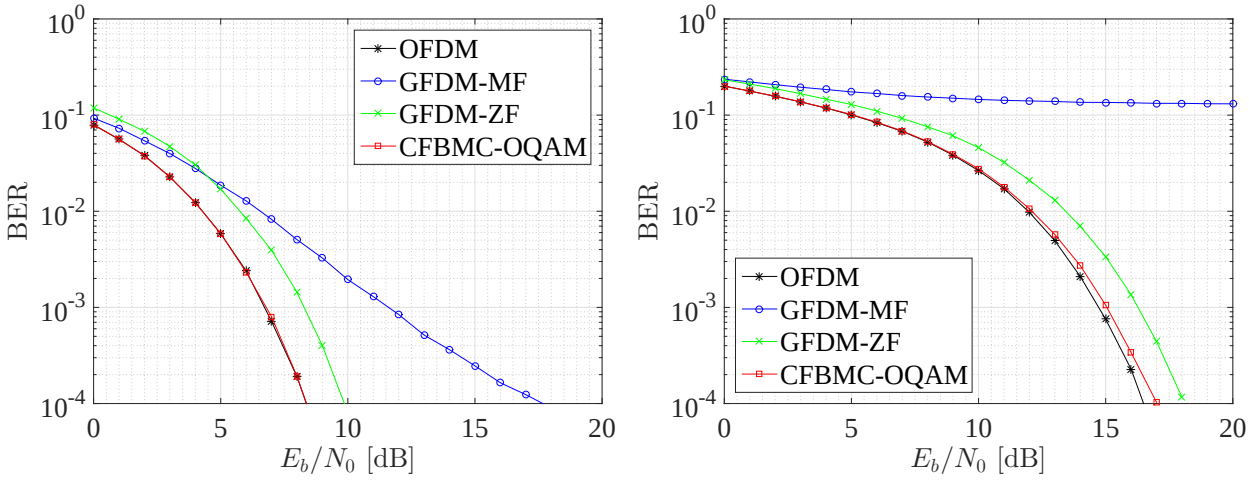

(a) 4-QAM

(b) 64-QAM

Figure 3.19: BER performance of OFDM, GFDM, and CFBMC-OQAM over AWGN channel. $K = 64$, $M = 31$, SRRC filter with $\beta = 0.5$.

Therefore, as one carefully designs $g[n]$ so that it minimizes the ISI then the ICI in the case when $k - k' = 2u$ and $m - m' = 2u'$ is also minimized.

Compared to a GFDM system, CFBMC-OQAM has a better mechanism to handle interference, especially the ICI. This leads to a better BER performance. Figure 3.19 shows the BER performance of OFDM, GFDM and CFBMC-OQAM over an AWGN channel. One can see that GFDM-ZF performs far better than GFDM-MF and CFBMC-OQAM achieves the same BER performance as OFDM, which is around 4 dB better than the performance of GFDM-ZF at BER of 10^{-4}. With a large constellation size, the performance loss of GFDM-MF becomes unacceptably, while CFBMC-OQAM's performance still matches that of OFDM.

Next, the BER performances of OFDM, GFDM, and CFBMC-OQAM systems over frequency selective channels (FSCs) are simulated. The results will show that the BER performances of these systems over FSCs can be badly affected if the channels experience zeros on its unit circle (also known as spectral null).

To understand the effect of channel spectral nulls on the BER performance of OFDM, GFDM, and CFBMC-OQAM, consider two frequency selective channels, each having four

Table 3.1: Impulse response of $h_1[n]$ and $h_2[n]$

n	$h_1[n]$	$h_2[n]$
0	$0.3699 + 0.5782j$	$0.3903 + 0.1049j$
1	$0.4053 + 0.575j$	$0.6050 + 0.1422j$
2	$0.0834 + 0.0406j$	$0.4402 + 0.0368j$
3	$-0.1587 + 0.0156j$	$0.0714 + 0.5002j$

coefficients as listed in Table 3.1. The magnitude response (in dB) of two channels $h_1(n)$ and $h_2(n)$ are shown in Figure 3.20a. The channel $h_1(n)$ has a relatively flat magnitude response compared to the channel $h_2(n)$ which has a zero around $\omega = 1.1\pi$ and its magnitude response shows more variations. The energy of the two channels has been normalized to 1.

Figures 3.20b and 3.20c show the BER performance of OFDM, GFDM, and CFBMC-OQAM over channel $h_1(n)$, $h_2(n)$, respectively. One observes that in channel $h_1(n)$ the BER performances of OFDM and CFBMC-OQAM are almost identical and there is a gap of 1 dB at the BER level of 10^{-4} between these curves and the performance curve of OFDM. When the channel experiences a zero as in the case of $h_2(n)$, the BER curves of the three techniques flat out for $20 \leq E_b/N_0 \leq 40$ dB. This is because in this SNR range the average BER of the systems is dominated by errors of the bad subchannels that experience the channel null. When $E_b/N_0 > 40$ dB the errors of the bad subchannels become less and the overall BER curves get better. The "local" error floor of the BER curves in Figure 3.20c is similar to what observed in [18]. It is pointed out that the ranges of E_b/N_0 in Figures 3.20b and 3.20c are different. Specifically, CFBMC-OQAM only requires $E_b/N_0 = 16$ dB to have a BER of 10^{-4} in channel $h_1(n)$ whereas more than 40 dB is needed to obtain the same level of BER in channel $h_2(n)$.

3.2.3 Efficient Implementation of CFBMC-OQAM

Given the similarity between the transceivers of GFDM and CFBMC-OQAM systems as shown in Figures 3.1 and 3.12, the efficient implementation structure for a GFDM system shown in Figure 3.9 can be extended for a CFBMC-OQAM system. Figure 3.21 shows the

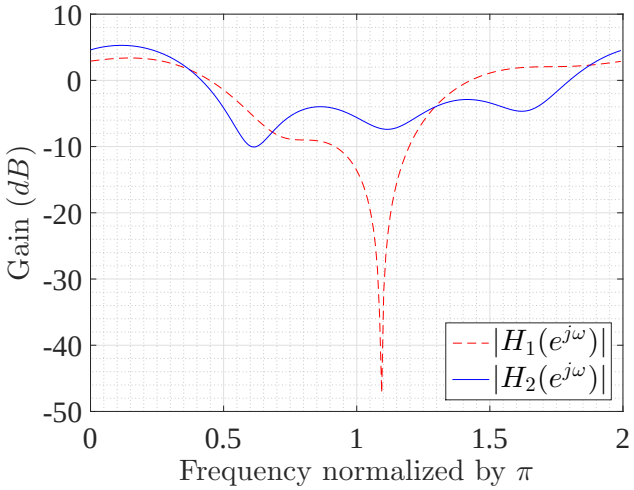

(a) Magnitude responses of the two channels $h_1[n]$, and $h_2[n]$

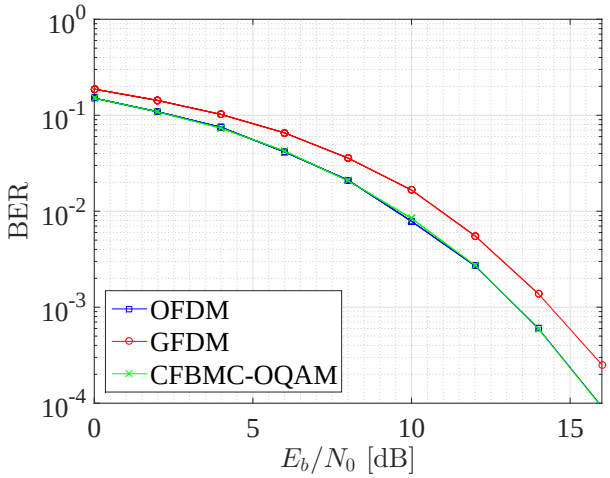

(b) Performance of OFDM, GFDM, and CFBMC-OQAM over channel $h_1[n]$.

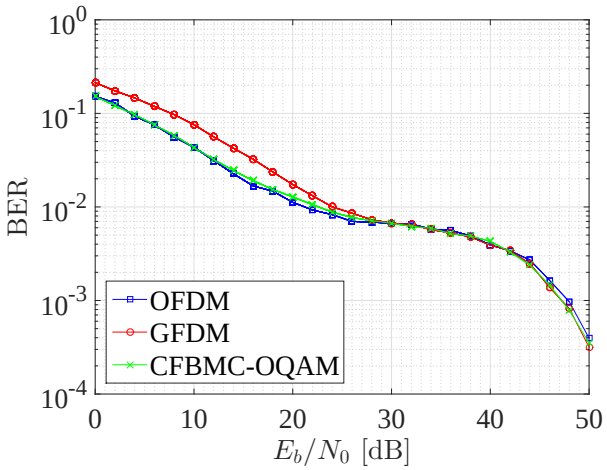

(c) Performance of OFDM, GFDM, and CFBMC-OQAM over channel $h_2[n]$.

Figure 3.20: Illustration of the spectral null effect on the BER performance of the three multicarriers techniques.

polyphase structure of a CFBMC-OQAM system. Following this structure, the transmitted CFBMC-OQAM signal can be expressed as

$$\mathbf{x} = \sum_{m=0}^{2M-1} \mathbf{G}_m \mathbf{R} \mathbf{F}_K^H \mathbf{J}_m \mathbf{a}_m, \tag{3.39}$$

where $\mathbf{a}_m$ is the mth column of matrix $\mathbf{A}$ in (3.26), $\mathbf{J}_m = \text{diag}([j^m, j^{m+1}, \ldots, j^{m+K-1}])$ is a matrix that introduces phase offsets, $\mathbf{F}_K$ is the K-point FFT matrix, $\mathbf{R} = [\mathbf{I}_K, \ldots, \mathbf{I}_K]^\top$ is the repetition matrix, $\mathbf{G}_m = \text{diag}(\mathbf{\Phi}_m \mathbf{g}) = \text{diag}([g_{0,m}, g_{1,m}, \ldots, g_{KM-1,m}])$, and $\mathbf{\Phi}_m$ is a $KM \times KM$ circulant matrix whose first column has only one non zero value, which is the $(mK/2)$th element with value 1. In this structure, $\mathbf{a}_m$ is first transformed into the time domain by multiplying it with an inverse FFT matrix, $\mathbf{F}_K^H$. Upsampling is performed by repeating the $K \times 1$ transformed vector M times with the $KM \times K$ matrix $\mathbf{R}$. The resulted vector is pulse-shaped by point-wise multiplication with the circularly shifted version of the prototype filter, which is $\mathbf{\Phi}_m \mathbf{g}$. Then the transmitted signal is obtained by summing all pulse-shaped subsymbol vectors.

At the receiver, first, an equalizer $\mathbf{S}$ is applied to the received signal $\mathbf{y}$ to remove the effect of multipath interference. Then, the equalized vector is processed in dual to (4.9). The equalized output that can be used to detect the data symbols for the mth time slot is given by

$$\hat{\mathbf{a}}_m = \Re\{\mathbf{J}_m^H \mathbf{F}_K \mathbf{R}^\top \mathbf{G}_m \mathbf{S} \mathbf{y}\}. \tag{3.40}$$

3.3 Summay

This chapter has introduced GFDM and CFBMC-OQAM system. The two systems share the same filtering process where circular convolution is utilized instead of linear convolution. Using circular convolution for filtering allows the two systems to use filters which have better stop-band attenuation than the rectangular filter used for OFDM systems without increasing the length of CP. In addition, efficient implementation structure developed for a GFDM system can be adapted for a CFBMC-OQAM system. The chapter also exlained how GFDM and CFBMC-OQAM deal with ISI and ICI. A GFDM system, when using MF receiver, lacks a mechanism to handle ICI, especially the severe ICI caused by symbols from the adjacent subcarriers. Whereas, a CFBMC-OQAM system, due to the use of offset QAM, can completely remove ICI from adjacent subcarriers. The simulation results which compare the BER performance of GFDM and CFBMC-OQAM systems over AWGN and FSC channels are also provided. It was demonstrated that the CFBMC-OQAM system is

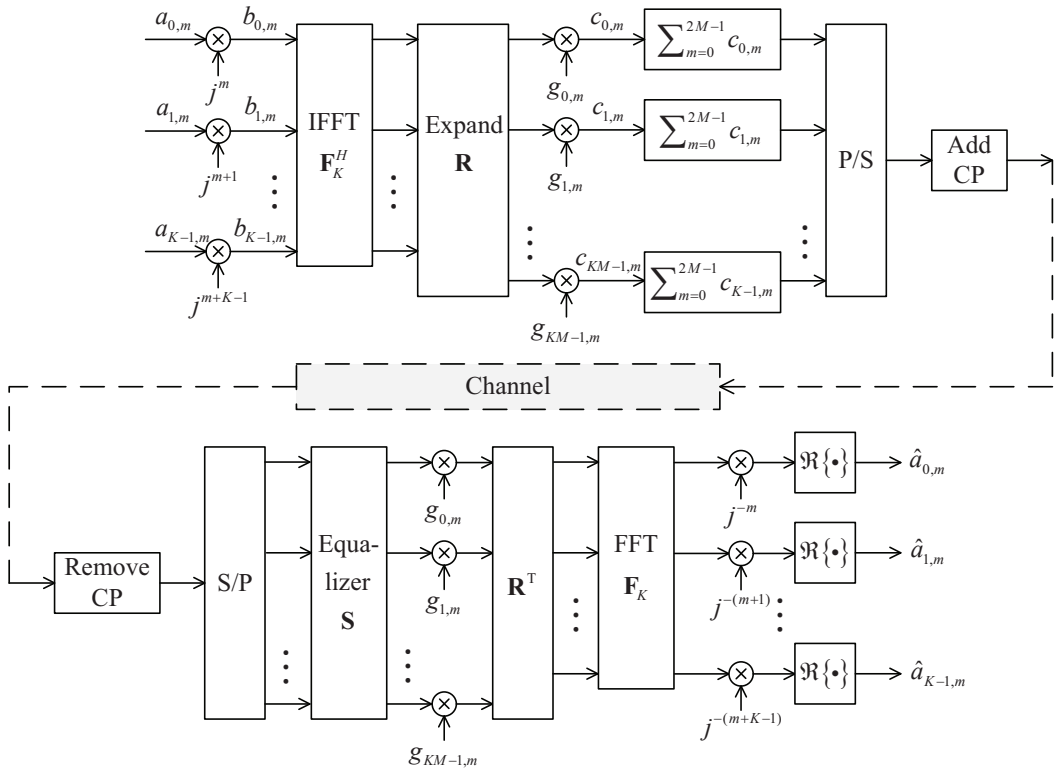

Figure 3.21: Efficient implementation of a CFBMC-OQAM system.

superior than the GFDM system. However, without additional processing techniques, the BER performance of CFBMC-OQAM in FSCs might be significantly degraded due to the spectral nulls effect. And thus more robust transceiver designs are required.

4. Walsh-Hadamard(WH)-CFBMC-OQAM

In the previous chapter, the transceiver structures of GFDM and CFBMC-OQAM system were introduced. The key differences between those techniques were highlighted. In particular, the advantages of CFBMC-OQAM over GFDM were illustrated. In addition, it was pointed out that without additional processing techniques the BER performance of OFDM, GFDM, and CFBMC-OQAM in frequency selective channels (FSCs) can be badly affected if the channels have spectral nulls.

To have transceivers whose performance is more robust to channel nulls, many techniques have been developed in the literature [8]. For example, in OFDM system with K subcarriers, instead of transmitting K symbols on K subcarriers within one OFDM block, one can transmit only $L < K$ symbols on L subcarriers, where the choice of L subcarriers is different for different OFDM blocks. This technique can achieve frequency diversity gain of K by coding across the subcarriers within one OFDM block as well as across different blocks [7]. Another well known method to prevent the BER performance being dominated by the bad subchannels is using a precoder, or using bit allocation techniques [33].

The focus of this chapter is on precoding schemes. There is a number of precoding techniques that have been proposed for multicarreir systems. Those precoded schemes are different in how they are designed and in their objectives. For example, the conventional CP-OFDM system experiences high peak to average power ratio PAPR. Then one can consider to use DFT precoder which is demontrated in [19] to produce very low PAPR. In fact, the precoded scheme in [19] leads to the well-known single carrier system with cyclic prefix (SC-CP) where the receiver performs both Discrete Fourier Transform (DFT) and Inverse DFT (IDFT) operations. Another example is [16], which proposed precoded and vector OFDM to

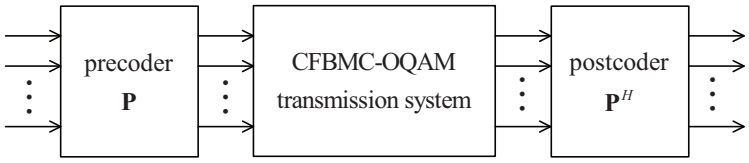

Figure 4.1: Precoded CFBMC-OQAM system.

combat channel spectral nulls. This precoded scheme aims at improving BER performance as well as reducing the overhead of inserting CP. On the other hand, reference [17] investigates linear precoding for an OFDM system to maximize the diversity gain and coding gain. Reference [21] proposes a precoded scheme for GFDM system, called Walsh-Hadamard(WH)-GFDM, to improve its BER over FSCs.

In this chapter, a precoded scheme for CFBMC-OQAM is studied. It is shown that the precoded CFBMC-OQAM outperforms the non-precoded scheme in terms of BER performance in FSCs, especially in channels with spectral nulls. The rest of this chapter is organized as follow. In Section 4.1, the system model for precoded CFBMC-OQAM is introduced. Section 4.2 analyzes the BER performance of the precoded scheme over FSCs and derives a theoretical approximation for the BER. Section 4.3 compares performance of the proposed scheme with that of OFDM, CFBMC-OQAM, GFDM, and WH-GFDM.

4.1 System Model

Figure 4.1 shows an CFBMC-OQAM transmission system with a precoder at the transmitter and a post-coder at the receiver. It should be mentioned that this thesis chooses the precoder $\mathbf{P}$ to be an unitary matrix such that $\mathbf{P}^H\mathbf{P} = \mathbf{I}$. The reason for this choice is that as the CFBMC-OQAM system is orthogonal such that its transmission matrix is an identity matrix, and the precoder and post-coder satisfy $\mathbf{P}^H\mathbf{P} = \mathbf{I}$, the precoded system transmission matrix remains identity.

Among unitary precoder matrices, a unitary precoder $\mathbf{P}$ whose elements, $p_{m,n}$, satisfies

$$\left|p_{m,n}\right| = \frac{1}{\sqrt{M}}, \quad 0 \leq m, n \leq M-1. \tag{4.1}$$

is considered. This type of precoder can achieve the so-called error-equalizing property [33],

which means the subchannels' noise variances are equalized to the average value and thus all the subchannels' BERs are the same. One of the well-known unitary matrices satisfying the equal magnitude property in (4.1) is the Walsh-Hadamard (WH) matrix. A nice property of WH matrix is that it requires only additions for implementation since its entries are either 1 or -1.

Figure 4.2 illustrates an equivalent complex baseband of an WH-CFBMC-OQAM system. Like the conventional CFBMC-QOAM, in the precoded WH-CFBMC-OQAM, the information symbols are processed in blocks, each involving K subcarriers and M time slots. Let $s_{k,m} = s^R_{k,m} + j s^I_{k,m}$ be the complex QAM data symbol associated with the kth subcarrier and mth time slot. To enable offset QAM (OQAM) modulation, the real and imaginary parts of a complex QAM symbol are separated and arranged in a $K \times 2M$ matrix as follows:

$$\begin{aligned}\mathbf{A} &= \begin{bmatrix} a_{0,0} & a_{0,1} & \cdots & a_{0,2M-1} \\ a_{1,0} & a_{1,1} & \cdots & a_{1,2M-1} \\ \vdots & \vdots & \ddots & \vdots \\ a_{K-1,0} & a_{K-1,1} & \cdots & a_{K-1,2M-1} \end{bmatrix} \\ &= \begin{bmatrix} s^R_{0,0} & s^I_{0,0} & \cdots & s^R_{0,M-1} & s^I_{0,M-1} \\ s^R_{0,0} & s^I_{0,0} & \cdots & s^R_{0,M-1} & s^I_{0,M-1} \\ \vdots & \vdots & \ddots & \vdots & \\ s^R_{0,0} & s^I_{0,0} & \cdots & s^R_{0,M-1} & s^I_{0,M-1} \end{bmatrix}.\end{aligned} \tag{4.2}$$

The K data streams at the input in Figure 4.2 are the K rows of matrix $\mathbf{A}$. This structure is basically the polyphase structure of CFBMC-OQAM presented in the previous chapter, except that a WH precoder is applied to the input.

The WH precoder is applied for each column of $\mathbf{A}$ as

$$\tilde{\mathbf{a}}_m = \mathbf{W}\mathbf{a}_m, \tag{4.3}$$

where $\mathbf{a}_m$ is the mth column of $\mathbf{A}$, $\mathbf{W}$ is a $K \times K$ WH matrix and $\tilde{\mathbf{a}}_m$ is the mth precoded

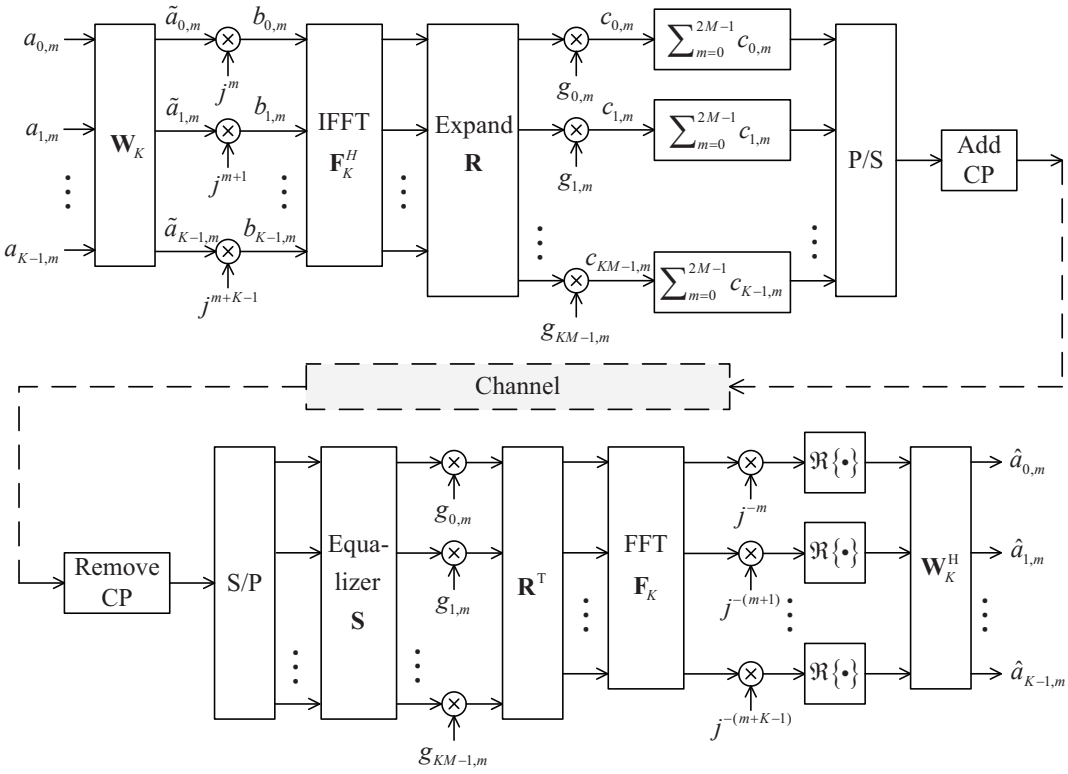

Figure 4.2: Equivalent complex baseband WH-CFBMC-OQAM system.

column vector.

$$\mathbf{W}_K = \frac{1}{\sqrt{K}} \begin{bmatrix} \mathbf{W}_{K/2} & \mathbf{W}_{K/2} \\ \mathbf{W}_{K/2} & -\mathbf{W}_{K/2} \end{bmatrix}, \ \mathbf{W}_2 = \frac{1}{\sqrt{2}} \begin{bmatrix} 1 & 1 \\ 1 & -1 \end{bmatrix}. \tag{4.4}$$

Similar to the conventional CFBMC-OQAM, the phase offsets are introduced to the real and imaginary components of QAM symbols on different subcarriers as follows:

$$\mathbf{b}_m = \mathbf{J}_m \tilde{\mathbf{a}}_m \tag{4.5}$$

where $\mathbf{J}_m = \mathrm{diag}([j^m, j^{m+1}, \ldots, j^{m+K-1}])$. Then, the WH-CFBMC-OQAM transmitted signal is given as [34]

$$x[n] = \sum_{k=0}^{K-1} \sum_{m=0}^{2M-1} j^{k+m} \tilde{a}_{k,m} g[(n - mK/2)_N] \mathrm{e}^{j2\pi kn/K}, \tag{4.6}$$

where $n = 0, 1, \ldots, N = KM - 1$, $\tilde{a}_{k,m}$ is the kth element of $\tilde{\mathbf{a}}_m$, $g[n]$ is the impulse response of a prototype filter, which has KM coefficients, and $g[(n - z)_w]$ denotes cyclically shifting $g[n]$ by z positions with period w.

The polyphase structure [15] for the implementation of (4.6) as shown in Fig. 4.2 is the most efficient method and can be described clearly in matrix form. Let

$$\mathbf{x} = [x[0], x[1], \ldots, x[KM-1]]^\top, \tag{4.7}$$

and $\mathbf{g} = [g[0], g[1], \ldots, g[KM-1]]^\top$ be the transmitted vector and vector of filter coefficients, respectively. Then the matrix form representation of (4.6) is

$$\mathbf{x} = \sum_{m=0}^{2M-1} \mathbf{G}_m \mathbf{R} \mathbf{F}^H \mathbf{b}_m, \tag{4.8}$$

where $\mathbf{F}$ is the K-point FFT matrix, $\mathbf{R} = [\mathbf{I}_K, \ldots, \mathbf{I}_K]^\top$, $\mathbf{G}_m = \text{diag}(\mathbf{\Phi}_m \mathbf{g})$ and $\mathbf{\Phi}_m$ is a $KM \times KM$ circulant matrix whose first column has only one non zero value, which is the $(mK/2)$th element with value 1. In this structure, $\mathbf{b}_m$ is first transformed into the time domain by multiplying it with an inverse FFT matrix, $\mathbf{F}^H$. Upsampling is performed by repeating the $K \times 1$ transformed vector M times with the $KM \times K$ matrix $\mathbf{R}$. The resulted vector is pulse-shaped by point-wise multiplication with the circularly shifted version of the prototype filter, which is $\mathbf{\Phi}_m \mathbf{g}$. Then the transmitted signal is obtained by summing all pulse-shaped subsymbol vectors. Substituting (4.3) and (4.5) into (4.8), the transmitted signal of WH-CFBMC-OQAM can be expressed as

$$\mathbf{x} = \sum_{m=0}^{2M-1} \mathbf{G}_m \mathbf{R} \mathbf{F}^H \mathbf{J}_m \mathbf{W} \mathbf{a}_m. \tag{4.9}$$

In a frequency selective channel, WH-CFBMC-OQAM uses a cyclic prefix (CP) of length L to achieve free inter-block interference (IBI). Let $\mathbf{h} = [h[0], h[1], \cdots, h[V-1]]^\top$ ($V \ll N = MK - 1$) be the vector of an V-taps channel impulse response. As long as $V - 1 \leq L$, free IBI is guaranteed at the receiver. In that case, the received signal after removing CP can be written as

$$\mathbf{y} = \mathbf{H}\mathbf{x} + \mathbf{n}, \tag{4.10}$$

where $\mathbf{H}$ is a $KM \times KM$ circulant matrix whose first column is $\mathbf{h}$ appended with $N - V$ zeros, and $\mathbf{n}$ is a vector of additive while Gaussian noise (AWGN) samples.

An approach to demodulate data is described in Fig. 4.2 [15]. First, an equalizer $\mathbf{S}$ is applied to the received signal $\mathbf{y}$ to remove the effect of multipath interference. Then, the

equalized vector is processed in dual to (4.9). The equalized signal that can be used to detect the data symbol for the mth time slot is given by

$$\hat{\mathbf{a}}_m = \mathbf{W}^H \Re\{\mathbf{J}_m^H \mathbf{F}\mathbf{R}^\top \mathbf{G}_m \mathbf{S}\mathbf{y}\}. \tag{4.11}$$

Let $\mathbf{D}_m = \mathbf{J}_m^H \mathbf{F}\mathbf{R}^\top \mathbf{G}_m$. Consider a non-precoding system operating in an ideal channel where $\mathbf{W} = \mathbf{I}$, and $\mathbf{S} = \mathbf{I}$. The equalized signal is

$$\begin{aligned}
\hat{\mathbf{a}}_m &= \mathcal{R}\left\{\mathbf{D}_m \sum_{m'=0}^{2M-1} \mathbf{D}_{m'}^H \mathbf{a}_{m'}\right\}. \\
&= \sum_{m'=0}^{2M-1} \left[\mathcal{R}\left\{\mathbf{D}_m \mathbf{D}_{m'}^H\right\}\right] \mathbf{a}_{m'} \\
&= \mathcal{R}\left\{\mathbf{D}_m \mathbf{D}_m^H\right\} \mathbf{a}_m + \sum_{\substack{m'=0 \\ m' \neq m}}^{2M-1} \mathcal{R}\left\{\mathbf{D}_m \mathbf{D}_{m'}^H\right\} \mathbf{a}_{m'}
\end{aligned} \tag{4.12}$$

Perfect reconstruction is achieved, i.e., $\hat{\mathbf{a}}_m = \mathbf{a}_m$ if the following condition is satisfied:

$$\mathcal{R}\left\{\mathbf{D}_m \mathbf{D}_{m'}^H\right\} = \begin{cases} \mathbf{I}, & \text{if} \quad m = m' \\ \mathbf{0}, & \text{if} \quad m \neq m' \end{cases}, \tag{4.13}$$

where $\mathbf{0}$ is the $K \times K$ zero matrix.

The previous chapter has discussed the effects of ISI and ICI on the demodulation of symbol $\hat{a}_{k,m}$, which is the kth element of $\hat{\mathbf{a}}_m$. Equation (4.12) gives another expression of those equalized symbols. Further, it helps one to analyze how close a practical design of a CFBMC-OQAM system approximates the perfect reconstruction condition in (4.13). Recall that the entries of $\mathbf{a}_m$ are real parts of QAM symbols. Assume that the constellation is normalized and QAM symbols are uncorrelated, one has

$$E\{\mathbf{a}_m\} = \mathbf{0}, \quad E\{\mathbf{a}_m \mathbf{a}_m^H\} = \mathbf{I}, \quad E\{\mathbf{a}_m \mathbf{a}_{m'}^H\} = \mathbf{0}. \tag{4.14}$$

Then one can verify that

$$E\{\hat{\mathbf{a}}_m \hat{\mathbf{a}}_m^H\} = \mathcal{R}\left\{\mathbf{D}_m \mathbf{D}_m^H\right\} \left(\mathcal{R}\left\{\mathbf{D}_m \mathbf{D}_m^H\right\}\right)^H + \sum_{\substack{m'=0 \\ m' \neq m}}^{2M-1} \mathcal{R}\left\{\mathbf{D}_m \mathbf{D}_{m'}^H\right\} \left(\mathcal{R}\left\{\mathbf{D}_m \mathbf{D}_{m'}^H\right\}\right)^H, \tag{4.15}$$

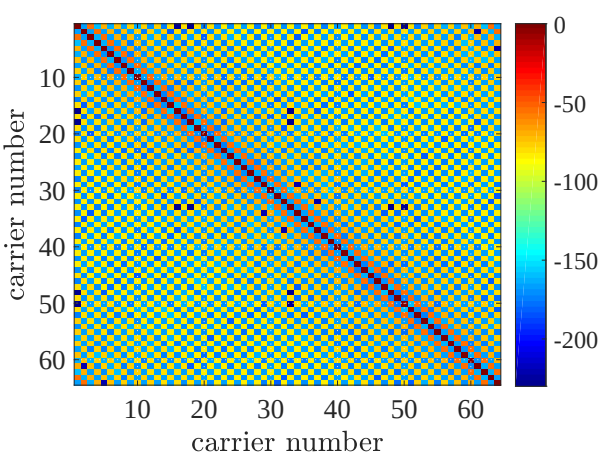

(a) $\mathcal{R}\left\{\mathbf{D}_m\mathbf{D}_m^H\right\}\left(\mathcal{R}\left\{\mathbf{D}_m\mathbf{D}_m^H\right\}\right)^H$

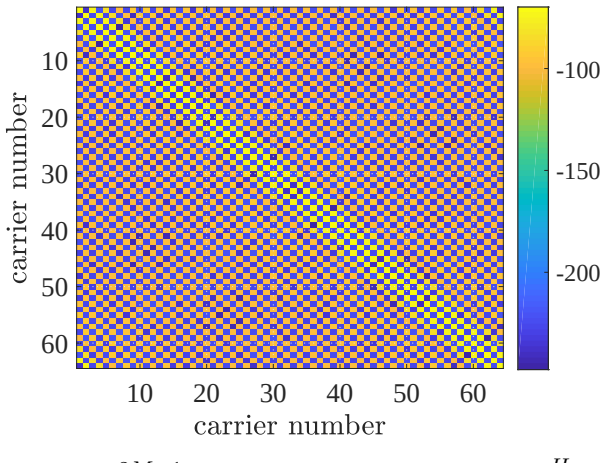

(b) $\sum_{\substack{m'=0\\m'\neq m}}^{2M-1}\mathcal{R}\left\{\mathbf{D}_m\mathbf{D}_{m'}^H\right\}\left(\mathcal{R}\left\{\mathbf{D}_m\mathbf{D}_{m'}^H\right\}\right)^H$

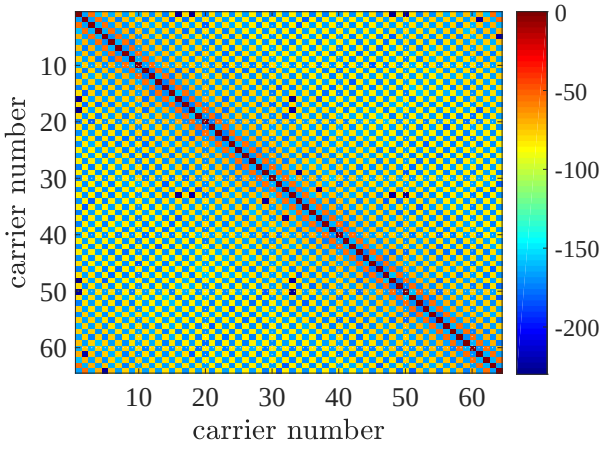

(c) $E\{\hat{\mathbf{a}}_m\hat{\mathbf{a}}_m^H\}$

Figure 4.3: Visualization of the terms in Equation (4.15).

where $E\{\hat{\mathbf{a}}_m\hat{\mathbf{a}}_m^H\}$ is a covariance matrix that characterizes the correlation between entries of $\hat{\mathbf{a}}_m$. Entry $[E\{\hat{\mathbf{a}}_m\hat{\mathbf{a}}_m^H\}]_{k,k'}$ is the interference power caused by $a_{k',m}$ when one demodulates $a_{k,m}$. The first term on the right hand side of (4.15) represents the ICI caused by symbols from the same time slots, and the second term represents the ICI caused by symbols from all other time slots. Figure 4.3 illustrates these terms for a CFBMC-OQAM system with $K = 64$, $M = 15$, and an SRRC filter ($\beta = 0.9$). The ICI power in this example is summarized in Table 4.1. Notice that the ISI power when $m \neq m'$ is significantly lower than that when $m = m'$. Overall, $E\{\hat{\mathbf{a}}_m\hat{\mathbf{a}}_m^H\}$ has a diagonal structure as illustrated in Figure 4.3c. This particular example shows that a design of CFBMC-OQAM where a SRRC filter

Table 4.1: ICI power (dB) for the example illustrated in Figure 4.3.

$k-k'$	$m=m'$	$m\neq m'$
0	0 dB	-80
odd	-200	-240
even	$[-50, -80]$	$[-80, -110]$

is utilized almost satisfies condition (4.13) with some certain level of approximation.

4.2 Performance Analysis

This section analyzes the BER performance of WH-CFBMC-OQAM over FSCs. Since $\mathbf{W}\mathbf{W}^H = \mathbf{I}$ and assume that (4.13) holds, $\hat{a}_{k,m}$ for $k = 0, 1, \ldots, K-1$ can be detected separately. Then, BER performance can be analyzed by analyzing the filtered noise power at the output of $\mathbf{W}^H$.

Consider the zero-forcing equalizer, i.e., $\mathbf{S} = \mathbf{H}^{-1}$. Then (4.11) becomes

$$\begin{aligned}\hat{\mathbf{a}}_m &= \mathbf{W}_K^H \mathcal{R}\left\{\mathbf{J}_m^H \mathbf{F}_K \mathbf{R}^\top \mathbf{G}_m \mathbf{H}^{-1}\left[\mathbf{H}\mathbf{x}+\mathbf{n}\right]\right\}. \\ &= \mathbf{a}_m + \hat{\mathbf{n}}_m,\end{aligned} \tag{4.16}$$

where the filtered noise vector $\hat{\mathbf{n}}_m$ is

$$\hat{\mathbf{n}}_m = \mathbf{W}_K^H \mathcal{R}\left\{\mathbf{Q}_m \mathbf{n}\right\} \tag{4.17}$$

and

$$\mathbf{Q}_m = \mathbf{J}_m^H \mathbf{F}_K \mathbf{R}^\top \mathbf{G}_m \mathbf{H}^{-1}. \tag{4.18}$$

Since $\mathbf{n}$ is a circularly symmetric Gaussian random vector which with correlation matrix $N_0\mathbf{I}$, the correlation of $\hat{\mathbf{n}}_m$ is

$$\mathbf{E}\{\hat{\mathbf{n}}_m \hat{\mathbf{n}}_m^H\} = \frac{N_0}{2}\mathbf{W}_K^H \mathcal{R}\left\{\mathbf{Q}_m \mathbf{Q}_m^H\right\}\mathbf{W}_K. \tag{4.19}$$

The term $\mathcal{R}\left\{\mathbf{Q}_m \mathbf{Q}_m^H\right\}$ is a diagonal matrix whose diagonal elements are

$$\left[\mathcal{R}\left\{\mathbf{Q}_m \mathbf{Q}_m^H\right\}\right]_{k,k} = \frac{1}{KM}\sum_{n=0}^{KM-1} \frac{|\sum_{i=0}^{KM-1} g_{i,m} \mathrm{e}^{-j\phi_{i,n,k,m}}|^2}{|H_n|^2}, \tag{4.20}$$

where

$$\phi_{i,n,k,m} = \left[-\frac{\pi}{2}(k+m) - \frac{2\pi}{K}(i \mod K) + \frac{2\pi}{KM} ni \right], \tag{4.21}$$

and H_k is the kth component of the channel frequency response of $\mathbf{h}$, i.e.,

$$H_k = \sum_{n=0}^{KM-1} h_n \mathrm{e}^{-j2\pi kn/(KM-1)}. \tag{4.22}$$

The proof of (4.20) is provided in Appendix A. It then follows that the diagonal elements of the correlation matrix in (4.19) are

$$\left[\mathbf{E}\{\hat{\mathbf{n}}_m \hat{\mathbf{n}}_m^H\}\right]_{k,k} = \frac{N_0}{2} \sum_{l=0}^{K-1} |w_{k,l}|^2 \left[\mathcal{R}\left\{\mathbf{Q}_m \mathbf{Q}_m^H\right\}\right]_{l,l}. \tag{4.23}$$

The Walsh-Hadamard matrix has the property that $|w_{k,l}| = \frac{1}{\sqrt{K}}$ for all k, l. Therefore, the noise correlation matrix has identical diagonal elements, which are

$$\left[\mathbf{E}\{\hat{\mathbf{n}}_m \hat{\mathbf{n}}_m^H\}\right]_{k,k} = \frac{N_0}{2K^2M} \sum_{l=0}^{K-1} \sum_{n=0}^{KM-1} \frac{|\sum_{i=0}^{KM-1} g_{i,m} \mathrm{e}^{-j\phi_{i,n,l,m}}|^2}{|H_n|^2}. \tag{4.24}$$

The BER of a WH-CFBMC-OQAM system can be obtained based on the signal-to-noise ratio (SNR) associated with the equivalent input/output expression in (4.16). Let $E_s = \mathbf{E}\{|s_{k,m}|^2\}$ be the average transmitted energy of the QAM symbols. Furthermore, assume that the real and imaginary components of the QAM signal have equal energy, i.e., $\mathbf{E}\{|a_{k,m}|^2\} = E_s/2$. Then the SNR corresponding to the detection of $a_{k,m}$ is

$$\beta_{k,m} = \frac{E_s/2}{[\mathbf{E}\{\hat{\mathbf{n}}_m \hat{\mathbf{n}}_m^H\}]_{k,k}} = \frac{\gamma_s K^2 M}{\sum_{l=0}^{K-1} \sum_{n=0}^{KM-1} \frac{|\sum_{i=0}^{KM-1} g_{i,m} \mathrm{e}^{-j\phi_{i,n,l,m}}|^2}{|H_n|^2}}, \tag{4.25}$$

where $\gamma_s = E_s/N_0$. Equation (4.25) implies that $\beta_{k,m}$ does not depend on k since the operation of Wash-Hadamard matrix averages the SNR over all subcarriers. Then, one can write

$$\beta_{k,m} = \beta_m = \frac{\gamma_s}{\alpha_m} \quad \text{for all } k, \tag{4.26}$$

where

$$\alpha_m = \frac{1}{K^2M} \sum_{l=0}^{K-1} \sum_{n=0}^{KM-1} \frac{|\sum_{i=0}^{KM-1} g_i \mathrm{e}^{-j\phi_{i,n,l,m}}|^2}{|H_n|^2}. \tag{4.27}$$

The BER with 2^{μ}-QAM constellation with Gray coding of WH-CFBMC-OQAM is well approximated as

$$P_{\text{WH-CFBMC-OQAM}} = \frac{4}{\mu M}\left(1 - \frac{1}{2^{\mu/2}}\right)\sum_{m=0}^{M-1} Q\left(\sqrt{\frac{3\mu\gamma_b}{\alpha_m(2^{\mu}-1)}}\right), \tag{4.28}$$

where $\gamma_b = \frac{E_b}{N_0}$ and $E_b = E_s/\mu$ is the energy per bit. It is pointed out that α solely depends on the coefficients of the prototype filter, and the channel coefficients.

4.3 Simulation Result

This section present simulation results of WH-CFBMC-OQAM. First, its BER performance over FSCs is discussed. BER performance of four other systems is also included for comparison. Those systems are OFDM, CFBMC-OQAM, GFDM, and WH-GFDM. The first three systems are non-precoding systems presented in previous sections. The last one is a precoded GFDM system based on WH, presented in [21]. Second, the theoretical approximation for the BER performance of WH-CFBMC-OQAM are illustrated and compared with the simulation results.

Fig. 4.4 and Fig. 4.5 present the BER performance of OFDM, GFDM, WH-GFDM, CFBMC-OQAM, and WH-CFBMC-OQAM under two different FSCs, each for two constellations of 4-QAM and 64-QAM. The delay profiles of the two channels are provided in Table 4.3. GFDM and CFBMC-OQAM signals are transmitted block by block, where one block has KM symbols. In the simulation, the duration of a time slot (subsymbol) is $T = 256\ \mu s$. A block of KM symbols is transmitted over the duration of MT seconds, leading to the sampling period (duration of one symbol) of $T_s = MT/KM = T/K = 4\ \mu s$. An L-paths channel can be modelled by a V-tap discrete filter as [7]

$$h[v] = \sum_{l=0}^{L-1} |q_l| \mathrm{e}^{j\phi_l}\ \mathrm{sinc}\left[v - \frac{\tau_l}{T_s}\right] \quad v = 0, 1, \ldots, V-1, \tag{4.29}$$

where τ_l, and $|q_l|\mathrm{e}^{j\phi_l}$ is the delay, and complex gain of the lth path, respectively. In the simulation, $|q_l|$ is computed based on the specified dB gain of each path, and ϕ_l is generated randomly in the range $[0, 2\pi]$. The value of V is chosen such that $|h[v]|$ is small when v is greater than V.

Table 4.2: Simulation parameters.

Parameters	Value
Number of subcarriers (K)	64
Number of subsymbols (M)	31
Prototype filter	SRRC
Roll-off	0.9
Modulation	4-QAM, 64-QAM

Table 4.3: Delay profile used in simulation.

Channel A	Gain (dB)	0	-8	-14	-	-	-	-
	Delay (μs)	0	4.57	9.14	-	-	-	-
Channel B	Gain (dB)	0	-10	-12	-13	-16	-20	-22
	Delay (μs)	0	2.85	4.57	6.28	9.71	15.43	20

Fig. 4.4 shows that WH-CFBMC-OQAM performs 2.5 dB better than WH-GFDM at the BER level of 10^{-4} even with a large constellation such as 64-QAM. Since WH-GFDM is based on GFDM, which is a non-orthogonal system, the interference between subsymbols and subcarriers is intensified in a FSC. That makes the BER performances of WH-GFDM worse than that of WH-CFBMC-OQAM. WH-GFDM and WHT-CFBMC-OQAM offer even a larger performance gain under Channel B. Specifically, WH-GFDM is 5 dB better than the non-precoding scheme, while WH-CFBMC-OQAM achieves 7.5 dB SNR gain at BER $= 10^{-4}$.

Fig. 4.6 shows that (4.28) can be used to accurately estimate the BER of WHT-C-FBMC over a FSC. In both channels, with 4-QAM modulation, the theoretical result matches perfectly with that of the simulation result for any SNR value. With 64-QAM modulation, the theoretical approximation is very accurate at SNR larger than 7.5 dB.

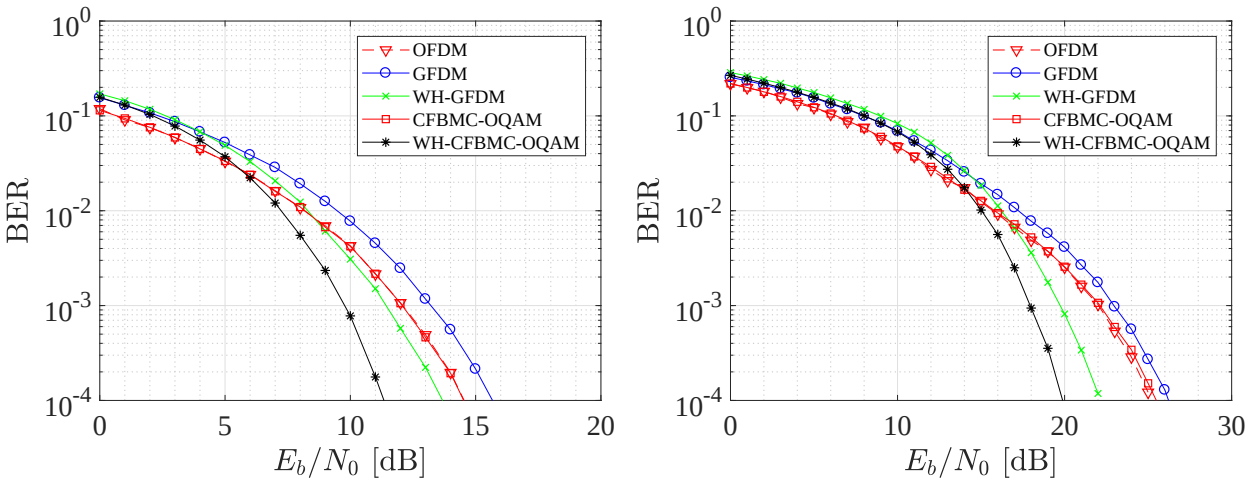

(a) 4-QAM (b) 64-QAM

Figure 4.4: WH-CFBMC-OQAM and WH-GFDM BER performance over Channel A.

4.4 Summay

To enhance the BER performance of CFBMC-OQAM in a FSC, this chapter studies a precoded version of CFBMC-OQAM, called WH-CFBMC-OQAM, which uses the unitary Walsh-Hadamard precoding matrix. WH-CFBMC-OQAM exploits the frequency diversity by averaging the SNR output over all subcarriers. A theoretical approximation for the BER of WH-CFBMC-OQAM has also been provided, which depends on the filter coefficients and channel gains. Results show that WH-CFBMC-OQAM not only performs significantly better than the conventional CFBMC-OQAM but also better than WH-GFDM.

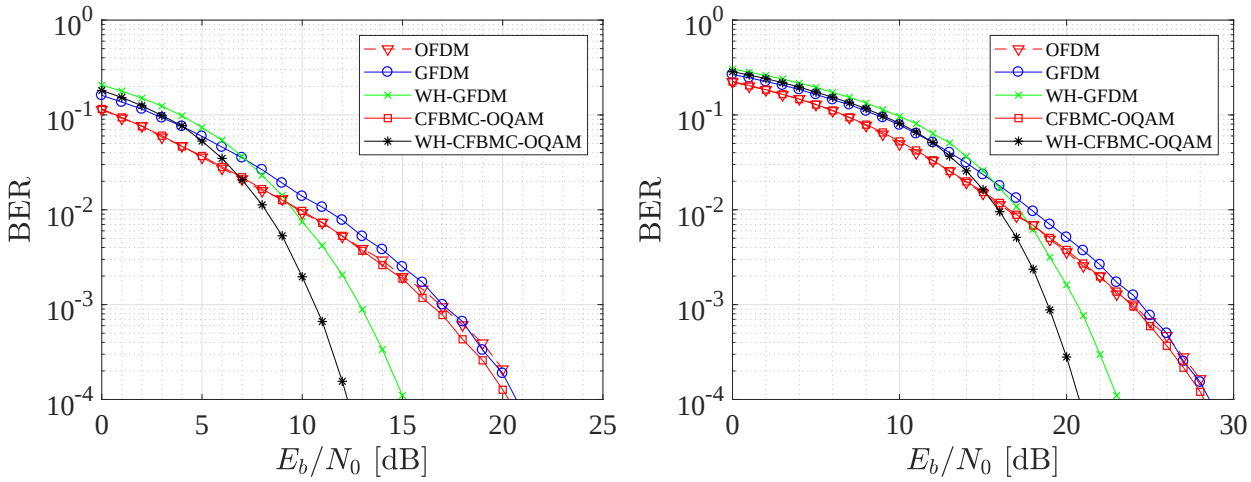

(a) 4-QAM (b) 64-QAM

Figure 4.5: WH-CFBMC-OQAM and WH-GFDM BER performance over Channel B.

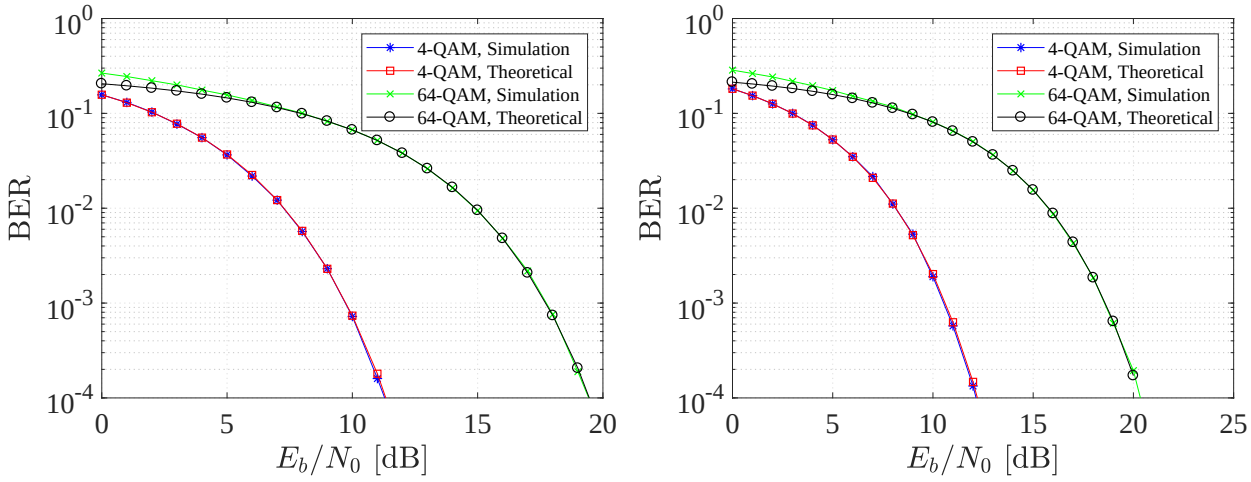

(a) Channel A (b) Channel B

Figure 4.6: Simulation versus theoretical results of WH-CFBMC-OQAM system.

5. Conclusion and Suggestion for Further Research

5.1 Conclusion

This thesis studies candidate multicarrier transmission techniques for 5G systems. First, a classic cyclic prefix OFDM system is presented. Due to its efficient implementation via FFT/IFFT blocks and simple frequency domain equalizer, OFDM is still a candidate for 5G. However, its main weaknesses, high side lobes and low spectral efficiency, motivate researchers to find potential alternatives.

Filter bank multicarrier offset QAM (FBMC-OQAM) and generalized frequency division multiplexing (GFDM) are two multicarrier techniques which are actively investigated. FBMC-OQAM addresses the drawback of rectangular time windowing in OFDM by using a prototype filter that satisfies the Nyquist condition. The orthogonality between subcarriers in FBMC-OQAM is achieved by using offset QAM. However, unlike OFDM, FBMC-OQAM does not have a block-based structure to facilitate an efficient implementation as well as a simple equalization. In constrast, GFDM has a block-based structure. It exploits that structure to replace the linear convolution in filtering with circular convolution. By doing so, the length of the cyclic prefix (CP) does not need to take into account the length of the filter and thus the overhead due to the use of the CP can be reduced. Unfortunately, GFDM is not an orthogonal system. The non-orthogonality between subcarriers requires a complex receiver to cancel intercarrier interference.

Recently, circular filter bank multicarrier offset QAM (CFBMC-OQAM) is proposed, which combines two key features, the offset QAM of the conventional FBMC-OQAM and the

block-based structure and circular convolution of GFDM in one system. The combination makes CFBMC-OQAM not only being an orthogonal system as FBMC-OQAM but also having an efficient implementation structure and simple equalization as GFDM.

The main contribution of this thesis is developing and analyzing a precoded scheme for CFBMC-OQAM is studied. In particular, WH-CFBMC-OQAM, which applies the Walsh-Hadamard transform to the CFBMC-OQAM system, has been developed. The objective of the precoded scheme is to make WH-CFBMC-OQAM more robust in frequency selective channels than FBMC-OQAM, GFDM, and CFBMC-OQAM. To estimate the BER performance of WH-CFBMC-OQAM over FSCs a theoretical approximation is derived. Under FSCs, simulation results show a significant performance improvement of WH-CFBMC-OQAM. Under the same system parameters setup, WH-CFBMC-OQAM is shown to outperform the non-precoded system, OFDM, FBMC-OQAM, CFBMC-OQAM, GFDM, and also the precoded system, WH-GFDM.

While the Walsh-Hadamard (WH) transform is proposed for precoding in this thesis, the framework and the performance analysis can be carried out for other unitary matrix transforms. For a simple implementation, WH is chosen since its entries are just real numbers. One may use other transforms to meet different objectives. For example, a CAZAC unitary transform [35] can be considered for further reducing the peak-to-average power ratio (PAPR) as suggested in [36].

The theoretical approximation of the BER performance of WH-CFBMC-OQAM under FSCs derived in this thesis could potentially be helpful in the designing of a prototype filter for an WH-CFBMC-OQAM system. Specifically, since the theoretical approximation depends on the coefficients of the prototype filter, one can use it to design an optimal filter for WH-CFBMC-OQAM that minimizes the BER.

5.2 Suggestion for Further Research

To meet the challenging objectives of 5G networks, researchers have studied new and more effective PHY techniques. There has been a growing interest on index modulation

(IM) over the past few years. IM is a new digital modulation scheme with high spectral and energy efficiency, in which the indices of the building blocks of the considered communications system are utilized to transmit additional information bits [37]. Reference [38] perhaps is the first to propose a technique called spatial modulation (SM), which is IM in the spatial domain. In this technique the indices of antennas are utilized to convey additional information bits. This technique has an advantage that only one antenna at the transmitter is active. The receiver's complexity of SM is reduced significantly compared to its competitors such as vertical Bell Labs layered space-time (V-BLAST) and space-time coding (STC) systems. Inspired by index modulation in the spatial domain, researchers have explored index modulation in the frequency domain as well. In particular, reference [39] proposed OFDM-IM where an incoming bit stream is split into index selection bits and M-ary constellation bits. The index selection bits determine a subset of subcarriers and those subcarriers are set to active while other subcarriers are off. CFBMC-OQAM and WH-CFBMC-OQAM have a block based structure like OFDM and thus the IM concept can be applied to these two schemes. In addition, the separation between real and imaginary parts of complex symbols in CFBMC-OQAM might result in a different way to manipulate indicies of subcarriers. Applying IM in CFBMC-OQAM systems is a promising research topic.

Appendix

From (4.18), $\mathcal{R}\left\{\mathbf{Q}_m\mathbf{Q}_m^H\right\}$ is given as

$$\mathcal{R}\left\{\mathbf{Q}_m\mathbf{Q}_m^H\right\} = \mathcal{R}\left\{\mathbf{J}_m^H\mathbf{F}_K\mathbf{R}^\top\mathbf{G}_m\mathbf{H}^{-1}(\mathbf{H}^{-1})^H\mathbf{G}_m\mathbf{R}\mathbf{F}_K^H\mathbf{J}_m\right\} \tag{A.1}$$

Recall that $\mathbf{H}$ is a $KM\times KM$ circulant matrix. Thus, one has $\mathbf{H}^{-1}(\mathbf{H}^{-1})^H = \frac{1}{KM}\mathbf{F}_{KM}^H\mathbf{\Lambda}\mathbf{F}_{KM}$, where $\mathbf{\Lambda} = \mathrm{diag}(|H_0|^{-2}, |H_1|^{-2}, \ldots, |H_{KM-1}|^{-2})$. Rewrite (A.1) as

$$\mathcal{R}\left\{\mathbf{Q}_m\mathbf{Q}_m^H\right\} = \frac{1}{KM}\mathcal{R}\left\{\mathbf{T}_m\mathbf{\Lambda}\mathbf{T}_m^H\right\} \tag{A.2}$$

where

$$\mathbf{T}_m = \mathbf{Y}_m\mathbf{F}_{KM}^H, \quad \mathbf{Y}_m = \mathbf{J}_m^H\mathbf{F}_K\mathbf{R}^\top\mathbf{G}_m. \tag{A.3}$$

The (k,n) elements of $\mathbf{T}_m$ are

$$t_{k,n} = \sum_{i=0}^{KM-1} y_{k,i}\mathrm{e}^{j\frac{2\pi}{KM}ni}, \tag{A.4}$$

where

$$y_{k,i} = (-j)^{k+m}g_{i,m}\mathrm{e}^{-j\frac{2\pi}{K}k(i \mod K)}. \tag{A.5}$$

Thus, the elements of $\mathcal{R}\left\{\mathbf{Q}_m\mathbf{Q}_m^H\right\}$ are

$$[\mathcal{R}\left\{\mathbf{Q}_m\mathbf{Q}_m^H\right\}]_{k,k'} = \frac{1}{KM}\frac{\sum_{n=0}^{KM-1}\mathcal{R}\left\{t_{k,n}(t_{k',n})^*\right\}}{|H_n|^2} \tag{A.6}$$

For $k = k'$, it is easy to see that using (A.4) and (A.5) leads to the expression of $\left[\mathcal{R}\left\{\mathbf{Q}_m\mathbf{Q}_m^H\right\}\right]_{k,k}$ in (4.20).

For $k \neq k'$, one has

$$\begin{aligned}\mathcal{R}\left\{t_{k,n}(t_{k',n})^*\right\} &= \mathcal{R}\left\{\sum_{i=0}^{KM-1} y_{k,i}\mathrm{e}^{j\frac{2\pi}{KM}ni}\sum_{i'=0}^{KM-1}(y_{k',i'})^*\mathrm{e}^{-j\frac{2\pi}{KM}ni'}\right\} \\ &= \mathcal{R}\left\{\sum_{i=0}^{KM-1} y_{k,i}(y_{k',i})^*\right\} + \mathcal{R}\left\{\sum_{i=0}^{KM-1} y_{k,i}\mathrm{e}^{j\frac{2\pi}{KM}ni}\sum_{\substack{i'=0\\ i'\neq i}}^{KM-1} y_{k',i'}\mathrm{e}^{-j\frac{2\pi}{KM}ni'}\right\}\end{aligned} \tag{A.7}$$

From (4.13), and (A.5) it can be verified that $\mathcal{R}\left\{\sum_{i=0}^{KM-1} y_{k,i}(y_{k',i})^*\right\} = 0$. In addition, from (A.5) and the fact that $g_{KM-i,m} = g_{i,m}$ for $i < \frac{KM}{2}$, one has

$$\begin{aligned}y_{k,KM-i} &= (-j)^{k+m}g_{KM-i,m}\mathrm{e}^{-j\frac{2\pi}{K}k(KM-i \mod K)} \\ &= (-j)^{k+m}g_{i,m}\mathrm{e}^{j\frac{2\pi}{K}k(i \mod K)}.\end{aligned} \tag{A.8}$$

Using (A.5), and (A.8), one can verify that

$$\begin{aligned}\mathcal{R}\left\{y_{k,i}(y_{k',i'})^*\right\} &= -\mathcal{R}\left\{y_{k,KM-i}(y^m_{k',KM-i'})^*\right\} \\ \mathcal{I}\left\{y_{k,i}(y_{k',i'})^*\right\} &= \mathcal{I}\left\{y_{k,KM-i}(y^m_{k',KM-i'})^*\right\}.\end{aligned} \tag{A.9}$$

Thus, (A.7) can be rewritten as

$$\begin{aligned}&\mathcal{R}\left\{t_{k,n}(t_{k',n})^*\right\} \\ &= \sum_{i=0}^{KM/2-1}\mathcal{R}\left\{\left[y_{k,i}(y_{k',i'})^*\mathrm{e}^{j\frac{2\pi}{KM}n(i-i')} + y_{k,KM-i}(y^m_{k',KM-i'})^*\mathrm{e}^{-j\frac{2\pi}{KM}n(i-i')}\right]\right\} \\ &= \sum_{i=0}^{KM/2-1}\Bigg[\mathcal{R}\left\{y_{k,i}(y_{k',i'})^*\right\}\cos\frac{2\pi}{KM}n(i-i') - \mathcal{I}\left\{y_{k,i}(y_{k',i'})^*\right\}\sin\frac{2\pi}{KM}n(i-i') \\ &+\mathcal{R}\left\{y_{k,KM-i}(y_{k',KM-i'})^*\right\}\cos\frac{2\pi}{KM}n(i-i') + \mathcal{I}\left\{y_{k,KM-i}(y_{k',KM-i'})^*\right\}\sin\frac{2\pi}{KM}n(i-i')\Bigg] \\ &= 0.\end{aligned} \tag{A.10}$$

References

[1] F. Boccardi, R. W. Heath, A. Lozano, T. L. Marzetta, and P. Popovski, "Five disruptive technology directions for 5G," *IEEE Communications Magazine*, vol. 52, pp. 74–80, February 2014.

[2] J. G. Andrews, S. Buzzi, W. Choi, S. V. Hanly, A. Lozano, A. C. K. Soong, and J. C. Zhang, "What will 5G be?," *IEEE Journal on Selected Areas in Communications*, vol. 32, pp. 1065–1082, June 2014.

[3] C. X. Wang, F. Haider, X. Gao, X. H. You, Y. Yang, D. Yuan, H. M. Aggoune, H. Haas, S. Fletcher, and E. Hepsaydir, "Cellular architecture and key technologies for 5G wireless communication networks," *IEEE Communications Magazine*, vol. 52, pp. 122–130, February 2014.

[4] T. S. Rappaport, S. Sun, R. Mayzus, H. Zhao, Y. Azar, K. Wang, G. N. Wong, J. K. Schulz, M. Samimi, and F. Gutierrez, "Millimeter wave mobile communications for 5G cellular: It will work!," *IEEE Access*, vol. 1, pp. 335–349, 2013.

[5] C. Han, T. Harrold, S. Armour, I. Krikidis, S. Videv, P. M. Grant, H. Haas, J. S. Thompson, I. Ku, C. X. Wang, T. A. Le, M. R. Nakhai, J. Zhang, and L. Hanzo, "Green radio: radio techniques to enable energy-efficient wireless networks," *IEEE Communications Magazine*, vol. 49, pp. 46–54, June 2011.

[6] A. Osseiran, F. Boccardi, V. Braun, K. Kusume, P. Marsch, M. Maternia, O. Queseth, M. Schellmann, H. Schotten, H. Taoka, H. Tullberg, M. A. Uusitalo, B. Timus, and M. Fallgren, "Scenarios for 5G mobile and wireless communications: the vision of the METIS project," *IEEE Communications Magazine*, vol. 52, pp. 26–35, May 2014.

[7] D. Tse and P. Viswanath, *Fundamentals of wireless communication*. New York, NY, USA: Cambridge University Press, 2005.

[8] A. Goldsmith, *Wireless communications*. New York, NY, USA: Cambridge University Press, 2005.

[9] Proakis, *Digital communications 5th edition*. McGraw Hill, 2007.

[10] A. Sahin, I. Guvenc, and H. Arslan, "A survey on multicarrier communications: Prototype filters, lattice structures, and implementation aspects," *IEEE Communications Surveys Tutorials*, vol. 16, pp. 1312–1338, Third Quarter 2014.

[11] T. Hwang, C. Yang, G. Wu, S. Li, and G. Y. Li, "OFDM and its wireless applications: A survey," *IEEE Transactions on Vehicular Technology*, vol. 58, pp. 1673–1694, May 2009.

[12] B. Farhang-Boroujeny, "OFDM versus filter bank multicarrier," *IEEE Signal Processing Magazine*, vol. 28, pp. 92–112, May 2011.

[13] G. Fettweis, M. Krondorf, and S. Bittner, "GFDM-generalized frequency division multiplexing," in *Proceedings IEEE Vehicular Technology Conference*, pp. 1–4, April 2009.

[14] R. Datta, N. Michailow, M. Lentmaier, and G. Fettweis, "GFDM interference cancellation for flexible cognitive radio PHY design," in *Proceedings IEEE Vehicular Technology Conference*, September 2012.

[15] H. Lin and P. Siohan, "Multi-carrier modulation analysis and WCP-COQAM proposal," *EURASIP Journal on Advances in Signal Processing*, vol. 2014, pp. 79–98, May 2014.

[16] X.-G. Xia, "Precoded and vector OFDM robust to channel spectral nulls and with reduced cyclic prefix length in single transmit antenna systems," *IEEE Transactions on Communications*, vol. 49, pp. 1363–1374, August 2001.

[17] Z. Liu, Y. Xin, and G. B. Giannakis, "Linear constellation precoding for OFDM with maximum multipath diversity and coding gains," *IEEE Transactions on Communications*, vol. 51, pp. 416–427, March 2003.

[18] Y.-P. Lin and S.-M. Phoong, "BER minimized OFDM systems with channel independent precoders," *IEEE Transactions on Signal Processing*, vol. 51, pp. 2369–2380, September 2003.

[19] B. S. Chang, C. D. Rocha, D. L. Ruyet, and D. Roviras, "On the Use of Precoding in FBMC/OQAM Systems," in *ITS 2010*, (Manaus, Brazil), September 2010.

[20] B. S. Chang, C. A. F. da Rocha, D. L. Ruyet, and D. Roviras, "On the effect of ISI in the error performance of precoded FBMC/OQAM systems," in *Asia-Pacific Conference on Communications (APCC)*, pp. 987–991, October 2012.

[21] N. Michailow, L. Mendes, M. Matthé, I. Gaspar, A. Festag, and G. Fettweis, "Robust WHT-GFDM for the next generation of wireless networks," *IEEE Communication Letter*, vol. 19, pp. 106–109, January 2015.

[22] H. Nguyen and E. Shwedyk, *A First course in digital communications*. New York, NY, USA: Cambridge University Press, 2009.

[23] B. Muquet, Z. Wang, G. B. Giannakis, M. de Courville, and P. Duhamel, "Cyclic prefixing or zero padding for wireless multicarrier transmissions?," *IEEE Transactions on Communications*, vol. 50, pp. 2136–2148, December 2002.

[24] Y.-P. Lin, S.-M. Phong, and P. P. Vaidyanathan, *Filter bank transceivers for OFDM and DMT Systems*. New York, NY, USA: Cambridge University Press, 2010.

[25] A. V. Oppenheim, R. W. Schafer, and J. R. Buck, *Discrete-time signal processing*. Upper Saddle River, NJ, USA: Prentice-Hall, Inc., 2009.

[26] P. P. Vaidyanathan, *Multirate systems and filter banks*. Prentice-Hall signal processing series, Englewood Cliffs, N.J. Prentice Hall, 1993.

[27] B. Farhang-Boroujeny and C. H. (George) Yuen, "Cosine modulated and offset QAM filter bank multicarrier techniques: A continuous-time prospect," *EURASIP Journal on Advances in Signal Processing*, vol. 2010, pp. 1–17, 2010.

[28] R. W. Chang, "Synthesis of band-limited orthogonal signals for multichannel data transmission," *The Bell System Technical Journal*, vol. 45, pp. 1775–1796, December 1966.

[29] N. Michailow, I. Gaspar, S. Krone, M. Lentmaier, and G. Fettweis, "Generalized frequency division multiplexing: Analysis of an alternative multi-carrier technique for next generation cellular systems," in *Proceedings IEEE International Symposium Wireless Communication Systems*, pp. 171–175, August 2012.

[30] N. Michailow, M. Lentmaier, P. Rost, and G. Fettweis, "Integration of a GFDM secondary system in an OFDM primary system," in *2011 Future Network & Mobile Summit*, pp. 1–8, June 2011.

[31] B. Alves, L. Mendes, D. Guimaraes, and I. Gaspar, "Performance of GFDM over frequency-selective channels," in *International Workshop on Telecommunications*, vol. 15, May 2013.

[32] A. RezazadehReyhani, A. Farhang, and B. Farhang-Boroujeny, "Circularly pulse-shaped waveforms for 5G: Options and comparisons," in *2015 IEEE Global Communications Conference (GLOBECOM)*, pp. 1–7, December 2015.

[33] P. Vaidyanathan, "Filter banks in digital communications," *IEEE Circuits and Systems Magazine*, vol. 1, February 2001.

[34] X. Gao, W. Wang, X. G. Xia, E. K. S. Au, and X. You, "Cyclic prefixed OQAM-OFDM and its application to single-carrier FDMA," *IEEE Transactions on Communications*, vol. 59, pp. 1467–1480, May 2011.

[35] Y. Fang, Z. Zhang, and G. Liu, "A novel synchronization algorithm based on cazac sequence for ofdm systems," in *2012 8th International Conference on Wireless Communications, Networking and Mobile Computing*, pp. 1–4, September 2012.

[36] M. Matthe, L. Mendes, I. Gaspar, N. Michailow, D. Zhang, and G. Fettweis, "Precoded GFDM transceiver with low complexity time domain processing," *EURASIP Journal on Wireless Communications and Networking*, vol. 2016, pp. 138–147, May 2016.

[37] E. Basar, "Index modulation techniques for 5g wireless networks," *IEEE Communications Magazine*, vol. 54, pp. 168–175, July 2016.

[38] R. Mesleh, H. Haas, C. W. Ahn, and S. Yun, "Spatial modulation - a new low complexity spectral efficiency enhancing technique," in *2006 First International Conference on Communications and Networking in China*, pp. 1–5, October 2006.

[39] E. Basar, U. Aygolu, E. Panayrc, and H. V. Poor, "Orthogonal frequency division multiplexing with index modulation," *IEEE Transactions on Signal Processing*, vol. 61, pp. 5536–5549, November 2013.